August 1986 UILU-ENG-86-2221 95?

COORDINATED SCIENCE LABORATORY
College of Engineering

THEORETICAL STUDY OF THE TRANSVERSE DIELECTRIC CONSTANT OF SUPERLATTICES AND THEIR ALLOYS

Keith Brian Kahen

UNIVERSITY OF ILLINOIS AT URBANA-CHAMPAIGN

REPORT DOCUMENTATION PAGE

a. REPORT SECURITY CLASSIFICATION UNCLASSIFIED	1b. RESTRICTIVE MARKINGS NONE
a. SECURITY CLASSIFICATION AUTHORITY N/A	3. DISTRIBUTION/AVAILABILITY OF REPORT Approved for public release, distribution unlimited.
b. DECLASSIFICATION/DOWNGRADING SCHEDULE N/A	
. PERFORMING ORGANIZATION REPORT NUMBER(S) UILU-ENG-86-2221	5. MONITORING ORGANIZATION REPORT NUMBER(S) N/A
a. NAME OF PERFORMING ORGANIZATION Coordinated Science Laboratory, Univ. of Illinois	6b. OFFICE SYMBOL (If applicable) N/A
c. ADDRESS (City, State and ZIP Code) 1101 W. Springfield Avenue Urbana, Illinois 61801	7a. NAME OF MONITORING ORGANIZATION NASA - Lewis Research Center National Aeronautics and Space Administrati 7b. ADDRESS (City, State and ZIP Code) 2100 Brookpark Road Cleveland, Ohio 44135
a. NAME OF FUNDING/SPONSORING ORGANIZATION NASA - Lewis Research Center	8b. OFFICE SYMBOL (If applicable) N/A 9. PROCUREMENT INSTRUMENT IDENTIFICATION NUMBER NASA NAG 3-507
c. ADDRESS (City, State and ZIP Code) 2100 Brookpark Road Cleveland, Ohio 44135	10. SOURCE OF FUNDING NOS.

PROGRAM ELEMENT NO.	PROJECT NO.	TASK NO.	WORK UNIT NO.
N/A	N/A	N/A	N/A

1. TITLE (Include Security Classification)
Theoretical Study of the Transverse Dielectric Constant of Superlattices and Their Alloys

2. PERSONAL AUTHOR(S)
Keith Brian Kahen

3a. TYPE OF REPORT	13b. TIME COVERED	14. DATE OF REPORT (Yr., Mo., Day)	15. PAGE COUNT
Technical	FROM _____ TO _____	July 1986	87

6. SUPPLEMENTARY NOTATION
N/A

7. COSATI CODES			18. SUBJECT TERMS (Continue on reverse if necessary and identify by block number)
FIELD	GROUP	SUB. GR.	superlattices, optical constants, alloys, dielectric constant, index of refraction, absorption coefficient

9. ABSTRACT (Continue on reverse if necessary and identify by block number)

In this thesis the optical properties of III-V binary and ternary compounds and GaAs-$Al_xGa_{1-x}As$ superlattices are determined by calculating the real and imaginary parts of the transverse dielectric constant, $\varepsilon(\omega)=\varepsilon_1(\omega) + i\varepsilon_2(\omega)$. Emphasis is given to determining the influence of different material and superlattice (layer thickness and Al composition) parameters on the values of the index of refraction, $\eta(\omega)$ and absorption coefficient, $\alpha(\omega)$.

In order to calculate the optical properties of a material, it is necessary to compute its electronic band structure. We accomplish this by introducing a partition band structure approach based on a combination of the $\vec{k}\cdot\vec{p}$ and nonlocal pseudopotential techniques. In this approach the bulk Brillouin zone is partitioned into the Γ, X, and L regions by performing $\vec{k}\cdot\vec{p}$ expansions about these symmetry points. The advantages of this approach are that it is accurate, computationally fast, analytical, and flexible. These last two properties enable us to incorporate easily into the model additional effects, such as disorder scattering, which occurs for alloy materials, and excitons. Furthermore, the model is easily extended to more
(Continued on the back side)

0. DISTRIBUTION/AVAILABILITY OF ABSTRACT	21. ABSTRACT SECURITY CLASSIFICATION
NCLASSIFIED/UNLIMITED ☒ SAME AS RPT. ☐ OTIC USERS ☐	UNCLASSIFIED
2a. NAME OF RESPONSIBLE INDIVIDUAL	22b. TELEPHONE NUMBER (Include Area Code) / 22c. OFFICE SYMBOL NONE

19. Abstract (continued)

complex structures, for example, multiple quantum wells and superlattices. The results for $n(\omega)$ and $\alpha(\omega)$ of bulk III-V compounds compare well with other one-electron band structure model and our calculations show that for small frequencies, the index of refraction is determined mai by the contributions of the outer regions of the Brillouin zone.

The effects of alloy scattering are incorporated into the model using a perturbative CPA approach which only includes the influence of compositional disorder. The results for the disc induced, Γ point, energy-gap bowings are shown to be nearly comparable to those calculated usin more sophisticated CPA approaches. Furthermore, the calculated absorption coefficient of $Al_xGa_{1-x}As$ is found to be in good agreement with the experimental data.

The model is extended to heterostructures by using the envelope-function approximation. Valence-band mixing and Γ-region exciton effects are also included in the model. Our results show that the anisotropy and structure dependence of the refractive index of superlattices resu mainly from the contribution of the Γ region, while the contributions of the outer regions of t zone are rather insensitive to the superlattice structure. The superlattice index of refractio values is determined to attain maxima at the various Γ-region, quantized, transition energies, where for certain structures the difference between the refractive indices of the superlattice and its corresponding $Al_xGa_{1-x}As$ alloy can be as large as 2%. Overall, the superlattice result are in good agreement with the available absorption and refractive index data.

THEORETICAL STUDY OF THE TRANSVERSE DIELECTRIC CONSTANT OF SUPERLATTICES AND THEIR ALLOYS

BY

KEITH BRIAN KAHEN

B.S., University of Illinois, 1981
M.S., University of Illinois, 1983

THESIS

Submitted in partial fulfillment of the requirements
for the degree of Doctor of Philosophy in Electrical Engineering
in the Graduate College of the
University of Illinois at Urbana-Champaign, 1986

Urbana, Illinois

THEORETICAL STUDY OF THE TRANSVERSE DIELECTRIC CONSTANT OF SUPERLATTICES AND THEIR ALLOYS

Keith Brian Kahen, Ph.D.
Department of Electrical and Computer Engineering
University of Illinois at Urbana-Champaign, 1986

In this thesis the optical properties of III-V binary and ternary compounds and GaAs-$Al_xGa_{1-x}As$ superlattices are determined by calculating the real and imaginary parts of the transverse dielectric constant, $\epsilon(\omega) = \epsilon_1(\omega) + i\epsilon_2(\omega)$. Emphasis is given to determining the influence of different material and superlattice (layer thickness and Al composition) parameters on the values of the index of refraction, $\eta(\omega)$ and absorption coefficient, $\alpha(\omega)$.

In order to calculate the optical properties of a material, it is necessary to compute its electronic band structure. We accomplish this by introducing a partition band structure approach based on a combination of the $\vec{k} \cdot \vec{p}$ and nonlocal pseudopotential techniques. In this approach the bulk Brillouin zone is partitioned into the Γ, X, and L regions by performing $\vec{k} \cdot \vec{p}$ expansions about these three symmetry points. The advantages of this approach are that it is accurate, computationally fast, analytical, and flexible. These last two properties enable us to incorporate easily into the model additional effects, such as disorder scattering, which occurs for alloy materials, and excitons. Furthermore, the model is easily extended to more complex structures, for example, multiple quantum wells and superlattices. The results for $\eta(\omega)$ and $\alpha(\omega)$ of bulk III-V compounds compare well with other one-electron band structure models, and our calculations show that for small frequencies, the index of refraction is determined mainly by the contributions of the outer regions of the Brillouin zone.

The effects of alloy scattering are incorporated into the model using a perturbative CPA approach which only includes the influence of compositional disorder. The results for the disorder-induced, Γ point, energy-gap bowings are shown to be nearly comparable to those calculated using more sophisticated CPA approaches. Furthermore, the calculated

absorption coefficient of $Al_xGa_{1-x}As$ is found to be in good agreement with the experimental data.

The model is extended to heterostructures by using the envelope-function approximation. Valence-band mixing and Γ-region exciton effects are also included in the model. Our results show that the anisotropy and structure dependence of the refractive index of superlattices result mainly from the contribution of the Γ region, while the contributions of the outer regions of the zone are rather insensitive to the superlattice structure. The superlattice index of refraction values is determined to attain maxima at the various Γ-region, quantized, transition energies, where for certain structures the difference between the refractive indices of the superlattice and its corresponding $Al_xGa_{1-x}As$ alloy can be as large as 2%. Overall, the superlattice results are in good agreement with the available absorption and refractive index data.

ACKNOWLEDGEMENTS

The author is deeply indebted to his advisor Professor Jean-Pierre Leburton for his constant guidance, support, and wisdom.

The author would like to thank especially Professor K. Hess for his interest and keen insights.

The author would like to thank also Professors N. Holonyak, Jr., B. Oakley, and B. Wheeler for their interest and helpfulness.

The support of the National Aeronautics and Space Administration is most appreciated.

For the assistance and friendship of Drs. K. Brennan, D. Widiger, T. Wang, and B. A. Mason, the author is most grateful.

The author is especially thankful for the friendship of R. Thorne, S. Manion, and D. Steiger.

Finally, an extra thanks goes to D. "Chet" Arnold for his humor, kindness, and friendship during the past years.

TABLE OF CONTENTS

1. INTRODUCTION

Sophisticated growth techniques, such as Molecular Beam Epitaxy (MBE)[1] and Metalorganic Chemical Vapor Deposition (MOCVD),[2] have made possible the advent of artificial semiconductor structures called superlattices or multiple quantum wells (MQWs). The structures consist of alternating layers of two lattice-matched solids. This layering adds a periodic potential along the growth axis to the existing periodic lattice potential. As the thicknesses of the layers decrease to values on the order of a few hundred Angstroms, quantum size effects, produced by the increasing confinement of the electrons and holes in the growth direction, become important and modify the properties of the structures from those of bulk, three-dimensional materials, to those of quasi-two-dimensional structures.[3] For instance, because of the enhancement of the exciton binding energy in quasi 2-D quantum wells,[4] exciton resonances are clearly visible at room temperature, while in bulk semiconductors, such as GaAs, the excitons are barely discernible at 300 K.[5] As a second example, at 300 K bulk GaAs lasers operate in the near infrared (~ 1.42 eV), while $Al_xGa_{1-x}As$-GaAs MQW lasers can be designed to operate in the visible red region (~ 1.83 eV), i.e., 400 meV higher than the bulk GaAs value, and have improved lasing characteristics.[6-7] In fact, by modifying the composition and thickness of the layers, the electronic and optical properties of superlattices can be modified over a considerable range.[8] For these reasons, MQWs and superlattices have become technologically important in both optoelectronics[7,9-11] and microelectronics.[12]

As a result of the many device applications of superlattices, their optical and electronic properties have been studied extensively both experimentally[1-7,9-16] and theoretically.[8,10,17-28] The major thrust of this research has focused on properties derived from electronic transitions originating around a region surrounding the Γ symmetry point. This has occurred for two reasons: devices frequently operate just above the Γ energy gap, and theoretical models of the Γ region usually are straightforward and analytically simple.

An example of the latter is exciton effects which can be described simply within the Effective-Mass Approximation (EMA) for Γ region transitions, while for Brillouin zone-edge transitions it becomes necessary to implement a many body approach.[29]

Recently, there has been suggested and demonstrated a number of optoelectronic devices based on the properties of the index of refraction of long period, i.e., > 100 Å, superlattices and multiple quantum wells.[9-10,30-34] A few examples of these devices are superlattice lasers which are monolithically integrated into higher-gap cavities via impurity diffusion.[9] electro-optic and optical-intensity controlled MQW switches.[32,33] and MQW phase modulators.[34] As a result, the index of refraction of superlattices and MQWs has become a technologically important parameter. However, unlike the absorption coefficient which only excites specific regions of the Brillouin zone, the index of refraction depends on transitions originating from all points of the Brillouin zone. Although most band structure models can describe the Γ region properly, they cannot calculate the index of refraction because of either analytical[18-19,25] or computational[17,20,27] difficulties. More specifically, the tight binding method[18-19,25] is valid for long-period superlattices, but has difficulty describing the structure at the edges of the Brillouin zone,[35-36] making questionable optical models in these regions. On the other hand, the pseudopotential technique[17,20,27] is excellent for short period, i.e., a few layers, superlattices, but has severe computational problems for long-period superlattices on account of the inversion of very large matrices. Furthermore, because of the complexity of the pseudopotential technique, many electron effects, such as alloy scattering, exciton effects and band tailing, are very difficult to incorporate into these models.

Consequently, a superlattice band structure model[28] based on a partition approach[37] was developed for calculating the optical properties of long-period heterostructure materials. More specifically, the model calculates the real and imaginary parts of the transverse dielectric constant, $\epsilon(\omega) = \epsilon_1(\omega) + i\epsilon_2(\omega)$, from which all of the optical properties of materials can be easily determined. Hence, the index of refraction, in

addition to the absorption coefficient, can be computed using this model. Unlike previous techniques for long-period superlattices, the computed band structures are accurate at the zone edges, and the calculations require a comparatively small amount of computation time.[28] Furthermore, the effects of alloy scattering and excitons are easily incorporated into the model.

In this thesis the superlattice band structure model based on the partition method is presented in detail. The following is a summary of the model. In the partition method the $\vec{k}\cdot\vec{p}$[38-39] and nonlocal pseudopotential[40] techniques are used to partition the Brillouin zones of the constituent superlattice materials into the Γ, X, and L regions, and to determine the bulk energy band and matrix element dispersion relations. Superstructure effects are incorporated into the model within the envelope-function approximation.[21] Band-mixing effects are neglected at first, as are superstructure effects for wavevectors parallel to the superlattice layers.[24] The quantized transition levels are determined from the solution of the periodic square well potential problem which incorporates energy-dependent masses[41] and assumes a 65:35, Γ-point, band-discontinuity ratio.[42] Exciton effects are included in the model only for the Γ region using the EMA.[29,43] For the alloy layers, the effects of alloy scattering are incorporated within the Coherent Phase Approximation (CPA)[44] via a perturbation theory calculation.[45-46]

In Chapter 2 the partition method is presented and applied to bulk III-V compounds. Included is the general $\vec{k}\cdot\vec{p}$ formalism and the derivations of the $\vec{k}\cdot\vec{p}$ energy dispersion relations for the Γ, X, and L symmetry points. We also present a table of the valence and conduction band effective masses at the Γ, X, and L points for each of five III-V compounds, GaP, GaAs, InP, InAs, and AlAs. In the next section of Chapter 2, general considerations on the complex dielectric constant and related optical parameters, namely, the absorption coefficient and the index of refraction, are presented. A description is also given of the partition method used to perform the calculations of the transverse dielectric constant. We conclude this chapter by discussing our results for the complex dielectric

constant of the five III-V compounds. The effects of alloy scattering are incorporated into the model in Chapter 3, with results given for the frequency-dependent absorption coefficient of $Al_xGa_{1-x}As$ alloys. In Chapter 4, we present our electronic band structure model for GaAs-$Al_xGa_{1-x}As$ superlattices. Band mixing is neglected and superstructure effects are assumed to influence the particles for all energies. Included is a derivation of our interface connection rules used to account for the discontinuities of the electronic properties of the component superlattice materials. Results are given for the frequency and structure-dependent index of refraction of GaAs-AlAs superlattices. In Chapter 5 the superlattice model is modified by incorporating band mixing and considering superstructure effects important only for energies below the superlattice potential barriers. Furthermore, the model is extended to incorporate the influence of the Γ region excitons. A description of our exciton binding energy model is also included. Results are given for the frequency-dependent absorption coefficient and index of refraction of GaAs-$Al_xGa_{1-x}As$ superlattices. A discussion is also included on the effect of the above modifications on the model presented in Chapter 4. Finally, the models and findings presented in the previous chapters are summed up in Chapter 6.

2. TRANSVERSE DIELECTRIC CONSTANT OF III-V COMPOUNDS

2.1 Introduction

As discussed previously, the evaluation of the complex transverse dielectric constant $\epsilon(\omega)$ requires a knowledge of the entire band structure of a material. Hence, it is necessary to determine the wave functions and energy bands throughout the irreducible region of the first Brillouin zone. A number of band structure techniques, for example, orthogonal plane wave[47,48] (OPW), augmented plane wave[49] (APW), pseudopotential,[40] and linear combination of Gaussian orbitals[50] (LCGO), have been implemented to calculate, with varying success, the dielectric constant of bulk semiconductors. However, these different theoretical approaches employ sophisticated computational methods which require extended running times. Hence, with most of these models it is difficult to assess the relative importance of band structure parameters, such as effective masses and optical matrix elements, in determining the value of the real part of the dielectric constant. Furthermore, because of the complexity of these techniques, it becomes difficult to incorporate into these models many body effects, such as band tailing and excitons, and compositional disorder, i.e., alloy compounds, and also to extend these models to heterostructures (superlattices). Consequently, previous bulk band structure techniques cannot be adapted beyond bulk structures without requiring prohibitive computer usage and losing their simplicity.

This prompted us to formulate a bulk band structure technique based on the $\vec{k} \cdot \vec{p}$ method.[38] In this technique the band structure is generated by expanding about one or several symmetry points. Since one of our goals is to be able to understand the optical properties of III-V compounds in general and to extend our method to more complex structures, it is desirable to have simple, analytical expressions for the energy bands and matrix elements. Consequently, we partition the zone into three regions by expanding about the three highest symmetry points, Γ, X, and L. For each point we use a small

number of bands in each of our $\vec{k} \cdot \vec{p}$ basis sets, therefore limiting the accuracy of the energy band expressions to regions surrounding the expansion points. Because of the size of the X and L regions, it is necessary to supplement the X and L point expansions by ones about the K and W symmetry points, also. However, because of the low symmetry characterizing these points, it is difficult to obtain the $\vec{k} \cdot \vec{p}$ energy dispersion relations and optical matrix elements in the volumes surrounding these two points. Therefore, for both the K and W points, analytical expressions for the energies and matrix elements are obtained directly from the results of nonlocal pseudopotential calculations which include the spin orbit interaction. The nonlocal pseudopotential results are also used to fit empirically the $\vec{k} \cdot \vec{p}$ band parameters when experimental energy gaps and masses are not available. In this way our approach appears as a hybrid model by combining the simplicity and flexibility of the $\vec{k} \cdot \vec{p}$ method with the accuracy and generality of the nonlocal pseudopotential technique.

Because we have partitioned the Brillouin zone into three regions, Γ, X, and L, the dielectric constant is then calculated as the sum of the contributions of these three Brillouin zone regions. By considering each region separately, our approach engenders a physical understanding of the parameters which influence the dielectric constant. Moreover, because it is based on the $\vec{k} \cdot \vec{p}$ method, it is sufficiently flexible to include secondary effects and complex structures, and it is computationally fast.

The precursor of our band structure model is an analytical partition method approach proposed by Cardona.[39] He calculated $\epsilon_2(\omega)$ for bulk semiconductor compounds by decomposing $\epsilon_2(\omega)$ into the contributions of a three-dimensional, critical point labeled E_0, a two-dimensional, critical point labeled E_1, and a one-dimensional, critical point labeled E_2 (see discussion in Sec. 2.4). The E_0 point accounts for the absorption edge of $\epsilon_2(\omega)$, while the E_1 and E_2 points produce the E_1 and E_2 peak structures in $\epsilon_2(\omega)$, respectively. He proposed that the E_0 absorption edge is due to band-edge transitions at Γ, the E_1 peak arises from transitions along the eight equivalent <111> directions, and the E_2 peak originates

from transitions which include or are close in energy to those at the X point. Next, for each critical point he constructed energy dispersion relations having the dimensionality of the points. More specifically, the 3-D E_0 point was modeled by parabolic bands at Γ, the 2-D E_1 point by valence and conduction bands which are parallel along the <111> direction and parabolic in the two transverse directions, and the 1-D E_2 point by valence and conduction bands which are parallel in two orthogonal directions while parabolic in the third (since the position of the E_2 point is unknown in his model, the directions for the E_2 expansions are not specified). As can be seen from this synopsis of Cardona's model, there are similarities between it and our partition approach. Both models split the zone into the Γ, X, and L regions and use $\vec{k} \cdot \vec{p}$ theory to calculate the matrix elements at Γ and L. However, our method is based on a many-band $\vec{k} \cdot \vec{p}$ approach, while Cardona's model only uses two bands for his expansions. Furthermore, for the E_2 peak Cardona uses phenomenological arguments to arrive at a 1-D model for an unknown position in k-space, while in our partition method the results of nonlocal pseudopotential calculations including spin orbit effects are used to model accurately the band structure around different expansion points and, especially, the $\vec{k}$ point (3/4, 1/4, 1/4) which is found to give rise to the E_2 peak.[37,51-52] Hence, our approach generalizes Cardona's model and places it on a more rigorous and numerically accurate basis by providing analytical expressions for the energy bands and matrix elements for any point in the zone. In the following section we discuss the $\vec{k} \cdot \vec{p}$ method in general and derive our energy band expansions for the Γ, X, and L points of bulk III-V compounds.

2.2 $\vec{k} \cdot \vec{p}$ Method and Expansions

2.2.a General Methodology

$\vec{k} \cdot \vec{p}$ band theory for III-V compounds and expansions for the Γ, X, and L symmetry points have been derived previously by Kane,[38] Dresselhaus,[53] and Cardona.[39] All three authors have discussed the Γ region expansion in detail, while only simplified

expansions were presented for the X and L points. However, in order to follow our derivation of the X and L point expansions, it is best to understand the $\vec{k} \cdot \vec{p}$ method and to see it applied to the simpler Γ point expansion. Consequently, the important highlights of the $\vec{k} \cdot \vec{p}$ method and the Γ region expansion will be discussed; whereas, the reader is referred to papers by Kane[38] and Dresselhaus[53] for details.

In terms of a complete set of basis function $u_n(\vec{k}_o)$ at the point $\vec{k}_o$, the energies and eigenvectors at any point in $\vec{k}$-space can be obtained by solving the $\vec{k} \cdot \vec{p}$ matrix equation:[38]

$$\sum_{n'} \left\{ \left[E_n(\vec{k}_o) + \frac{\hbar^2}{2m_o}(k^2 - k_o^2) \right] \delta_{nn'} + \frac{\hbar}{m_o}(\vec{k} - \vec{k}_o) \cdot \vec{P}_{nn'} + H^{so}_{nn'} \right\} c_{n'n} = E_n(\vec{k}) c_{nn} \qquad (1)$$

$$\vec{P}_{nn'} = \int_{\substack{\text{unit} \\ \text{cell}}} u^*_{n\vec{k}_o}(\vec{r})\, \vec{p}\, u_{n'\vec{k}_o}(\vec{r})\, d^3\vec{r} \qquad (2)$$

where

$$u_{n\vec{k}}(\vec{r}) = \sum_{n'} c_{n'n}\, u_{n'\vec{k}_o}(\vec{r}) \qquad (3)$$

In the above, m_o is the free electron mass, n and n' are band indices, $\vec{p}$ is the electron momentum, and $E_n(\vec{k}_o)$ is the energy and $\vec{P}_{nn'}$ is the momentum matrix element at the point $\vec{k}_o$. Since the spin orbit interaction has a noticeable effect on the band structure of many semiconductors, we added onto the $\vec{k} \cdot \vec{p}$ Hamiltonian the spin orbit energy H^{so}, which consists of two terms[38]

$$H^{so} = \frac{\hbar}{4m_o^2c^2} \left[(\vec{\nabla}V \times \vec{p}) + (\vec{\nabla}V \times \vec{k}) \right] \cdot \vec{\sigma} \qquad (4)$$

where V is the crystal potential, c is the speed of light, and $\vec{\sigma}$ is the Pauli spin operator. Because the main contribution to the spin orbit interaction comes from the core region of the atom where $\vec{p}$ is many times larger than $\vec{k}$, we only include the $\vec{k}$-independent spin orbit interaction in our Hamiltonian.

In order to evaluate the dielectric constant for energies less than 6 eV, it is reasonable to restrict the calculation to transitions between band-edge states where the transition rates are the largest. Consequently, in performing the energy expansions about Γ, X, and L we treat the band edge states exactly, i.e., the $u_n(\vec{k}_o)$ of Eq. (3), and incorporate the effects of the other bands (Löwdin states) using a perturbation technique described by Löwdin.[38,54] These renormalizations are performed by including only those bands which give the largest contributions. This approximation results in a slight overestimation of the matrix elements involving these bands. This point will be discussed in more detail later in this chapter. In all of our Löwdin states, we find it necessary to add d-symmetry states onto those states of p-symmetry in order to obtain the correct energy-band curvatures. This idea was suggested by Chadi[35,55] who showed from pseudopotential calculations that there is appreciable mixing of d-symmetry states into the p-symmetry states; and, in a type of tight-binding calculation, he determined that the addition of d-symmetry states to an s-p basis set resulted in more accurate wavefunctions and energy bands.

2.2.b Γ Point Expansion

The basis set includes the three p-symmetry valence bands, the lowest s-symmetry conduction band, and the three lowest p-symmetry conduction bands as the additional Löwdin states. The seven wavefunctions are

$$\Gamma_{15}\begin{cases} -\frac{1}{\sqrt{2}}(x+iy)\downarrow \\ z\uparrow \\ \frac{1}{\sqrt{2}}(x-iy)\downarrow \end{cases} \qquad (5a)$$

Γ_1^c is $s^c\uparrow$

$$\Gamma_{15}^{c}\left\{\begin{array}{l} -\frac{1}{2}\left|(x^{c}+iy^{c})+(d_{yz}^{c}+id_{xz}^{c})\right|\downarrow \\ \frac{1}{\sqrt{2}}(z^{c}+d_{xy}^{c})\uparrow \\ \frac{1}{2}\left|(x^{c}-iy^{c})+(d_{yz}^{c}-id_{xz}^{c})\right|\downarrow \end{array}\right. \tag{5b}$$

where we have labeled the wavefunctions using single group symmetry notation. The superscript c signifies a conduction band wavefunction (no superscript implies a valence band wavefunction). x, y, and z are the three orthogonal components of the p-symmetry wavefunction, and d_{xy}, for example, denotes one of the five spherical harmonics of the d-symmetry wavefunctions. Each of the seven states are orthonormal and there is another degenerate set of seven states with the spin flipped. To obtain the energy dispersion relations for the states of Eq. (5a), we diagonalized the following renormalized Hamiltonian matrix resulting from the above basis set:

$$\begin{vmatrix} E_c+\frac{A'k^2}{2}+\frac{\hbar^2k^2}{2m_o} & 0 & kP' & 0 \\ 0 & \frac{B'k^2}{2}-\frac{2\Delta}{3}+\frac{\hbar^2k^2}{2m_o} & \frac{1}{3}\sqrt{2}\Delta & 0 \\ kP' & \frac{1}{3}\sqrt{2}\Delta & -\frac{1}{3}\Delta+\frac{\hbar^2k^2}{2m_o} & 0 \\ 0 & 0 & 0 & \frac{B'k^2}{2}+\frac{\hbar^2k^2}{2m_o} \end{vmatrix} . \tag{6}$$

In Eq. (6) we chose the k vector to lie along the z-direction (by symmetry it can lie along any direction) and the top of the valence band is taken as the zero of energy. E_c is the band gap at the Γ point, Δ is the spin orbit constant, the parameter P' results from the direct interaction of the s and p wavefunctions, and the coefficients A' and B' are due to Löwdin renormalization involving the Γ_{15}^{c} states and are defined similarly to L, M, and N of Dresselhaus et al.[56] The interaction matrix of Eq. (6) is very similar in form to the one given by Kane.[38] The constants Δ, P', A', and B' are defined by

$$\Delta = \frac{3\hbar i}{4m_o^2c^2}\left\langle x\left|\frac{\partial V}{\partial x}p_y-\frac{\partial V}{\partial y}p_x\right|y\right\rangle$$

$$P' = \frac{\hbar}{m_o} \langle is^c \mid p_z \mid z \rangle \tag{7}$$

$$A' = \frac{\hbar^2}{m_o^2} \frac{\mid \langle is^c \mid p_z \mid z^c \rangle \mid^2}{E_1^c - E_{15}^c} \tag{8}$$

$$B' = \frac{\hbar^2}{m_o^2} \frac{\mid \langle x \mid p_z \mid id_{xz}^c \rangle \mid^2}{E_{15} - E_{15}^c}$$

In Eq. (8), E_1^c, for example, is the energy of the Γ_1^c state. The Löwdin coefficients normally involve sums over all bands of a certain symmetry type that interact with the s- and p-symmetry wavefunctions;[54] however, we chose to include only the largest terms in the sums. The parameters E_c, Δ, P', A', and B' are determined empirically by numerically solving the eigenvalue equation in order that the $\vec{k} \cdot \vec{p}$ band structure has the correct band-edge, energy splittings and effective masses. The value of these parameters, as well as those for the X and L point expansions, for GaAs are listed in the Appendix. As stated previously, the energy gaps and effective masses are either experimental values or determined from nonlocal pseudopotential calculations which include spin orbit effects. The pseudopotential energy gaps resemble those of Chelikowsky and Cohen;[40] the band edge effective masses are given at the end of this section.

2.2.c X Point Expansion

The eight X point basis states are

$$X_5 \begin{cases} iz\uparrow \\ y\uparrow \end{cases}$$

$$X_1^c \quad s^c \uparrow \tag{9a}$$

$$X_3^c \quad \frac{1}{\sqrt{2}}(ix^c + id_{yz}^c)\uparrow$$

$$X_1 \quad \frac{1}{\sqrt{2}}(s + f_{xyz})\uparrow$$

$$X_3 \ \frac{1}{\sqrt{2}}(ix+id_{yz})\uparrow \qquad (9b)$$

$$X_5^c \begin{cases} iz^c\uparrow \\ y^c\uparrow \end{cases}$$

where the states listed in Eq. (9a) are treated exactly while those in Eq. (9b) are incorporated by Löwdin renormalization. In Eq. (9) we chose the <100> axis to lie along the x-direction. Again the d-symmetry states are included in order to obtain a better empirical fit, and the X_1 wavefunction has an f-symmetry state for reasons analogous to those discussed previously for the d-symmetry states.[35,55] The same band structure results from the above basis set with spin down. Because the energy gaps at the X point for III-V semiconductors are large, we find it reasonable to diagonalize two 2x2 matrices instead of one 4x4 matrix in order to obtain the energy dispersion relations for the states of Eq. (9a). The resulting 2x2 matrices are

$$\begin{vmatrix} k_z^2[(E1)+\frac{1}{2}(E2)] + \frac{\hbar^2k^2}{2m_o} & \frac{1}{2}\Delta' \\ \frac{1}{2}\Delta' & \frac{1}{2}k_z^2(H'+I)+\frac{\hbar^2k^2}{2m_o} \end{vmatrix} \qquad (10a)$$

$$\begin{vmatrix} E_{3,x}^c + \frac{1}{4}Dk_x^2 + \frac{1}{2}k_z^2(-H' + G) + \frac{\hbar^2k^2}{2m_o} & k_x\left|\frac{F(E_{1,x}^c - E_{5,x}^c)}{2}\right|^{1/2} \\ k_x\left|\frac{F(E_{1,x}^c - E_{5,x}^c)}{2}\right|^{1/2} & E_{1,x}^c + \frac{(E1)(E_{5,x} - E_{1,x}^c)k'^2_x}{2(E_{1,x}^c - E_{3,x})} + k_z^2[F-(E1)] + \frac{\hbar^2(k'^2_x + k_z^2)}{2m_o} \end{vmatrix} . \qquad (10b)$$

Equations (10a) and (10b) are for the band-edge valence and conduction bands, respectively. In Eq. (10) we chose the z-direction as the arbitrary (neglecting the anisotropy) perpendicular direction and the top of the valence band as the zero of energy. k_x and k_z are the $\vec{k}$ vectors along the <100> and z-directions, respectively, and $k'_x = k_x - k_m$, where k_m corrects for the X_1^c minimum not being exactly at the X point. k_m is determined empirically from the pseudopotential calculations. Δ' is the spin orbit constant defined analogously to Δ of Eq. (7) and $E_{1,x}^c$, for example, is the relative energy of

the X_1^c state. D, E1, E2, F, G, H′, and I are the Löwdin coefficients and are defined similarly to A′ and B′ in Eq. (8). The parameters in Eq. (10) are fitted empirically by computer so that the X_1, X_3,X_5,X_1^c, and X_3^c bands all have the correct relative position and dispersion relations (see Appendix for their values in GaAs).

2.2.d L Point Expansion

The ten L point basis states are

$$\begin{aligned}
&L_3\ \frac{i}{\sqrt{2}}(x-y)\uparrow \\
&L_3\ \frac{1}{\sqrt{6}}(2z-x-y)\uparrow \\
&L_1^c\ \ s^c\uparrow
\end{aligned} \tag{11a}$$

$$\begin{aligned}
&L_1\ \frac{1}{\sqrt{2}}(s+f_{xyz})\uparrow \\
&L_1\ \frac{1}{\sqrt{6}}(x+y+z+d_{xy}+d_{xz}+d_{yz})\uparrow \\
&L_3^c \begin{cases} \frac{i}{\sqrt{2}}(x^c-y^c+d_{yz}^c-d_{xz}^c)\uparrow \\ \frac{1}{\sqrt{12}}(2z^c-x^c-y^c+2d_{xy}^c-d_{yz}^c-d_{xz}^c)\uparrow \end{cases} \\
&L_2^c\ \frac{i}{\sqrt{6}}(x^c+y^c+z^c+d_{xy}^c+d_{xz}^c+d_{yz}^c)\uparrow \\
&L_3^c \begin{cases} \frac{1}{\sqrt{6}}(2d_{z^2}^c-d_{x^2}^c-d_{y^2}^c)\uparrow \\ \frac{i}{\sqrt{2}}(d_{x^2}^c-d_{y^2}^c)\uparrow \end{cases}
\end{aligned} \tag{11b}$$

where the states listed in Eq. (11a) are treated exactly and those in Eq. (11b) are incorporated using Löwdin renormalization. For convenience, we took the spin quantization axis to be the <111> axis and transformed Eq. (4) into the <111> coordinate system, i.e.,

$\frac{1}{\sqrt{3}}(\hat{i}+\hat{j}+\hat{k})$ is the z-axis. Using this coordinate system for the spin orbit interaction, H_{so} only connects L_3 states having the same spin. The basis set with spin down is degenerate with the states listed in Eq. (11).

Similar to the X region treatment, because of the large band gap at the L point, we diagonalized a 2x2 matrix consisting of the two upper valence bands and considered separately the lowest conduction band. The 2x2 matrix is written as

$$\begin{vmatrix} \frac{1}{2m_o}\hbar^2k^2+\frac{1}{6}Tk_l^2+\frac{1}{3}k_t^2(T+\frac{1}{2}V') & \frac{1}{2}\Delta'' \\ \frac{1}{2}\Delta'' & \frac{1}{2m_o}\hbar^2k^2+\frac{1}{6}Tk_l^2+k_t^2\left|\frac{1}{3}T+\frac{1}{2}U+\frac{1}{6}(V'+W)-\frac{S'(E^c_{1,L}-E_{1,L})}{(E^c_{1,L}-E_{3,L})}\right| \end{vmatrix} \quad (12a)$$

and the energy dispersion relation for the L_1^c band is

$$E = E^c_{1,L}+\frac{1}{2m_o}\hbar^2k^2+\frac{1}{2}k_l^2(R'+S')+k_t^2\left|\frac{S'(E^c_{1,L}-E_{1,L})}{(E^c_{1,L}-E_{3,L})}+\frac{R'(E^c_{1,L}-E^c_{2,L})}{2(E^c_{1,L}-E^c_{3,L})}\right| . \quad (12b)$$

In Eq. (12) k_l and k_t are the longitudinal and transverse k basis vectors, respectively. k_l is taken along the L-Γ direction and k_t is arbitrarily, by symmetry and neglecting the anisotropy, taken along the L-W direction. In analogy with the X-region treatment, Δ'' is the spin orbit constant; $E^c_{1,L}$ is the relative energy of the L_1^c state, for example; and R', S', T, U, V', and W are the Löwdin coefficients. Again, the parameters are fitted empirically so that the L_1, L_2, L_3, and L_1^c bands have the correct relative positions and dispersion relations and their values for GaAs are listed in the Appendix.

2.2.e. Effective Masses

Table 1 lists the low temperature (5 K - 77 K) values of the band-edge effective masses at the three symmetry points for the five III-V compounds. Presented are the longitudinal and transverse masses for the X and L states and the density of states masses for the Γ states. When experimental data are not available, the masses are calculated using the results of nonlocal pseudopotential calculations which include the spin orbit interaction.

Table 1: Low temperature theoretical and experimental band-edge masses at the Γ, X, and L symmetry points. Each of the experimental masses is referenced. For Γ only the density of states masses is given while for X and L both the longitudinal and transverse masses are presented.

		GaAs	AlAs	InAs	InP	GaP
Γ_1^c	m^*	0.067[a]	0.140	0.023[b,c]	0.077[b]	0.122
Γ_{hh}	m^*	−0.510[a]	-0.536	−0.40[d]	−0.58[e]	−0.56[e]
Γ_{lh}	m^*	−0.082[a]	-0.087	−0.026[d]	−0.12[e]	−0.16[e]
Γ_{so}	m^*	−0.154[a]	-0.217	-0.166	-0.179	-0.289
L_6^c	m_l	1.854	1.592	2.333	2.149	1.988
	m_t	0.136	0.157	0.143	0.144	0.147
$L_{4,5}$	m_l	1.731	2.011	1.688	2.021	1.948
	m_t	-0.277	-0.290	-0.308	-0.295	-0.278
L_6	m_l	1.731	2.011	1.668	2.021	1.948
	m_t	-0.277	-0.290	-0.308	-0.295	-0.278
X_7^c	m_l	0.495	0.385	0.593	0.566	0.551
	m_t	0.258	0.254	0.305	0.279	0.249
X_6^c	m_l	2.100	1.158	4.516	2.772	1.70[f]
	m_t	0.277	0.268	0.307	0.278	0.191[f]
X_7	m_l	1.209	1.300	1.236	1.341	1.258
	m_t	-0.744	-0.659	-1.109	-0.839	-0.628
X_6	m_l	1.209	1.300	1.236	1.341	1.258
	m_t	-0.744	-0.659	-1.109	-0.839	-0.628

a Reference 57
b Reference 58
c Reference 59
d Reference 60
e Reference 61
f Reference 62

These masses along with the energy gaps are used to determine the direct interaction and Löwdin coefficients at the three symmetry points. Instead of taking the masses directly from the energy band curvatures, a technique with a fair amount of uncertainty, the mass m^* at the point k_o is calculated using[38]

$$\frac{1}{m^*} = \frac{1}{m_o} + \frac{2\hbar^2}{m_o^2} \sum_{n'}' \frac{|\vec{s} \cdot \vec{\nabla}_{nn'}|^2}{E_n(\vec{k}_o) - E_{n'}(\vec{k}_o)} \tag{13}$$

where s is a unit vector in the direction of a principal axis, $\vec{\nabla}_{nn'}$ is the gradient operator between the states n and n′ at the point k_o, and the summation is over all $n' \neq n$.

In order to test the accuracy of our masses, we calculated the conduction band masses at Γ for GaAs, InP, and InAs for which experimental data are available. The masses are 0.070, 0.075, and 0.028 for GaAs, InP, and InAs, respectively. As can be seen, our calculated masses compare favorably with the experimental data.

2.3 Dielectric Constant and Partition Method Formalism

The dielectric constant is calculated as the sum of interband optical transitions. Ignoring phonon assisted transitions and the exciton contribution, the real part of the transverse dielectric constant in the long wavelength limit is given by[63]

$$\epsilon_1(\omega) = 1 + \frac{8\pi e^2 \hbar^2}{m_o^2} \sum_{\vec{k}_i, \vec{k}_f, c, v} \frac{|\hat{e} \cdot P_{cv}(\vec{k})|^2}{(E_{\vec{k}_{f,c}} - E_{\vec{k}_{i,v}})[(E_{\vec{k}_{f,c}} - E_{\vec{k}_{i,v}})^2 - \hbar^2\omega^2]} \tag{14}$$

where $P_{cv}(\vec{k})$ is the momentum (optical) matrix element defined in Eq. (2) between the initial and final states having wavevectors $\vec{k}_{i,v}$ and $\vec{k}_{f,c}$, respectively, e is the electronic charge, $\hat{e}$ is the unit polarization vector in the direction of the electric field, $E_{\vec{k}_{i,v}}$ and $E_{\vec{k}_{f,c}}$ are the initial and final states energies, respectively, and ω is the frequency of the electromagnetic field. In Eq. (14) it is assumed that the valence band is filled and the conduction band is empty.

Because of our restriction to band-edge transitions, we have to calculate both the

real and imaginary parts of the dielectric constant since the Kramers-Kronig dispersion relation[63] can be used to determine $\epsilon_1(\omega)$ given $\epsilon_2(\omega)$ only when $\epsilon_2(\omega)$ is known for a larger range of energies. Consequently, we also calculate the imaginary part of the transverse dielectric constant which can be written as[63]

$$\epsilon_2(\omega) = \frac{4\pi^2 e^2}{m_0^2 \omega^2} \sum_{\vec{k}_i, \vec{k}_f, c, v} |\hat{e} \cdot P_{cv}(\vec{k})|^2 \, \delta(E_{\vec{k}_f, c} - E_{\vec{k}_i, v} - \hbar\omega) \quad . \tag{15}$$

Equations (14) and (15) both contain a summation over energy bands and $\vec{k}$ states. As stated previously, we only consider transitions between the highest valence band states and the lowest conduction band states. Consequently, for the Γ region contribution, we include transitions between the upper three valence bands and the lowest conduction band, for the X region contribution, we include transitions between the upper two valence bands and the two lowest conduction bands, and for the L region contribution, we include transitions between the upper two valence bands and the lowest conduction band. In Figure 1 arrows on the GaAs band structure represent the aforementioned interband transitions. In our model both the L and X regions include the K and W points, even though Figure 1 shows only the K point as being part of the X region.

As a result of conservation of momentum, $\vec{k}_i = \vec{k}_f$, and, thus, we replace the double summation by a single one over the valence band wavevectors. For $\epsilon_2(\omega)$ the summation is only over $\vec{k}$-states for which there is energy conservation between the energy of the excitation and the energy difference between the valence and conduction bands. Therefore, $\epsilon_2(\omega)$ has contributions only from specific regions of the Brillouin zone and, thus, a measurement of $\epsilon_2(\omega)$ reveals properties specific to certain portions of the zone. On the other hand, $\epsilon_1(\omega)$ also allows virtual transitions, i.e., no conservation of energy, and, thus, all regions of the zone contribute to it. However, because of the energy denominator in Eq. (14), the most important transitions for a specific excitation energy are those for which there is approximately energy conservation. Consequently, transitions having energies which are significantly different from the excitation energy can be safely ignored, which

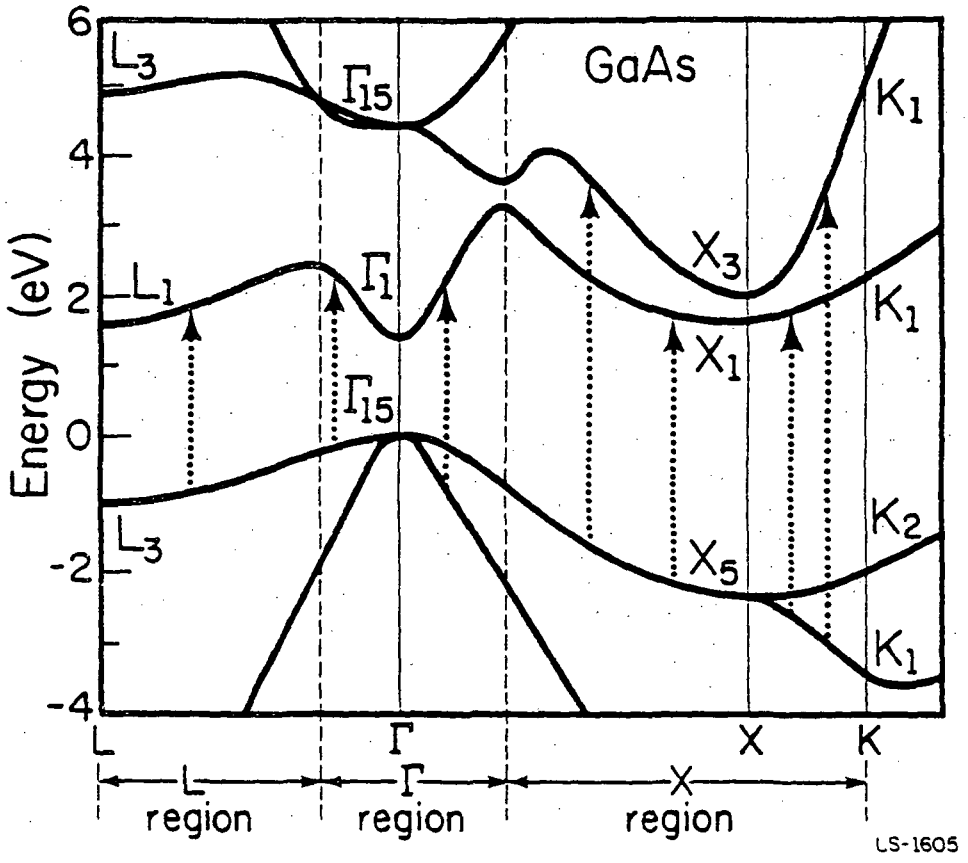

Figure 1. Optical transitions betwen the band-edge valence and conduction bands for the three regions, Γ, X, and L, for GaAs. Only these transitions are included in our model.

accounts for our decision to include only band-edge transitions in our model.

In order to calculate $\epsilon(\omega)$, the summation over $\vec{k}$-states is replaced by an integration over the first Brillouin zone. Since we calculate the dielectric constant by summing over the contributions of the regions around the Γ, X, and L points, the integration is performed separately for each region. The integration volumes for the Γ, X, and L regions are approximated by a sphere and two cones, respectively (see Figure 2). For GaAs, the volumes of these regions, taking into account the six-fold and eight-fold degeneracies of the X and L regions, respectively, are 8.24×10^{-2}, 1.35 and 4.01 $Å^{-3}$ for Γ, X, and L, respectively. The total volume of 5.44 $Å^{-3}$ is less than 1% different than the actual volume of the first Brillouin zone of GaAs.

Prior to performing the integrations for each region, it is necessary to determine analytical expressions for the energies and matrix elements. For Γ we assume the region to be isotropic and, hence, the energies are obtained directly from Eq. (6). To obtain the Γ region optical (momentum) matrix elements we use Eq. (2) in conjunction with Eqs. (6)-(8). More specifically, for the case of the transition between the heavy hole (hh) band and the first conduction (cond) band, the x- or y-component (by symmetry) of $P_{cv}(\vec{k})$ is

$$P^{x}_{hh,cond}(\vec{k}) = \frac{m_o N_1 N_4}{\hbar} \left| \frac{a_1 P'}{\sqrt{2}} + \frac{a_1 k}{2\sqrt{2}} \left| \frac{(A')(B')(E_1^c - E_{15}^c)}{(E_{15} - E_{15}^c)} \right|^{1/2} \right.$$

$$\left. + \frac{a_1 k}{2\sqrt{2}} \left| \frac{(A')(B')(E_{15} - E_{15}^c)}{(E_1^c - E_{15}^c)} \right|^{1/2} + \frac{c_1 k B'}{2\sqrt{2}} \right| \qquad (16)$$

where we have substituted the hh and cond band eigenvectors of the Eq. (6) matrix into Eq. (2). In Eq. (16) N_1 and N_4 are the normalization constants for the hh- and cond-band eigenvectors, respectively; a_1, b_1, and c_1 are the eigenvector coefficients for the cond band; and P', A', and B' are the direct interaction and Löwdin coefficients, respectively, from Eqs. (7)-(8).

For the X and L regions, the integrations and dispersion relations are calculated

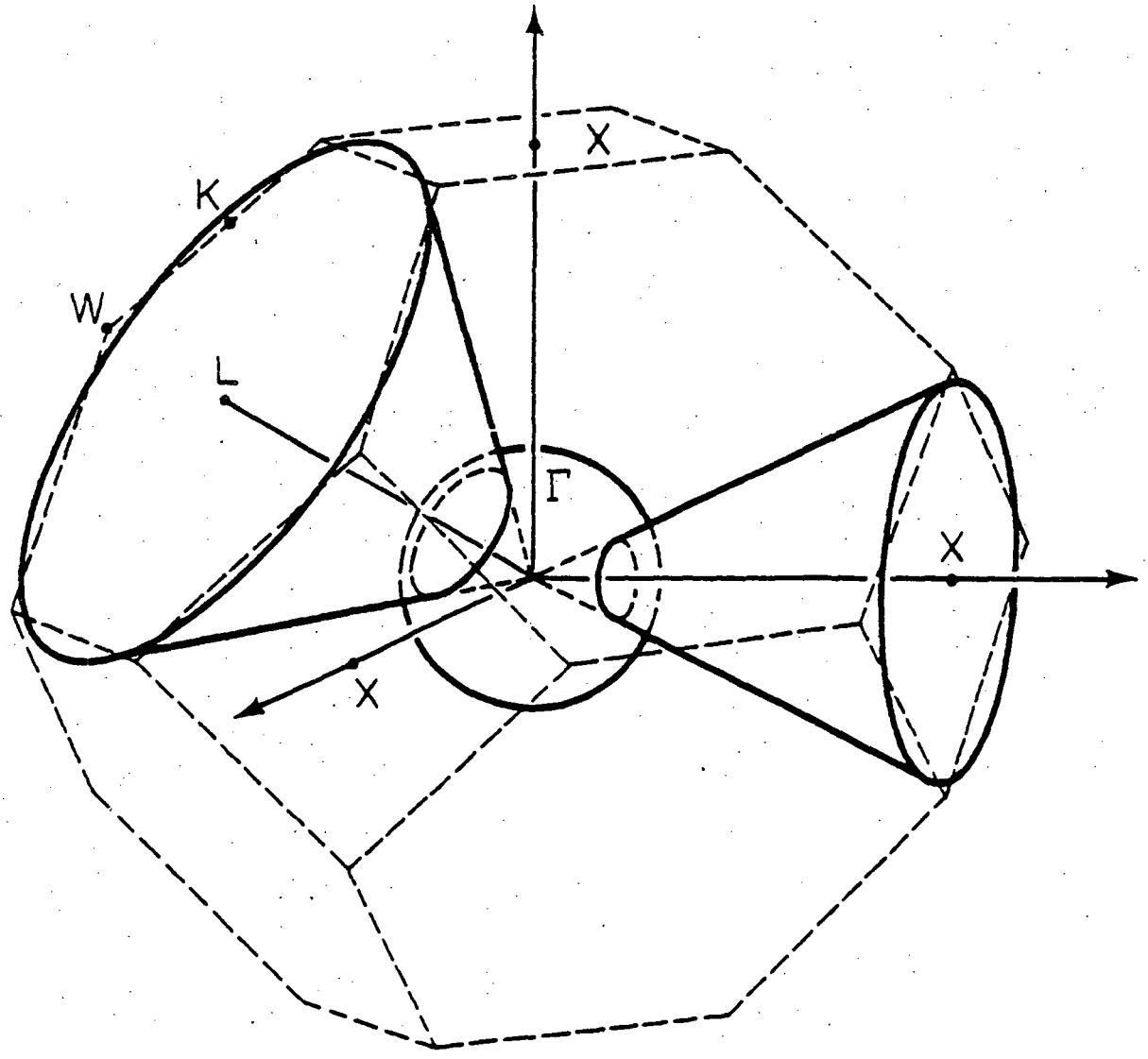

Figure 2. Partition of the first Brillouin zone of a zinc-blende lattice into the Γ, X, and L regions. The Γ region is a sphere while the X and L regions are both cones. The K and W points are also part of the X region.

analogously; therefore, we will only consider the case of the L region. On the zone-face containing the L point, we expand the energies and matrix elements from the L point towards both the K and W points. For energies closer to the L point, i.e., up to halfway between L and K, we evaluate Eqs. (12), while for those closer to K or W, we construct polynomial fits to the energy bands resulting from nonlocal pseudopotential calculations which include spin orbit effects. For the matrix elements we assume a constant value equal to the L point matrix elements (evaluated analogously to the derivation of Eq. (16)) for states closer to L and linearly interpolate between the two endpoint values, as obtained from the pseudopotential results, for states closer to K and W. Both of these matrix element approximations are borne out by pseudopotential calculations. In a similar fashion we expand from L, K, and W towards Γ, i.e., using Eq. (12) and a constant matrix element for the L expansion and the pseudopotential results with two matrix elements for the K and W expansions. By symmetry, it is only necessary to consider the region between the L-K and L-W lines. This type of structure repeats itself 8 and 12 times on the X and L zone-faces, respectively. For simplicity, the energies and matrix elements between the L-K and L-W lines are computed by linear interpolation. We also make the approximation that the volume between the L zone-face and the Γ point is to be modeled by a succession of shrinking hexagons, assuming the symmetry on the L zone-face to exist on each of the hexagons. For hexagons which are less than 0.65 of the distance from L to the edge of the Γ region, we assume the disperson relations along L-K and L-W are also valid along the pseudo L-K and L-W lines of each hexagon. For hexagons which are greater than 0.65 of the distance, the dispersion relations along the pseudo L-K and L-W lines are approximated by linearly interpolating between the values along the L-Γ line and those along the K-Γ or W-Γ lines. By comparing all of these interpolated values with those resulting from a nonlocal pseudopotential calculation, we have determined that our linear interpolation and shrinking hexagon schemes, in spite of their roughness, yield reasonable results.

Having obtained analytical expressions for the dispersion relations, we are able to

obtain the energies and matrix elements at a large number of mesh points using a small amount of computation time. The Γ region integration is straightforward because of its isotropy, while for the X and L regions we integrate numerically by dividing the irreducible volumes of these regions into approximately 32,000 rectangular cubes of varying sizes and shapes. The sizes and shapes are varied according to the density of states and to ensure that the integration is performed within the volume of the first Brillouin zone. Using this method, we fill the zone with over 4,000,000 mesh points, assuring us of satisfactory convergence and a lack of artifacts for an energy resolution of 0.1 eV. On a Harris 800 computer, the $\epsilon_2(\omega)$ curves presented in Section 2.4.a take approximately 15 minutes to generate.

Once $\epsilon_1(\omega)$ and $\epsilon_2(\omega)$ are known, the index of refraction $\eta(\omega)$ and the absorption coefficient $\alpha(\omega)$ can be easily determined. The index of refraction is given by[63]

$$\eta(\omega) = \left[\frac{\epsilon_1(\omega)}{2} + 1/2(\epsilon_1(\omega)^2 + \epsilon_2(\omega)^2)^{1/2} \right]^{1/2} . \tag{17}$$

The absorption coefficient is related to $\eta(\omega)$ and $\epsilon_2(\omega)$ via the relation[63]

$$\alpha = \frac{\omega\epsilon_2(\omega)}{c\eta(\omega)} \tag{18}$$

where c is the velocity of light.

2.4 Results and Discussions

2.4.a $\epsilon_2(\omega)$ for Five III-V Compounds

Figures 3a-e compare our calculated $\epsilon_2(\omega)$ curves with the experimental data of Aspnes and Studna.[64] As the theoretical curves are generated using low temperature (5 K) band structure data while the experimental data are obtained at 300 K, we have shifted the experimental curves by 0.1 eV in order to account for this difference. Experimental data do not exist for AlAs.

The most noticeable feature of all of the curves is the presence of the two well

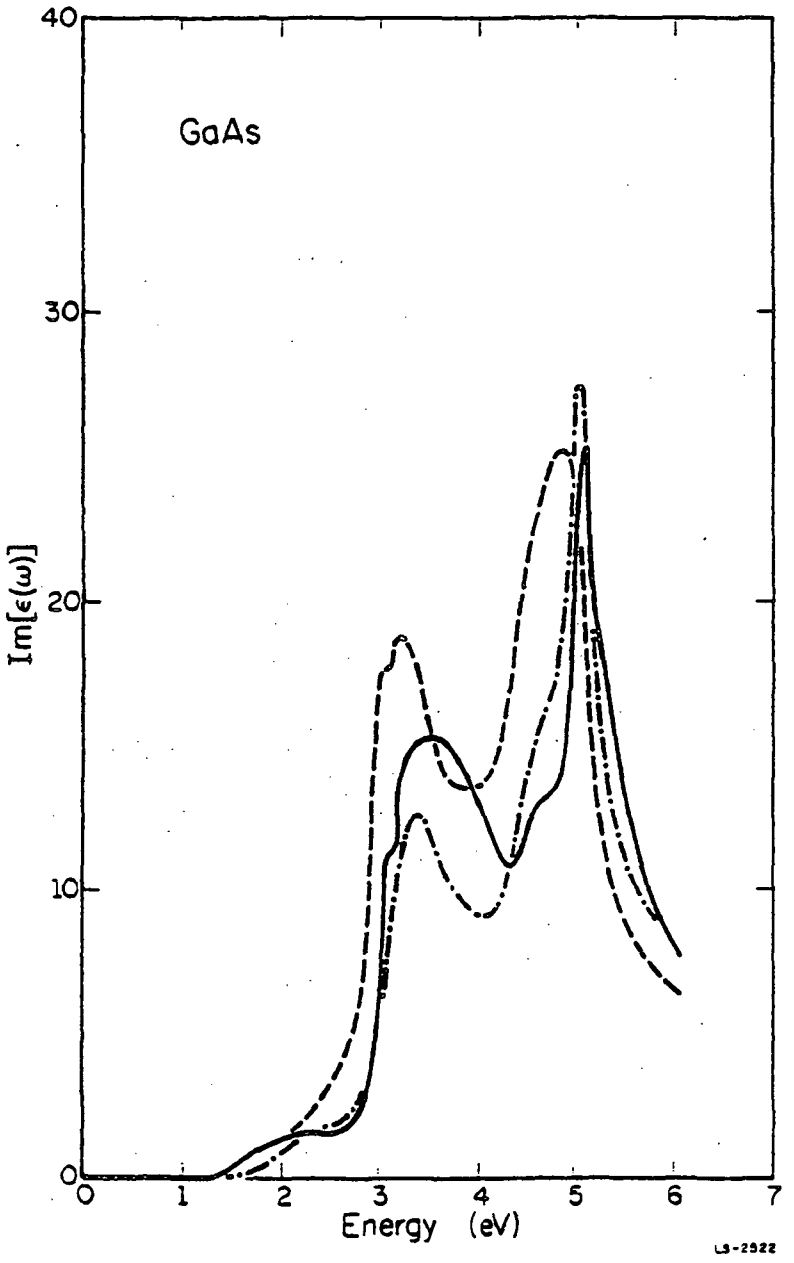

Figure 3a. Imaginary part of the dielectric constant of GaAs. The solid and dotted-dashed lines are calculated by the $\vec{k} \cdot \vec{p}$ and nonlocal pseudopotential methods, respectively, while the dashed line is the experimental results. The experimental data are extrapolated to 5 K.

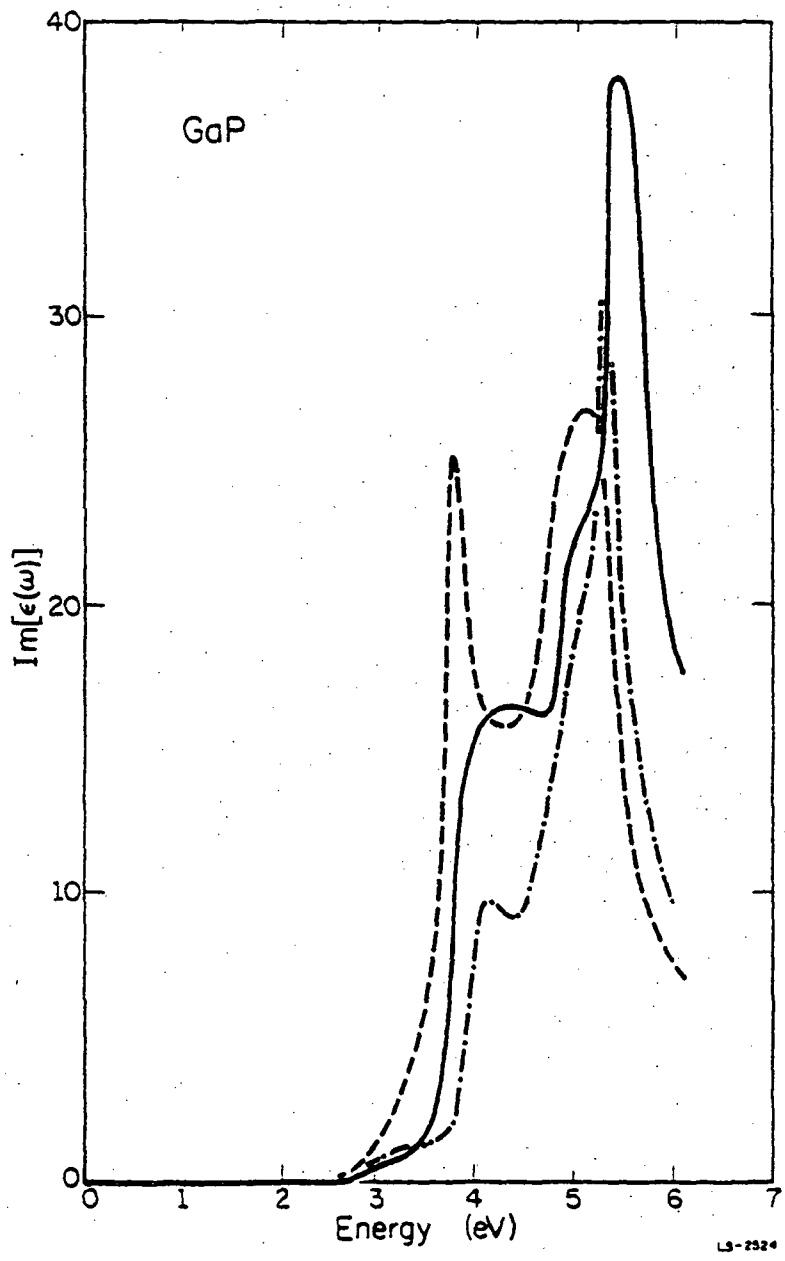

Figure 3b. Imaginary part of the dielectric constant of GaP. The solid and dotted-dashed lines are calculated by the $\bar{k} \cdot \bar{p}$ and nonlocal pseudopotential methods, respectively, while the dashed line is the experimental results. The experimental data are extrapolated to 5 K.

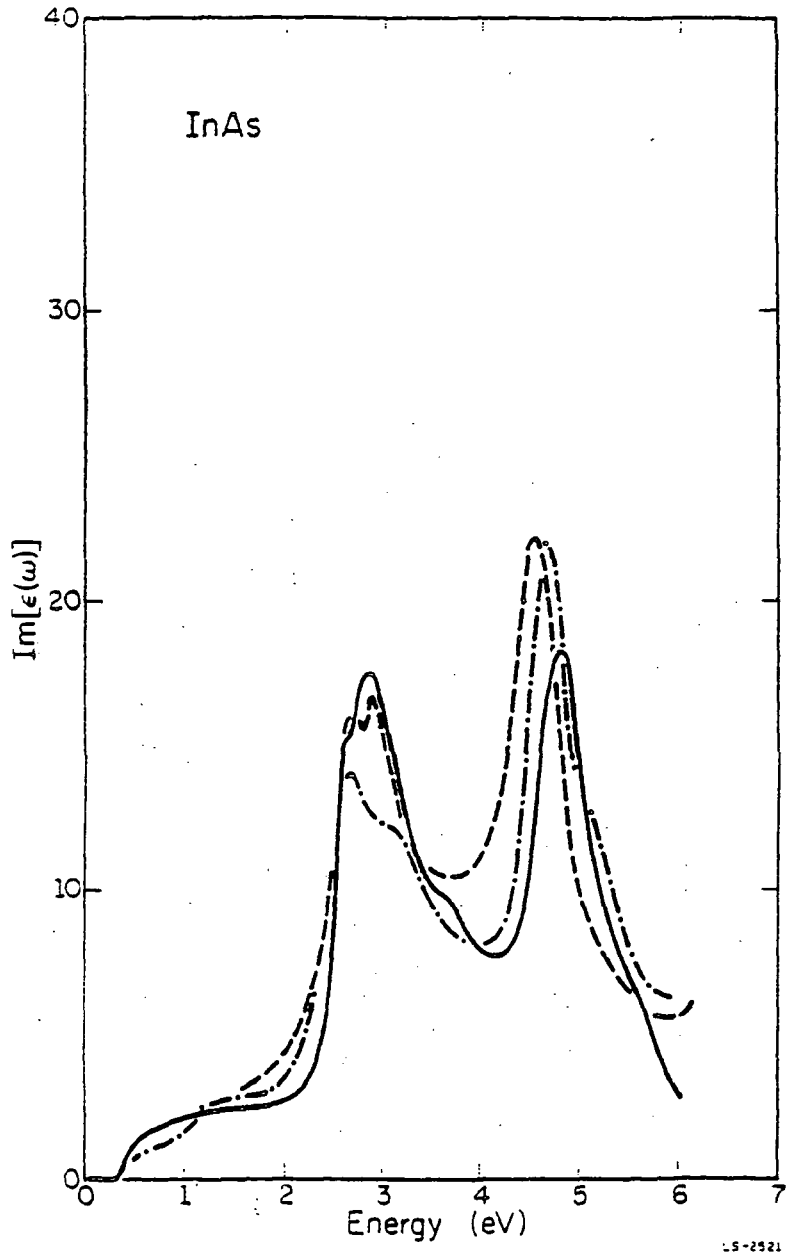

Figure 3c. Imaginary part of the dielectric constant of InAs. The solid and dotted-dashed lines are calculated by the $\vec{k} \cdot \vec{p}$ and nonlocal pseudopotential methods, respectively, while the dashed line is the experimental results. The experimental data are extrapolated to 5 K.

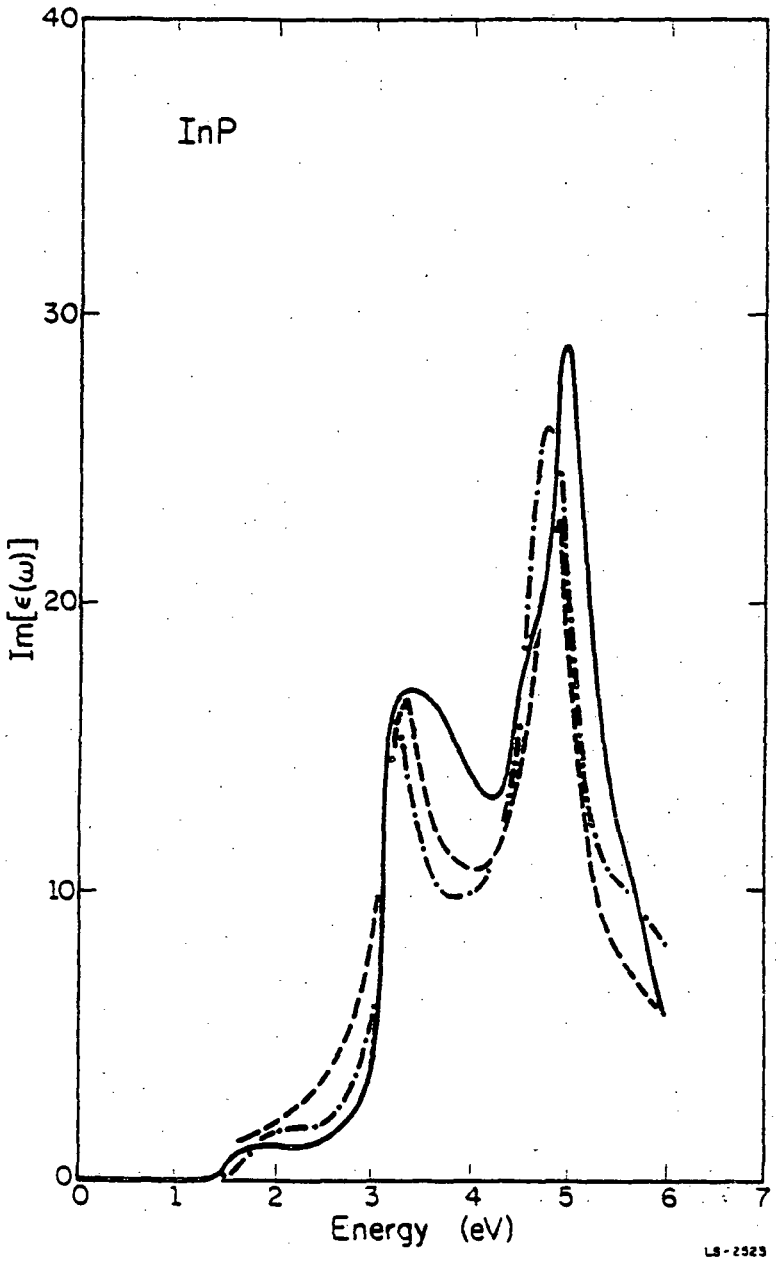

Figure 3d. Imaginary part of the dielectric constant of InP. The solid and dotted-dashed lines are calculated by the $\vec{k} \cdot \vec{p}$ and nonlocal pseudopotential methods, respectively, while the dashed line is the experimental results. The experimental data are extrapolated to 5 K.

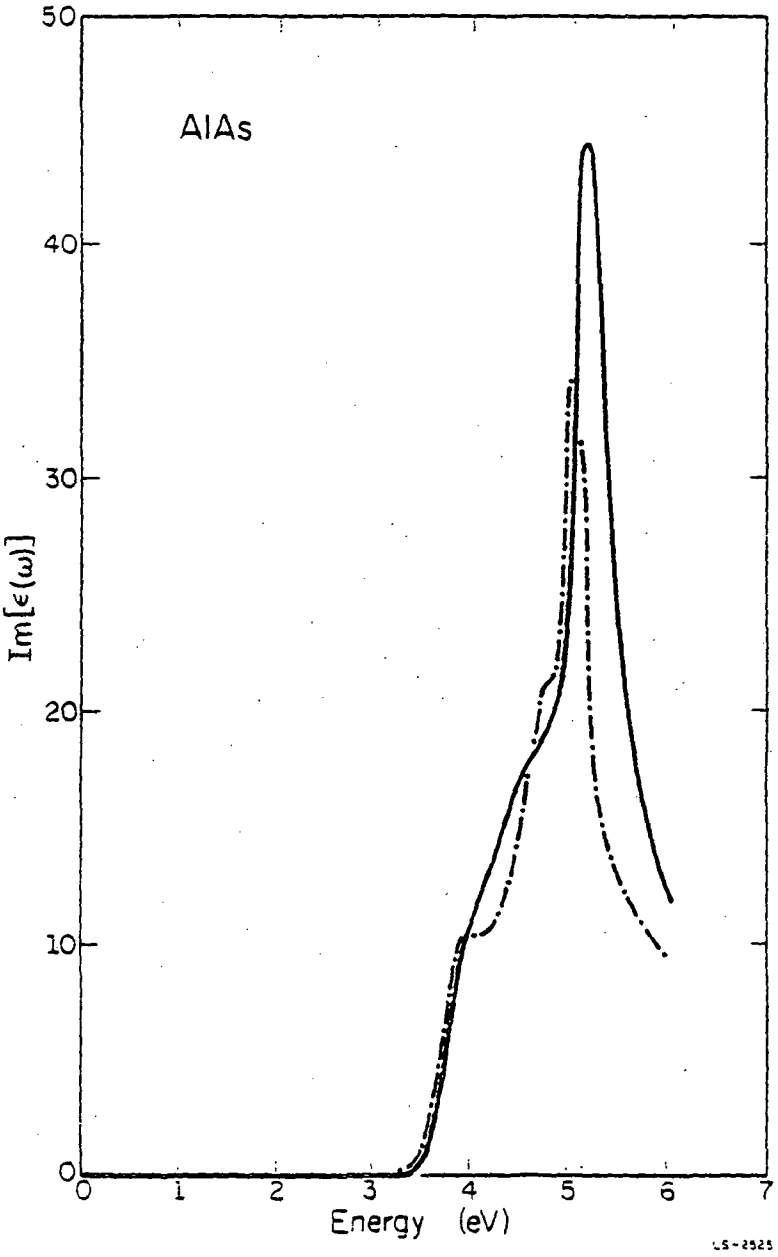

Figure 3e. Imaginary part of the dielectric constant of AlAs. The solid and dotted-dashed lines are calculated by the $\vec{k} \cdot \vec{p}$ and nonlocal pseudopotential methods, respectively, while the dashed line is the experimental results. The experimental data are extrapolated to 5 K.

known E_1 and E_2 peaks, as discussed previously in Sec. 2.1 in reference to Cardona's model.[39] The E_1 peak arises from transitions occurring over a large portion of the Brillouin zone around the L points. There is no E_1 peak for AlAs because the L and K point energy gaps differ by less than 1 eV; hence, the position of the AlAs E_1 peak overlaps with the low-energy slope of its E_2 peak. Except for InAs and GaAs for which our theoretical curves show a small structure due to the L point spin orbit splitting, the Ga and In compounds exhibit unsplit E_1 peaks which are broader than the experimental peaks. We believe that this occurs mainly because of the absence of excitons in our model. Exciton effects could have various consequences on the magnitudes of the E_1 peaks because they alter both the density of states and the optical matrix elements. According to Velicky and Sak[65] and Hanke and Sham,[66] excitons should sharpen and enhance the E_1 peak. We account qualitatively for their results by the following argument. Without excitons, the E_1 peak arises from transitions away from the L-Γ line because the band-edge conduction and valence bands along that line have small transverse masses and, correspondingly, small densities of states which are insufficient to support a peak. Consequently, the peak is shifted to higher energies where the phase space is larger. Exciton effects should lower the L gap and raise the transverse effective masses, resulting in higher densities of states along the L-Γ line. Thus, the structure of the line would be reflected in the shape of the E_1 peak, i.e., the peak would become split.

These ideas are corroborated by our theoretical results. The InAs band edge matrix elements are a factor of two smaller than those of GaP; however, InAs has the largest E_1 peak. Furthermore, its peak is the sharpest and the most centered of the four compounds. This occurs because its transverse energy band curvature is the smallest among these compounds; hence, the E_1 peak is supported mainly by transitions occurring close to the L-Γ line. However, for more precise imformation, an explicit calculation is required to determine the overall effect of excitons on the E_1 peak.

As discussed in Section 2.1, the E_2 peak originates from a region around the special

$\vec{k}$ point (3/4,1/4,1/4). From our calculations we find that the density of states in this region is more important than the magnitudes of the optical matrix elements in influencing the strength of the E_2 peak. Excitons should lower the E_2 peak.[65-66] A possible explanation is that excitons could disrupt the parallel band curvature in the vicinity of the special $\vec{k}$ point. This would lower the effective density of states in this region and, consequently, reduce the E_2 peak. The same exciton effect can account for the slight energy difference between the experimental and theoretical curves for GaAs, GaP, InAs, and InP.

The other regions of the Brillouin zone have small contributions to the dielectric constant in the 0 to 6 eV range. The Γ valley contribution is negligible because of its small phase space as shown in the previous section. The X region contribution is small because its phase space and matrix elements are, respectively, about a factor of three and two smaller than those of the L region.

2.4.b Comparison with Pseudopotential

Figures 3a-e also compare our results with those generated using a nonlocal pseudopotential calculation. The spin orbit interaction is not included in the pseudopotential calculations. For GaP, the effect of the omission is negligible; however, for the other four compounds, the spin orbit interaction effectively lowers the important band gaps by $\sim$ 0.1 eV. Consequently, for these four compounds, we have shifted the $\epsilon_2(\omega)$ curves so that the L-point, energy gaps agree with the spin orbit results.

The results of our model compare favorably with both the experimental and pseudopotential results. The magnitudes of our E_1 peaks are larger and more closely approximate the experimental peaks than those determined by the pseudopotential calculations. For GaAs, InAs, and InP, the E_2 peaks calculated by the $\vec{k}\cdot\vec{p}$ and pseudopotential methods are comparable in magnitude, but slightly shifted with respect to the experimental E_2 peaks, while for AlAs and GaP, the $\vec{k}\cdot\vec{p}$ peaks are substantially larger than the pseudopotential peaks. The discrepancy in the magnitudes of the E_1 and E_2 peaks

calculated by the $\vec{k}\cdot\vec{p}$ and pseudopotential methods can be attributed to the difference in the values of the optical matrix elements and to our linear interpolation approximation of the off-expansion line energies as discussed in Section 2.3. As stated previously, the $\vec{k}\cdot\vec{p}$ matrix elements involving the Löwdin states are overestimated due to the neglect of all but the closest higher bands of the proper symmetry.[67] However, we find that the band-edge $\vec{k}\cdot\vec{p}$ and pseudopotential matrix elements differ by only a few percent. This result agrees with the calculation of Hermann and Weisbuch[67] who found that the Γ-point, band-edge, matrix elements are insensitive to the higher band contributions. Since the band-edge matrix elements determine the low-frequency dielectric constant, the discrepancy in the peaks is, therefore, largely the result of our linear interpolation approximation. The problem with this approximation is that although it provides a good average energy dispersion relation, it sometimes produces a poor value for the density of states. This discrepancy also accounts for the difference in the shapes of the two curves. Nevertheless, despite the approximations involving the matrix elements and energy dispersion relations, the results of the two models are comparable for GaAs, InAs, and InP and assert the validity of our partition model.

2.4.c $\epsilon_1(0)$ for Five III-V Compounds

In Table 2 we give $\epsilon_1(0)$ at 5 K for the five III-V compounds. We also list the experimental values and the individual contributions of the three regions. Only the GaAs experimental data are 5 K values; for the other four compounds the values are extrapolated from 300 K using the GaAs $\epsilon_1(0)$ temperature dependence. The theoretical values are uniformly low, with an average error of $\sim$ 7.5%. The error is partly due to the omission of all high-energy transitions. The errors for AlAs, InP, and GaP are small because of the overestimation of the contributions of the virtual transitions corresponding to the E_2 peak. This effect is particularly pronounced for GaP where the strength of the E_2 transitions compensates for the small contribution from the E_1 transitions. For GaAs, the error results

Table 2. Theoretical and experimental $\epsilon_1(0)$ values at 5 K for five III-V compounds. Also included are the calculated individual contributions of the Γ, X, and L regions to $\epsilon_1(0)$ for each of the five compounds.

				Contributions of the three regions.		
Matl.	$\epsilon_1(0)$-theory	$\epsilon_1(0)$-expt.	% error	L	X	Γ
GaAs	8.68	10.60	18.1	6.01	1.25	0.41
AlAs	7.42	7.90	6.1	5.12	1.16	0.14
InP	9.13	9.27	1.5	6.68	1.12	0.33
InAs	10.10	11.49	12.1	7.26	0.94	0.91
GaP	8.77	8.80	0.4	6.30	1.21	0.25

also from its weak E_1 contribution. For InAs the error is ~ 12% in spite of its large E_1 peak. This probably stems from the fact that its E_2 peak is small and $\epsilon_1(0)$ of this small gap material is affected most by the neglect of higher band contributions in our model.

The valley contributions are split up according to the partition of the Brillouin zone as presented in Section 2.3. For all materials, the L region contributes approximately 60-70% to the total value of the dielectric constant while the Γ region accounts for about 5-10%. This general trend is also confirmed for optical frequencies corresponding to the Γ energy gap. Thus, the index of refraction is essentially determined by the band structure away from the center of the Brillouin zone, in agreement with the model of Cardona[39] discussed in Section 2.1.

In conclusion we have developed a general model for the dielectric constant and, thus, the optical parameters of III-V compounds using a hybrid approach which combines the $\vec{k}\cdot\vec{p}$ method with a nonlocal pseudopotential calculation to partition the bulk Brillouin zone into three regions. The results for the absorption coefficient and refractive index of bulk III-V compounds compare well with those for other one-electron band structure models. In contrast to other models, the partition method enables us to determine easily

the dependence of the dielectric constant on the form of the band structure. The other main advantage of this method is its flexibility, enabling it to analyze more complex structures and materials, such as alloys and heterostructures, as will be shown in Chapters 3 and 4, respectively.

3. EXTENSION OF THE PARTITION METHOD TO III-V ALLOY COMPOUNDS

3.1 Introduction

Because of the ability to tailor the electronic and optical properties of III-V alloy compounds by varying the alloy composition, these compounds have seen widespread application in such diverse optoelectronic devices as heterostructure lasers.[2,6,7] III-V alloy lasers and light emitting diodes (LEDs),[68-69] photodetectors.[11,70-71] and solar cells.[72-73] Consequently, the determination of the electronic and optical properties of these compounds as a function of composition is technologically important. The most simplistic approach to this problem is to invoke the virtual crystal approximation (VCA).[74] Alloy calculations based on the VCA have been performed using the empirical[75] and model,[76] local pseudopotential techniques and the dielectric method of Phillips.[77-78] In the VCA the alloy is treated as a perfectly periodic crystal having an average potential at each sublattice site, thus, ignoring the effects of fluctuations in the crystal potential and lattice site positions caused by the random arrangement of the atoms. However, these fluctuations cause the electrons to scatter as they traverse the lattice, leading to modifications of the VCA electron wavefunctions. These modifications manifest themselves in a number of phenomena, such as localized states, band tailing, mobility edges, and the variation of the energy gaps and absorption coefficient with the alloy composition. VCA models do predict some of these effects; however, the magnitudes of the trends are normally only correct for very small, aperiodic potentials.

Consequently, it is necessary to resort to a theoretical model which can take the lattice site and potential fluctuations into account. One such technique is the supercell method.[79] In this approach a very large unit cell, encompassing many lattice sites, is assumed to be representative of an average volume of the alloy. By calculating the band structures resulting from randomly varying the potential at each lattice site in the supercell, an average band structure is obtained which reflects the effects of alloy disorder.

This method yields good results at the expense of large computational costs resulting from the use of large unit cells.

The more commonly used approach, which, however, is also computationally expensive and complex, is to use the Coherent Phase Approximation (CPA).[44,80-82] The advantages of the CPA are that it is valid for all alloy compositions when the aperiodicity is small, while being applicable to all sizes of the disorder potential when the concentration of one of the alloy components is small. The basic idea of the CPA is to replace the actual disorder potential by an effective or coherent, complex, energy-dependent potential which, on the average, produces the same electron scattering as the actual potential. The coherent potential can be obtained by forcing it to follow the criterion that, on the average, an electron propagating according to it should undergo no further scattering at each atomic site.[44] Because of the computational difficulties associated with a full CPA implementation and our desire to have a simple, intuitive, bulk, band-structure model, we chose to use a perturbation theory approach to the CPA, introduced by Stroud[45] and rederived by Baldereschi and Maschke.[46] for calculating the band structure of GaP_xAs_{1-x}.

In Section 3.2 we implement this pertubation theory approach for calculating the absorption coefficient of $Al_xGa_{1-x}As$. The results of nonlocal pseudopotential calculations are used as input to the perturbation expansions. Ting and Chang[82] show that it is necessary to add to the disorder-induced absorption, the effects due to phonon-assisted processes. Hence, in Section 3.3 we introduce the phonon-assisted absorption model of Dumpke et al.[83] In Section 3.4, the two models are combined and compared with the experimental results.

3.2 Perturbation Approach to the CPA

Both Stroud[45] and Baldereschi and Maschke[46] derived expressions for the modifications of an alloy's electronic band structure as a result of disorder effects. Stroud's[45] calculation was based on an expansion of the real part of the CPA self-energy to

first order in the atomic site potentials. Baldereschi and Maschke[46] obtained the analogous expression by calculating, via second order perturbation theory, the effects of an aperiodic potential on a VCA electronic band structure, calculated using a local pseudopotential approach. The expression they derived for an $A_xB_{1-x}C$ alloy is

$$E_n(\vec{k},x) = E_n^{(0)}(\vec{k},x) + x(1-x) \sum_{n',\vec{k}}{}' \frac{| <n,\vec{k},x | \delta | n',\vec{k}',x> |^2}{E_n^{(0)}(\vec{k},x) - E_n^{(0)}(\vec{k}',x)} \tag{19}$$

where x is the mole fraction of A atoms, δ is the atomic pseudopotential difference between atoms A and B, and $E_n^{(0)}(\vec{k},x)$ and $|n,\vec{k},x>$ are the VCA eigenvalues and eigenvectors, respectively, corresponding to a state having a wavevector $\vec{k}$ and a band index n. Also using perturbation theory, the CPA wavefunction $\Psi_n(\vec{k},x)$ associated with $E_n(\vec{k},x)$ can be written as

$$\Psi_n(\vec{k},x) = |n,\vec{k},x> + x(1-x) \sum_{n',\vec{k}}{}' \left| \frac{<n,\vec{k},x | \delta | n',\vec{k}',x>}{E_n^{(0)}(\vec{k},x) - E_n^{(0)}(\vec{k}',x)} \right| |n',\vec{k}',x>. \tag{20}$$

In Eqs. (19) and (20), the VCA wavefunctions and energies are determined from a nonlocal pseudopotential calculation. To obtain the form factors for $Al_xGa_{1-x}As$, for example, we linearly interpolate between the values for GaAs and AlAs. Because there is some latitude in fitting the pseudopotential parameters, we chose the AlAs parameters so that they are consistent with the GaAs parameters. More specifically, since the symmetric and antisymmetric form factors can be decomposed into the atomic contributions as shown below,

$$V^S = \frac{1}{2}(V^{Ga} + V^{As}) \tag{21a}$$

$$V^A = \frac{1}{2}(V^{Ga} - V^{As}) \tag{21b}$$

the AlAs band structure is fitted such that its As form factors are nearly equivalent to those for GaAs. An exact match cannot be obtained without sacrificing accuracy in the

AlAs band structure. The fitted form factors for both GaAs and AlAs at 300 K are given in Table 3.

Finally, the atomic pseudopotential difference is required for all values of $\vec{q}=\vec{k}-\vec{k}'$. This can be seen by writing $|n,\vec{k},x\rangle$ in its Bloch form, $u_{n\vec{k}}(\vec{r})e^{i\vec{k}\cdot\vec{r}}$. There are two parts to the nonlocal pseudopotential, a local part and its nonlocal correction. Since we use the empirical nonlocal pseudopotential formalism of Chelikowsky and Cohen,[40] the local potential is only determined for a few selected reciprocal lattice vectors, while the energy and momentum dependent nonlocal correction V_{NL} is the Fourier transform of a square well potential of the form

$$V_{NL}(r,E) = \sum_{l=0,2} A_l(E) f_l(r) P_l \tag{22a}$$

$$f_l(r) = \begin{cases} 1 & r < R_l \\ 0 & r \geq R_l \end{cases} \tag{22b}$$

In Eq. (22), l is the angular momentum, $A_l(E)$ is the energy-dependent well depth, R_l is the well width, and P_l is a projection operator for the l^{th} angular momentum component. We determined the complete q-dependence of the local potential by fitting the local model pseudopotential of Aymerich et al.[84] so as to reproduce the form factors of GaAs and

Table 3. Pseudopotential parameters for GaAs and AlAs at 300 K. α_0 and A_2 have units of Rydbergs (R_y). β_0 is unitless, and R_0 and R_2 have units of Angstroms.

	Form Factors (R_y)						Lattice
Compound	$V^S(\sqrt{3})$	$V^S(\sqrt{8})$	$V^S(\sqrt{11})$	$V^A(\sqrt{3})$	$V^A(\sqrt{4})$	$V^A(\sqrt{11})$	Contant (Å)
GaAs	-0.2204	0.0225	0.0621	0.0458	0.0317	0.0058	5.65
AlAs	-0.2010	0.0348	0.0700	0.0525	0.0327	-0.0029	5.65

	Nonlocal Parameters (square well)									
	Cation					Anion				
Compound	α_0	β_0	R_0	A_2	R_2	α_0	β_0	R_0	A_2	R_2
GaAs	0.0	0.0	0.0	0.126	1.22	0.0	0.0	0.0	2.285	1.22
AlAs	-0.03	0.0	1.27	0.013	1.21	0.053	0.0	1.06	2.087	1.21

AlAs. Their expression for the bare potential is[84]

$$V_b(r) = ae^{-Br^2}\sin(cr)/r - 2Ze^2/r \tag{23}$$

where Z is the number of valence electrons for the atom under consideration, i.e., 4 for Ga, and a, b, and c are disposable constants. Their $V_b(r)$ consists of a repulsive core term plus an attractive coulombic term. To obtain the pseudopotential, they screened the bare potential using the zero-frequency, dielectric function of Schulze and Unger[85] corrected for exchange through the Hubbard approximation.[86] The complete dielectric-screening function $\epsilon(q)$ can be written as[85]

$$\epsilon(q) = 1 + \frac{\epsilon_o - 1}{1 + L^2(\epsilon_o - 1)q^2}\left[\frac{1}{1 + 3q^2/4k_F^2}\right] \tag{24}$$

where ϵ_o is the optical dielectric constant, L is the Thomas-Fermi screening length, and k_F is the Fermi wavevector.

Having evaluated Eqs. (19) and (20), it is then straightforward to obtain the CPA energy band bowings and absorption coefficients. The bowing factors are the second term in Eq. (19), while inserting the energies and wavefunctions of Eqs. (19) and (20) into Eq. (15) yields $\epsilon_2(\omega)$ from which $\alpha(\omega)$ follows from Eq. (18). The index of refraction $\eta(\omega)$ in Eq. (18) is calculated by linearly interpolating between the bulk $\eta(\omega)$ values of GaAs and AlAs, obtained from the results of the bulk dielectric constant model presented in Chapter 2. The experimental results of Casey et al.[87] show that there is a slight downward bowing of the refractive index relative to the interpolated value calculated above; however, within the accuracy of our CPA model, the slight bowing can be neglected.

In evaluating $\epsilon_2(\omega)$ we ignored optical matrix elements P_{cv} between two perturbed states, i.e., the second term in Eq. (20), because their magnitudes are negligible compared to the other three terms. These three terms are matrix elements between two VCA states, an initial VCA state and a final perturbed state, and an initial perturbed state and a final VCA state. The first term is simple to evaluate, while the last two only have contributions for

perturbed states with wavevectors equal to those of the VCA states. Note that transitions between different $\bar{k}$ states in the Brillouin zone are allowed because the aperiodicity destroys the translational symmetry of the crystal and provides the required momentum through disorder scattering.

3.3 Phonon-Assisted Absorption Contribution

As stated previously, in order to account for the experimental results below the direct threshold it is necessary to add to the CPA contribution the added absorption due to phonon-assisted optical transitions. Hence, for this case it is the phonons which provide the necessary momentum for transitions between different $\bar{k}$ states. To evaluate this contribution, we use the model proposed by Dumpke et al.[83] In their model they only considered the low-temperature phonon emission case where the main contribution to the absorption occurs at the band edges of the initial and final states. Consequently, they assumed parabolic energy bands and their optical and electron-phonon matrix elements were independent of energy. These assumptions were used to model the two contributions to the absorption process. The first contribution involves the formation of a free indirect exciton for which they used the results of Elliott to give[88]

$$\alpha_{ex} = \left| \frac{B_{ex}}{\hbar\omega} \right| (\hbar\omega + E_{ex} - \hbar\omega_p - E^I) \tag{25}$$

where E_{ex} is the free exciton binding energy, E^I is the indirect energy gap, $\hbar\omega_p$ is the phonon emission energy, and B_{ex} is an adjustable parameter which contains density of states and matrix element information. The second contribution describes single-particle, indirect transitions between the heavy hole (hh), light hole (lh), and split-off hole (so) bands and the two lowest indirect conduction bands. It is given by

$$\alpha_{ind} = \sum_{i=1}^{3} \sum_{j=1}^{2} \left| \frac{m_{vi}}{m} \right|^{3/2} \frac{A_j^I}{\hbar\omega} \int_0^{\hbar\omega-\hbar\omega_p-E_j^I} \frac{(E_{vi})^{1/2}(\hbar\omega-\hbar\omega_p-E_j^I-E_{vi})^{1/2}\, dE_{vi}}{[\hbar\omega-(1+m_{vi}/m_c)E_{vi}-E_i^D]^2} \tag{26}$$

where i = 1-3 refers to the hh, lh, and so bands, respectively, j = 1-2 refers to the two

lowest indirect conduction bands, m_{vi} is the valence band effective mass, and m_c is the effective mass of the lowest direct conduction band. E_i^D is the smallest direct energy gap for the i^{th} valence band, E_j^I gives the two smallest indirect energy gaps, and A_j^I, in analogy to B_{ex} in Eq. (25), reflects the density of states and matrix element factors and is determined empirically. To evaluate Eqs. (25)-(26), experimental values[89] are used for the energy gaps and phonon energies, the effective masses are obtained from Table 1, and A_j^I and B_{ex} are given by Dumpke et al.[83] for AlAs. We assume that these empirical parameters are approximately constant for all compositions of $Al_xGa_{1-x}As$ since the density of states and optical and electron-phonon matrix elements are approximately equivalent for GaAs and AlAs.

3.4 Results and Discussions

Figure 4 shows the calculated absorption coefficient of $Al_{0.8}Ga_{0.2}As$. The solid line is obtained using the CPA model of Section 3.2 and the dashed line results from a VCA calculation, i.e., use $E_n^{(0)}(\vec{k},x)$ and $|n,\vec{k},x>$ to calculate $\alpha(\omega)$. The CPA curve has been shifted by $\sim$ -70 meV so that its direct energy gap, marked E^D in the figure, is in accordance with the experimental results of Monemar et al.[90] Furthermore, in order to compare more directly the overall shape of the theoretical and experimental curves, both theoretical curves have been scaled by a factor of 1.1 so that the CPA curve agrees with the experimental data for energies greater than the direct energy gap. The CPA curve is shifted by -70 meV because our CPA perturbation model cannot account entirely for the disorder-induced lowering of the direct energy gap. In contrast to Baldereschi et al.[75] who calculated a correction of +6 meV for $Al_{0.8}Ga_{0.2}As$ using the perturbation CPA model with a local pseudopotential, we obtained a value of -15 meV with a nonlocal pseudopotential. The disparity in the two results arises because the main contribution to the difference between the Ga and Al potentials comes from the cores of the atoms and only the nonlocal potential is able to take this effect into account. Our underestimation of the downward

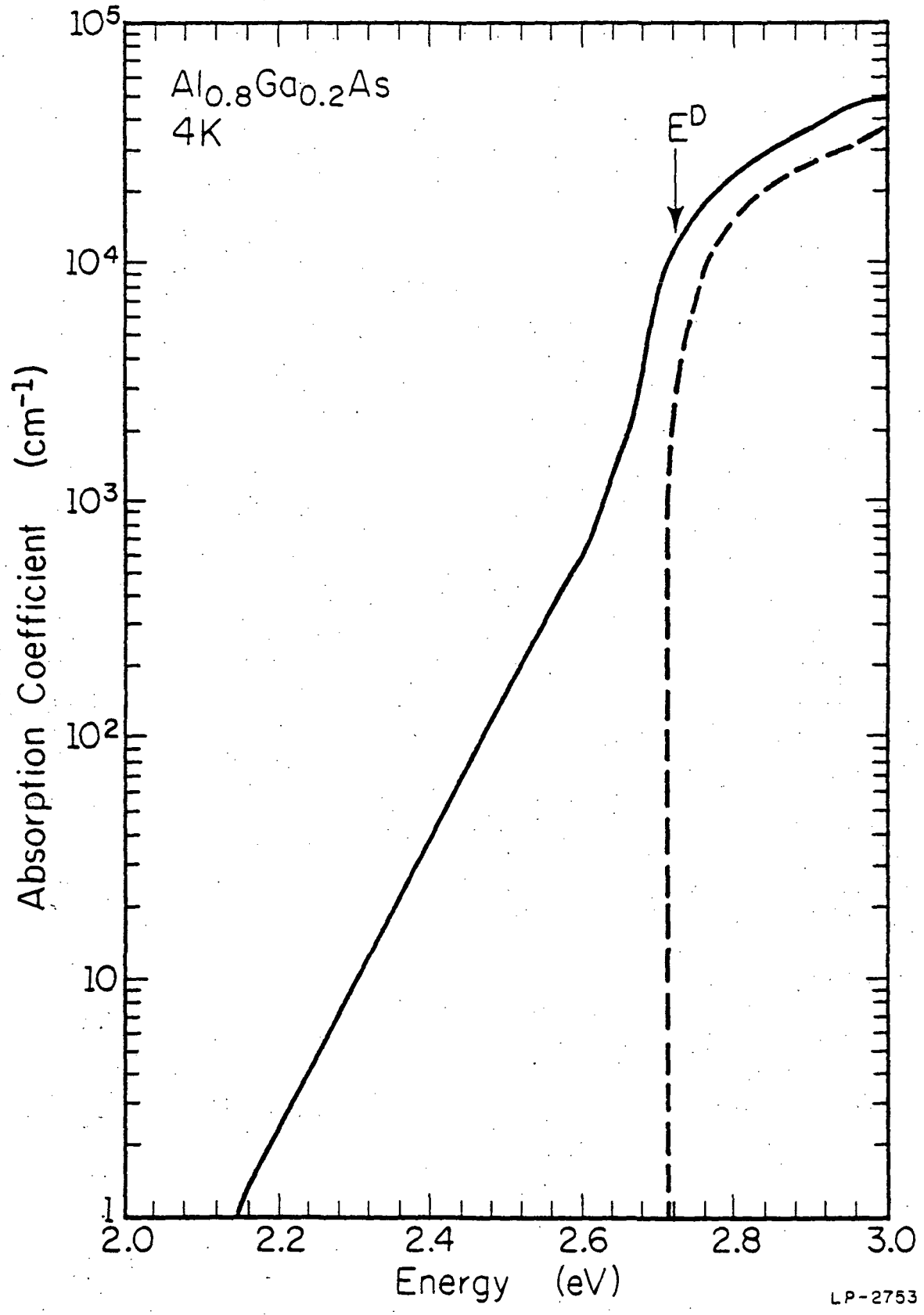

Figure 4. Comparison of the $Al_{0.8}Ga_{0.2}As$ absorption coefficient calculated by CPA, solid line, and VCA, dashed line.

bowing probably arises from two sources: the neglect of positional disorder and the approximate nature of second order perturbation theory. Baldereschi et al.[75] estimated that the effect of positional disorder of $Al_xGa_{1-x}As$ is small, while Chen and Sher[81] obtained an energy correction of $\sim$ -25 meV using a sophisticated CPA approach, which takes into consideration both positional and compositional disorders. Hence, the neglect of higher-order CPA effects is probably the largest source of error in our model. As a final note, because there is a large scatter in the experimental energy corrections as a function of composition,[75] it is difficult to judge the accuracy of the -84 meV value of Monemar et al.[90]

As discussed in the previous section, Figure 4 illustrates the phenomenon that the disorder potential allows indirect transitions to the X and L valleys, which accounts for the long absorption tail for the CPA curve. Because the density of states of the X point is approximately a factor of 3 larger than that for L,[91] the majority of indirect transitions occurs between the Γ and X regions. Figure 4 also shows that disorder effects start to become unimportant for energies larger than the direct gap and for these energies it becomes reasonable to model the absorption coefficient by a shifted (bowing effects) VCA curve.

In Figure 5 the absorption coefficient of $Al_{0.8}Ga_{0.2}As$ is calculated using the results of the phonon-assisted absorption model. The dashed curve neglects exciton processes, Eq. (25), while the solid curve includes these processes. Because the model only considers phonon-emission transitions, the dashed curve begins $\hbar\omega_p$ above the indirect energy gap, while the solid curve begins $\hbar\omega_p - E_{ex}$ above the indirect gap since this curve also includes the exciton contribution. For larger energies the two curves merge, since the exciton contribution has a weak dependence on the photon energy. Since Eq. (26) shows that $\alpha_{ind}(\omega)$ blows up as $\hbar\omega \rightarrow E^D$, the curves are only plotted up to $\hbar\omega$ = 2.7 eV. The discontinuity in Eq. (26) occurs because the expression for $\alpha_{ind}(\omega)$ is derived using second order pertubation theory which becomes invalid as $\hbar\omega \rightarrow E^D$, i.e., it is necessary to include self-energy effects in the derivation. Finally, the most important point to gather from this

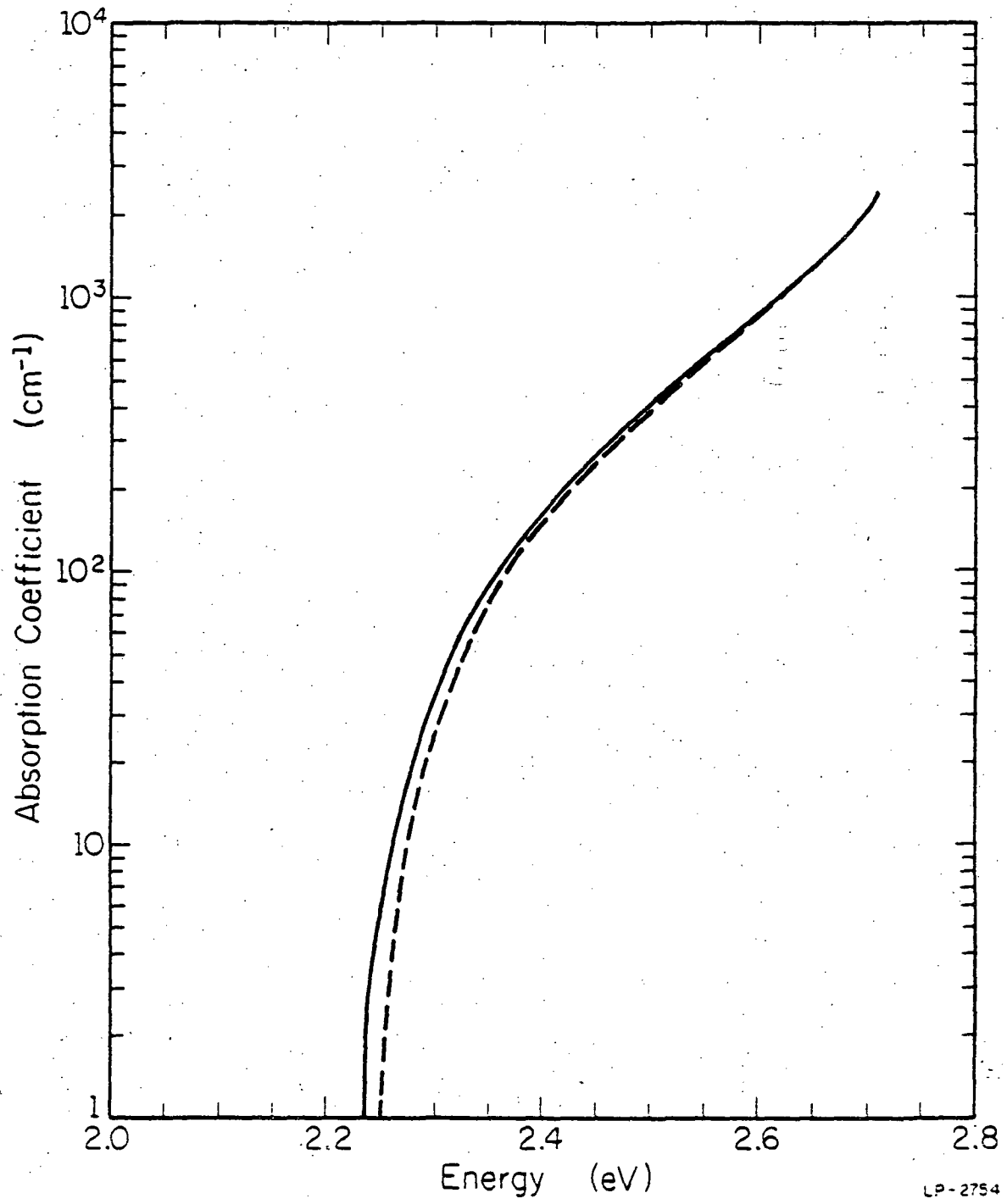

Figure 5. The contributions of phonon-assisted absorption to the absorption coefficient of $Al_{0.8}Ga_{0.2}As$. The solid line includes both exciton-phonon and phonon-assisted transitions, while the dashed line only includes phonon processes.

figure is that by comparing it with Figure 4, it is evident that in $Al_{0.8}Ga_{0.2}As$ phonon-assisted and disorder-assisted indirect transitions have approximately the same magnitude.

Figure 6 compares the total calculated absorption coefficient of two compositions of $Al_xGa_{1-x}As$ with the experimental results of Monemar et al.[90] The calculated curves include both the CPA and phonon-assisted contributions. In the figure the solid and dashed lines are the theoretical and experimental values for $Al_{0.8}Ga_{0.2}As$ at 4 K, respectively, and the dotted-dashed and dotted lines are the theoretical and experimental values for $Al_{0.3}Ga_{0.7}As$ at 300K, respectively. The experimental data are available only for the energy range presented in the figure. Since $Al_{0.3}Ga_{0.7}As$ is a direct material, the theoretical curve does not include the phonon-assisted contribution and disorder effects are barely noticeable. As in Figure 4, the CPA contributions to the theoretical curves have been shifted and scaled so as to enable direct comparisons with the experimental data. The factors for x = 0.8 are the same as those given for Figure 4 and the shift and scale for x = 0.3 are +20 meV and 1.0 (no scaling), respectively. The energy shift is positive since Monemar et al.[90] obtained no disorder-induced lowering of E^D, while we calculated a value of -20 meV. As discussed above, because of the large scatter in experimental bowing values, it is difficult to ascertain the validity of the experimental value. Consequently, for comparison, Chen and Sher[81] calculated an energy lowering for $Al_{0.3}Ga_{0.7}As$ of $\sim$ -35 meV.

Figure 6 shows that our theoretical results compare very favorably with the experimental data. The only noticeable discrepancy between the calculated and experimental curves occurs for energies around the direct gap where our neglect of direct, free excitons becomes important. Note that these exciton effects not only raise the magnitude of the direct contribution, but also change the shape of the curve around E^D. In Chapter 5 we will discuss a method for extending our model to include these Γ region exciton effects.

In conclusion, we have extended the partition method, based on a hybrid band structure approach, to include disorder- and phonon-assisted indirect transitions in ternary

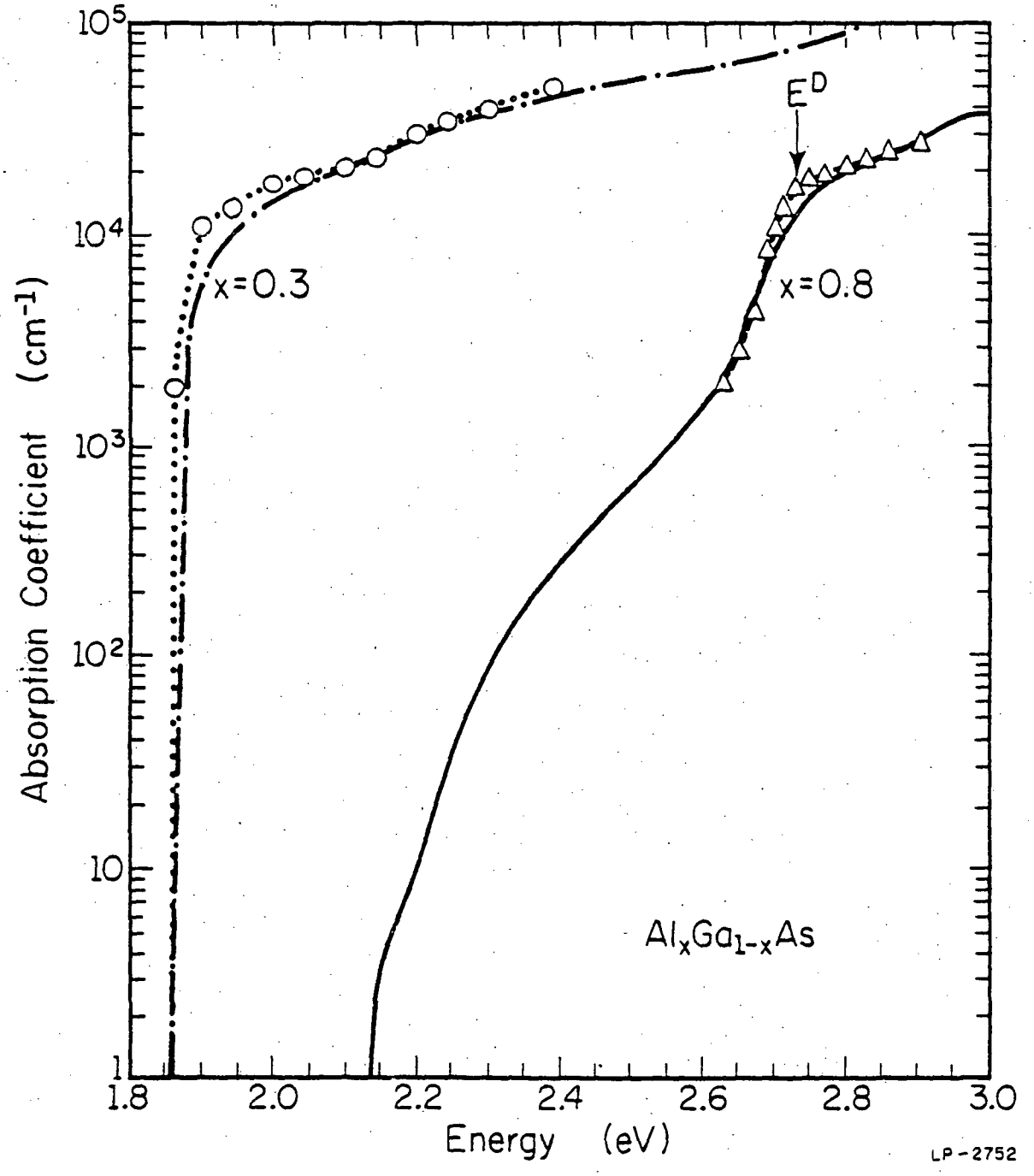

Figure 6. The absorption coefficient for two $Al_xGa_{1-x}As$ compositions. The dotted-dashed and dotted lines are the calculated and experimental values for x = 0.3, respectively, and the solid and dashed lines are the calculated and experimental values for x = 0.8, respectively. The calculated curves include the CPA and phonon-assisted contributions.

alloys. The disorder of the alloy has been accounted for by using a perturbative CPA approach and the phonon contribution is incorporated using the empirical model of Dumpke et al.[83] In $Al_xGa_{1-x}As$ the contributions of disorder-assisted and phonon-assisted indirect transitions are determined to be comparable. The results for the disorder-induced, Γ point, energy-gap bowings are shown to be nearly comparable to those calculated using a more sophisticated CPA approach. Because of the large scatter in the reported experimental Γ energy gaps, it is difficult to compare the calculated values with experiment. In general the calculated absorption coefficients of $Al_xGa_{1-x}As$ are in good agreement with the experimental data and compare well with the calculated values of Ting and Chang.[82] Because our method is based on a perturbation expansion, our model does not provide correct absolute absorption values, but determines the correct relative contributions of the indirect (disorder- and phonon-assisted) and direct transitions. Even though results are only presented for $Al_xGa_{1-x}As$, our model can also provide good results for other III-V ternary alloys. In the next two chapters the partition method is applied to heterostructure materials.

4. DIELECTRIC CONSTANT AND REFRACTIVE INDEX OF III-V BASED MQWs AND SUPERLATTICES

4.1 Introduction

Recently, there has emerged a number of laser[9,92] and optoelectronic[31-34] devices which would benefit from a knowledge of the refractive index of MQWs and superlattices. Equation (17) shows that $\eta(\omega)$ depends on both the real and imaginary parts of the transverse dielectric constant. Because we are mainly interested in low-frequency applications, $\epsilon_2(\omega) << \epsilon_1(\omega)$, Eq. (17) reduces to

$$\eta(\omega) = \sqrt{\epsilon_1(\omega)} \quad . \tag{27}$$

In contrast to the absorption coefficient which selects out specific portions of the Brillouin zone, the refractive index includes transitions from all regions of the zone. Consequently, a useful one-electron superlattice band structure model must be accurate throughout the zone, be efficient, and be extendible to include many body effects such as excitons, band tailing, and alloy disorder.

There exists in the literature a number of superlattice band structure models which can be used to calculate the low-frequency absorption coefficient.[18,20,25,27-28] As stated in Chapter 1, the majority of these models are inaccurate at the zone edges[18,25] or are computationally complex.[20,27] In the past few years, a number of band structure models based on the $\vec{k} \cdot \vec{p}$ method[38] have been introduced which do not suffer from the above problems.[23,28,93-94] In this chapter the superlattice $\vec{k} \cdot \vec{p}$ approach suggested originally by Leburton and Hess[23] and extended by Kahen and Leburton[28] is developed and applied to GaAs-$Al_xGa_{1-x}As$ MQWs and superlattices.

In Section 4.2 a review of the different superlattice $\vec{k} \cdot \vec{p}$ approaches is made and the merits of the different models are discussed. We give an account of our superlattice model, based on the partition method, in Section 4.3. Results are presented in Section 4.4 for the structure and frequency-dependent refractive index of GaAs-AlAs superlattices. Because it

is necessary to include excitons in the superlattice model in order to have a reasonable representation of $\alpha(\omega)$, we have postponed an account of the absorption coefficient until the next chapter where excitons are introduced into the model.

4.2 Superlattice $\vec{k} \cdot \vec{p}$ Band Structure Models

As discussed in Section 2.2.a. using the $\vec{k} \cdot \vec{p}$ approach[38] the entire band structure can be obtained by expanding about one or several symmetry points. The advantages of using several expansion points are that fewer and less complex basis sets can be employed to perform the expansions. Leburton and Hess[23] calculated the dielectric constant of long period GaAs-AlAs superlattices by splitting the constituent material Brillouin zones into the Γ, X, and L regions. For the Γ region, a simplistic $\vec{k} \cdot \vec{p}$ expansion was used and superstructure effects were accounted for within a tight binding approach based on the envelope-function approximation.[21,95] The Kronig-Penney model[95] was used to calculate the superlattice, miniband, energy positions and widths. A crude VCA approximation was made for the contributions of the X and L regions. The results of Leburton and Hess[23] were correct qualitatively in that the resulting superlattice dielectric constant was structure dependent, showed a polarization effect, and exhibited fine structure due to the quantized Γ region contribution.

Tsu and Iorriatti[93] calculated the longitudinal dielectric constant of GaAs-$Al_xGa_{1-x}As$ MQWs also by splitting the Brillouin zone into the Γ, X, and L regions. They improved the model of Leburton and Hess[23] by considering quantization effects at the Γ, X, and L points only for energies below the superstructure potential barriers at each of the symmetry points. These energies were calculated by performing simplistic $\vec{k} \cdot \vec{p}$ expansions about each of the symmetry points, i.e., effective-mass expressions, while a crude VCA approach was used for energies above the potential barriers. Since their model is a simplistic version of the one discussed in this chapter, it is pointless to discuss the merits of their model.

Mailhiot et al.[94] calculated the electronic band structure of a GaAs-AlAs superlattice within the envelope-function approximation.[21] The energies and the propagating and evanescent envelope wavefunctions of the constituent superlattice materials were obtained by performing $\vec{k} \cdot \vec{p}$ expansions about the respective Γ symmetry points. The Γ-point basis sets were determined using the results of local pseudopotential calculations. Similar to our $\vec{k} \cdot \vec{p}$ approach, their technique avoids the problems inherent in the pure tight binding and pseudopotential methods. However, since their model neglects nonlocal, as well as spin orbit interactions, the bulk band structures obtained by their model are inferior to those obtained using our hybrid band structure approach. It should also be noted that these effects cannot be included in their approach, since a nonlocal band structure cannot be obtained by performing a $\vec{k} \cdot \vec{p}$ expansion about a single symmetry point.[96] Consequently, the accuracy of their technique is limited to a small region of the zone and, thus, can only be used to determine accurately, for example, the Γ region absorption coefficient.[97] In order to improve their model, it is necessary to resort to our method of expanding about several symmetry points.

4.3 Electronic Band Structure Model of [100] Superlattices

4.3.a Envelope-Function Approximation

In long period superlattices, the periodic variation of the band gap produces quantization of the electronic states which results in the formation of minibands which are superimposed upon the bulk band structure of the constituent materials. We account for this band modulation, assumed to be in the z-direction, by quantizing the z-component of the wavevector $\vec{k}$ which results in a tight binding superlattice wavefunction of the form.[95]

$$\Psi_{\vec{k}} = e^{i\vec{k}_{||} \cdot \vec{r}_{||}} \Phi^{j}_{K_z}(z) \, | u_{\vec{k}} > \tag{28}$$

where K_z is the superlattice traveling wavevector in the z-direction, $\vec{r}_{||}$ and $\vec{k}_{||}$ are the position coordinate and wavevector in the plane parallel to the superlattice layers, $|u_{\vec{k}}>$ is

the periodic part of the bulk Bloch state, and $\Phi^j_{K_z}(z)$ is the superlattice envelope wavefunction of the j^{th} quantized state whose periodic part is found from the solution of the periodic square-well potential problem, as described in Section 4.3.b. Equation (28) is derived by assuming that there is no mixing between valence-band, envelope wavefunctions[24-25] (see Section 4.3.c) and the superlattice periodicity acts only upon the envelope wavefunction in the z-direction. Therefore, $u_{\vec{k}}(r)$ is unchanged from its bulk value, as given in Section 2.2, and the superlattice band structure differs from the corresponding bulk material band structure only in the quantization direction.

In line with the above approximations, we assume the following simplified, tight-binding expression for the energy dispersion relation of the minibands in the z-direction[95]

$$E_j(K_z) = E_j + (-1)^j W_j \cos(K_z d) \tag{29}$$

where E_j and W_j are the midband energy and energy width of the j^{th} miniband, respectively, and d is the period of the superlattice. The superlattice miniband energy disperson relation $E^j_{SL}(k_x,k_y,K_z)$ is calculated by adding Eq. (29) onto the bulk relation $E_B(k_x,k_y,k_z)$ and quantizing the k_z-wavevector. We obtained the superlattice optical matrix element M_{SL} between the valence and conduction bands by quantizing the z-component of the $\vec{k}$ vector in the bulk matrix element expression M_B, which is discussed in Section 2.3. Hence,

$$E_B(k_x,k_y,k_z) \rightarrow E^j_{SL}(k_x,k_y,K_z) = E_B(k_x,k_y,k_j) + \Delta E_j + (-1)^j W_j \cos(K_z d) \tag{30a}$$

$$M_B(k_x,k_y,k_z) \rightarrow M_{SL}(k_x,k_y,k_j). \tag{30b}$$

Here ΔE_j is the shift in the energy of the j^{th} level resulting from the carrier confinement. The values of W_j and ΔE_j are determined using the interface connection rules described below and $k_j = [2(j-1) + 1]\pi/2d$. By applying Eqs. (30) at the three symmetry points, Γ, X, and L, we obtained the quantized electronic band structure presented in Figure 7. Since K and W are low symmetry points, the effects of quantization are negligible for the

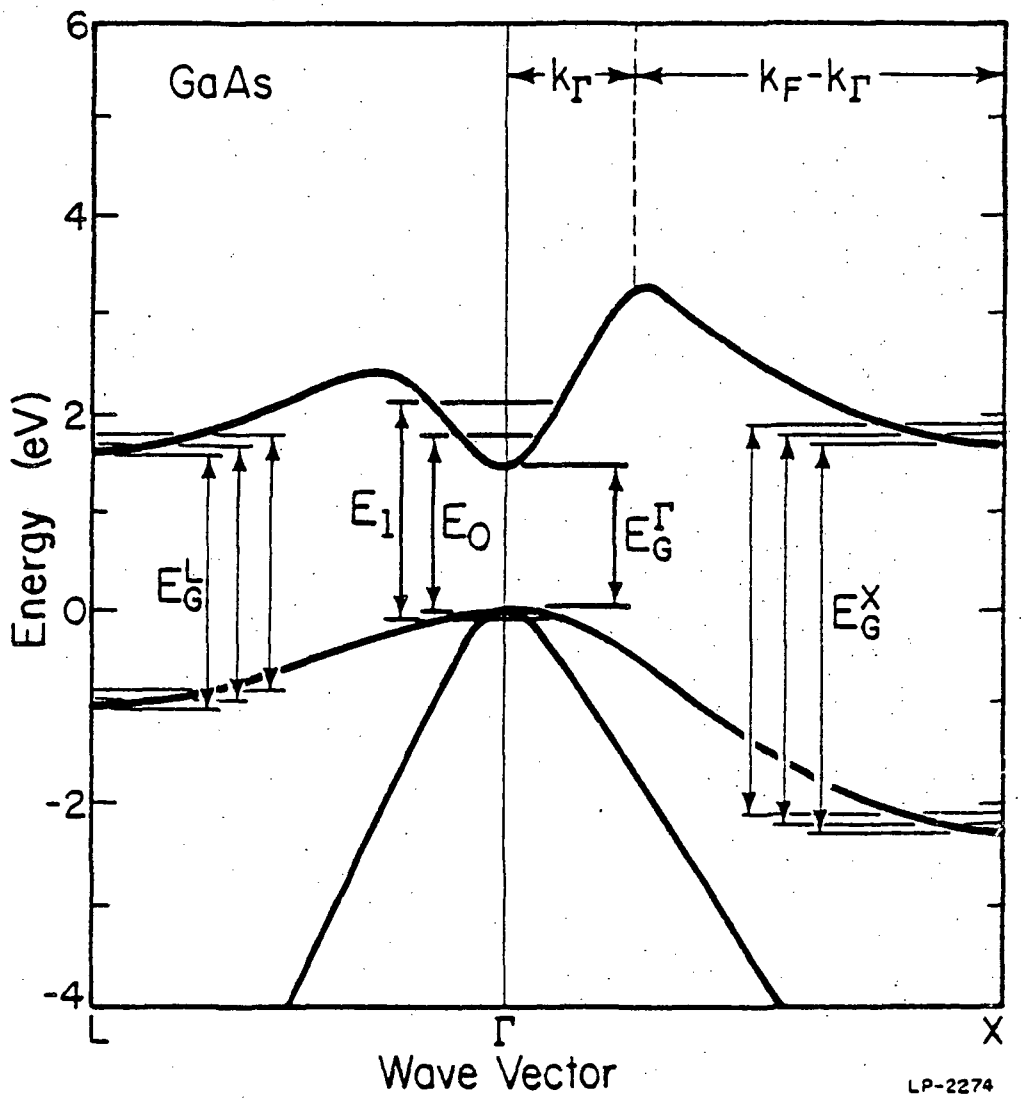

Figure 7. Band structure of GaAs and the effect of quantization on each of the symmetry points.

contributions coming from these regions. Therefore, these contributions are treated in a mean-field approximation where the energy and matrix element dispersion relations are approximately equal to the compositionally averaged bulk alloy values. These alloy values are calculated using the VCA model presented in Section 3.2.

Superstructure effects also influence the evaluation of the $|\hat{e} \cdot P_{cv}|^2$ term in Eqs. (14)-(15), which give the expressions for $\epsilon_1(\omega)$ and $\epsilon_2(\omega)$, respectively. The $\hat{e}$ factor takes into account the consideration that it is necessary to average over all polarizations of the optical excitation. For bulk materials, on account of their isotropy, all polarizations are equivalent and this term is equal to

$$|\hat{e} \cdot P_{cv}|^2 = \frac{1}{3}(p_x^2 + p_y^2 + p_z^2) \tag{31}$$

where p_x is the x-component of $\vec{P}_{nn'}$, defined in Eq. (2). However, for superlattice structures the symmetry is lowered by the superstructure layering which causes one direction, i.e., the z-direction, to become preferred over the other two. This asymmetry leads to two distinct polarization terms which can be combined into one expression

$$|\hat{e} \cdot P_{cv}|^2 = \frac{1}{2}(1 - \mathrm{POL})(p_x^2 + p_y^2) + (\mathrm{POL})p_z^2 \tag{32}$$

where POL is one or zero for the electric field polarization being perpendicular (TM) or parallel (TE) to the superlattice layers, respectively.

In this chapter, we assumed a superlattice model for which superstructure effects are assumed to be operative at Γ, X, and L for all particle energies. Hence, we use Eqs. (30) and (32) for all energies. In the next chapter we find that a better approximation is to use an approach which combines both superlattice (Eqs. (30) and (32)) and isotropic-alloy (VCA model and Eq. (31)) electronic band structure models.

4.3.b Interface Connection Rules

At each symmetry point the envelope wavefunction $\Phi^j_{K_z}(z)$ and the miniband parameters, W_j and E_j, are obtained through the use of connection rules which account for the difference in electronic properties of the two constituent superlattice materials. In general, these connection rules involve continuity conditions for the wavefunctions of the two materials at the boundaries between them.[21,22,24] In our approach, we assumed the continuity of the entire wavefunction and its derivative at the interfaces; however, since the GaAs-$Al_xGa_{1-x}As$ junction is not abrupt, we averaged these relations over the volume of a unit cell to obtain

$$<X_A \mid \Psi_A> = <X_B \mid \Psi_B> \tag{33a}$$

$$<X_A \mid \frac{d}{dz} \mid \Psi_A> = <X_B \mid \frac{d}{dz} \mid \Psi_B> \tag{33b}$$

where for each material A and B, $|\Psi>$ is the total wavefunction, and $|X>$ is the local wavefunction. If B is the barrier material on the right-hand side of the heterojunction, the two A material wavefunctions can be written as

$$|\Psi_A> = e^{ik_x x + ik_y y} \left[C_A^+ e^{ik_z z} \mid u^A_{\vec{k}} > + C_A^- e^{-ik_z z} \mid u^A_{-\vec{k}} > \right] \tag{34a}$$

$$|X_A> = \frac{1}{\sqrt{2}} (\mid u^A_{\vec{k}} > + \mid u^A_{-\vec{k}} >) \tag{34b}$$

where $|u^A_{-\vec{k}}>$ is the time reversed state[63] of $|u^A_{\vec{k}}>$, and C_A^+ and C_A^- are the amplitudes for the forward and backward propagating waves, respectively. The transmitted wavefunctions in material B are

$$|\Psi_B> = e^{ik_x x + ik_y y} C_B e^{ik_z' z} \mid u^B_{\vec{k}} > \tag{35a}$$

$$|X_B> = \mid u^B_{\vec{k}} > \tag{35b}$$

where k_z' has an imaginary component if the energy of the particle is smaller than the

potential barrier height. Note that in agreement with the assumptions underlying the derivation of Eqs. (28)-(29), Eqs. (33)-(35) also do not include the effects of mixing between quantized bands having comparable energies.

By using the orthogonality conditions between time reversed states, $\langle u_{\vec{k}} | u_{-\vec{k}} \rangle = 0$ and $\langle u_{\vec{k}} | \frac{d}{dz} | u_{-\vec{k}} \rangle = 0$, and the expressions for $| u_{\vec{k}} \rangle$ in each material (see Section 2.2) in Eq. (33), it is easy to obtain the following conditions on the envelope functions F_A and F_B at the position of the interface at $z = z_o$

$$F_A(z = z_o) = F_B(z = z_o) \tag{36a}$$

$$\frac{1}{m_A(E)} \frac{dF_A}{dz}\Big|_{z=z_o} = \frac{1}{m_B(E)} \frac{dF_B}{dz}\Big|_{z=z_o} \tag{36b}$$

where

$$\frac{1}{m(E)} = \frac{1}{m_o} \left| 1 + \frac{\langle u_{\vec{k}} | \frac{d}{dz} | u_{\vec{k}} \rangle}{ik_z(E)} \right| \tag{37}$$

and we have indicated explicitly that k_z in Eqs. (34)-(35) is energy dependent. To derive the above we set $k_x = k_y = 0$ (since we ignore band mixing) and defined F_A and F_B by

$$F_A(z) = \frac{1}{\sqrt{2}} \left(C_A^+ e^{ik_z z} + C_A^- e^{-ik_z z} \right) \tag{38a}$$

$$F_B(z) = C_B e^{ik_z' z} \tag{38b}$$

Equation (36) gives the normal connection rules within the envelope-function approximation.[21,98] except that the masses are energy dependent in both materials to account for the effects of non-parabolicity. Because the non-parabolicity effects at the X and L points are weak in comparison to those at Γ, for the X and L region minibands, we used the band-edge limit of Eq. (37), i.e., the effective mass value, for all energies (see Table 1).

By applying the energy-dependent connection rules to a periodic superstructure, we

obtained the following relation, which is analogous to that of Bastard[21] and Sai-Halasz et al.,[98] except that now the masses are energy dependent

$$\cos K_z d = \cos k_z^A L_z \cos k_z^B L_B - Q \sin k_z^A L_Z \sin k_z^B L_B \tag{39a}$$

$$Q = \frac{1}{2}\left[\frac{k_z^A m_B(E)}{k_z^B m_A(E)} + \frac{k_z^B m_A(E)}{k_z^A m_B(E)}\right] \tag{39b}$$

Here L_Z and L_B are the well and barrier widths of materials A and B, respectively, $d = L_Z + L_B$, and k_z^A and k_z^B are the energy-dependent wavevectors of Eq. (37). In order to evaluate Eq. (39) it is necessary to determine the energy-band offsets at the Γ, X, and L symmetry points. Figure 8 gives these offsets for a GaAs-AlAs interface at 300 K assuming a 65:35, Γ-point, band-discontinuity ratio.[42] The energy levels in Figure 8 are obtained using experimental data, when available; otherwise, they are estimated from nonlocal pseudopotential calculations which include spin orbit effects.

Equation (39) yields values for E_j and W_j of Eq. (29). By solving the periodic potential problem used to obtain Eq. (39), we also obtained an expression for the periodic part of $\Phi_{K_z}^j(z)$

$$g(z) = \begin{cases} (c')\cos(k_z^A(E)z) & |z| < L_Z/2 \\ \exp(-K_z^B(E)z) & L_Z/2 < |z| < L_Z/2 + L_B/2 \end{cases} \tag{40a-b}$$

where Eq. (40a) is valid in material A (the well) and Eq. (40b) is valid in material B (the barrier). In the above we assume $z = 0$ is at the middle of the well and c', a normalization coefficient, and K_z^B, a complex wavevector, are both determined using the continuity of $g(z)$ and its derivative at $z = L_Z/2$.

4.3.c Valence-Band Mixing Effects

Recently, there has been a flurry of activity concerned with valence-band mixing effects which produce, in the direction parallel to the superlattice layers, symmetry exchanges and repulsion effects between the bands.[24-25] These authors[24-25] show that

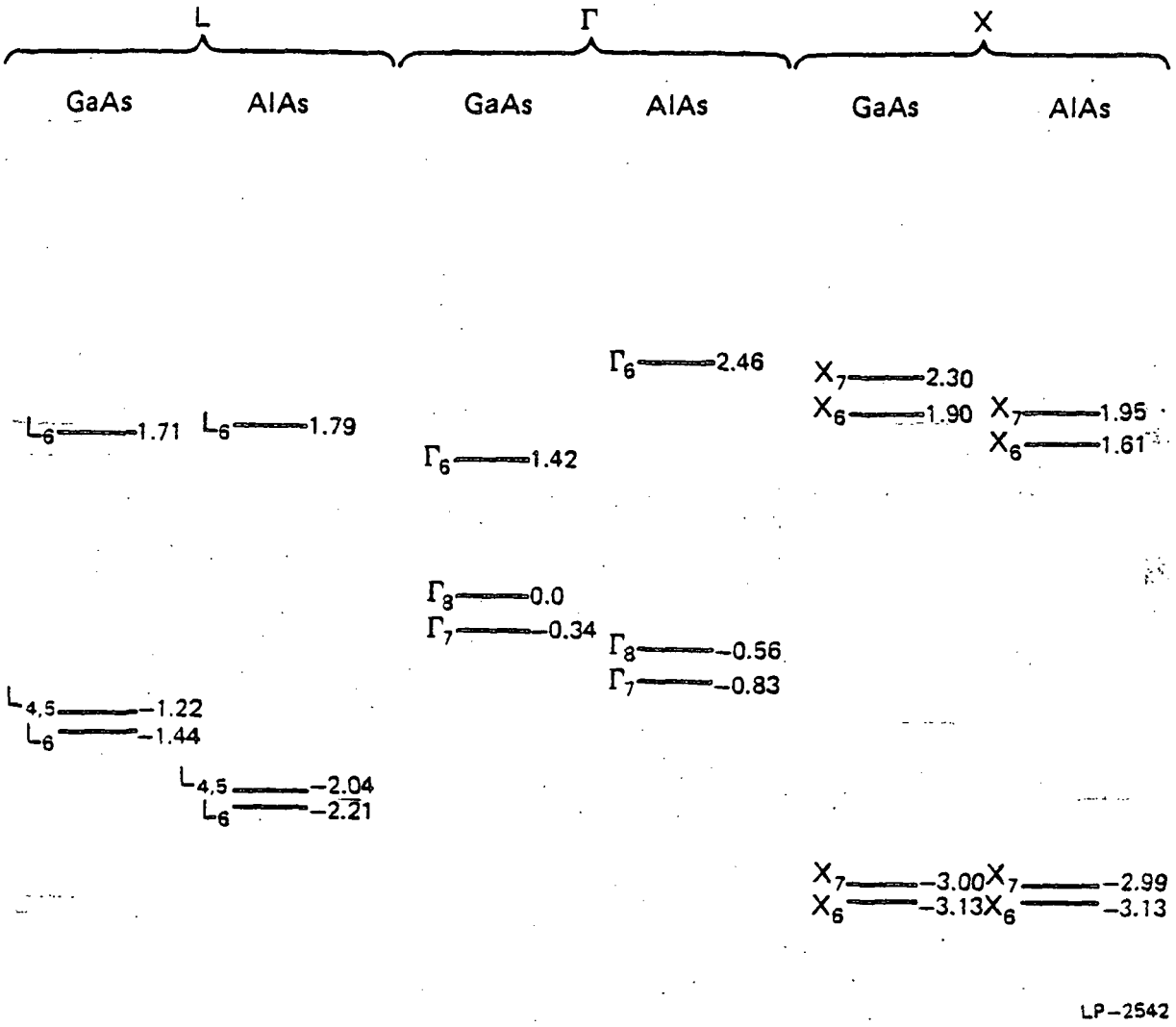

Figure 8. Energy-band offsets at 300 K at each of the main symmetry points for a GaAs-AlAs superlattice. The energy levels are calculated assuming a 65:35 Γ-point. band-discontinuity ratio. Each level is marked with the appropriate double-group-symmetry notation.

mixing effects in GaAs-$Al_xGa_{1-x}As$ superlattices between the *l*h and hh quantized, energy bands become important when the energy separation between the bands are on the order of 10 meV. In this chapter Eqs. (28)-(30) and (33)-(37) are derived by neglecting these effects. Therefore, for some structures these equations are valid, while for others the model must be modified. In the next chapter we show that these equations can be retained if we modify the masses of the hh and *l*h bands so as to account empirically for the position of the bound exciton peaks. Using the variational, band-mixing model of Altarelli,[24] it is straightforward to include these effects in our model in a more rigorous fashion.

4.4 Results and Discussions

Figure 9 gives the contributions of the Γ, X and L regions to the real part of the dielectric constant of a GaAs-AlAs superlattice at $\hbar\omega$ = 1.5 eV for light being polarized parallel and perpendicular to the superlattice layers (solid and dashed lines, respectively). Values are presented as a function of the period $d=L_B+L_Z$ for a mole fraction $x=L_B/(L_Z+L_B)$ of AlAs of 0.3. The superlattice quantization axis is in the [100] direction. Notice the large L contribution with respect to the Γ and X contributions. As already mentioned in Section 2.4, this results from the combined effects of large densities of states and momentum matrix elements, and small energy gaps present in the L region. The L contribution is approximately independent of the period because the superlattice quantization axis is not aligned with any of the principal axes and, thus, it is approximately equal to its bulk alloy value. Hence, in agreement with the experimental findings of Laidig et al.,[99] the effect of the superstructure is only weakly felt at L. The L contribution is isotropic since the x, y, and z directions are all equivalent for the [111] direction. Therefore, for a superlattice grown along the [100] direction, the polarization of the L valleys, as an average over the three orthogonal directions, vanishes in analogy to the bulk case.

The Γ and X contributions both increase as a function of the period. The superlattice

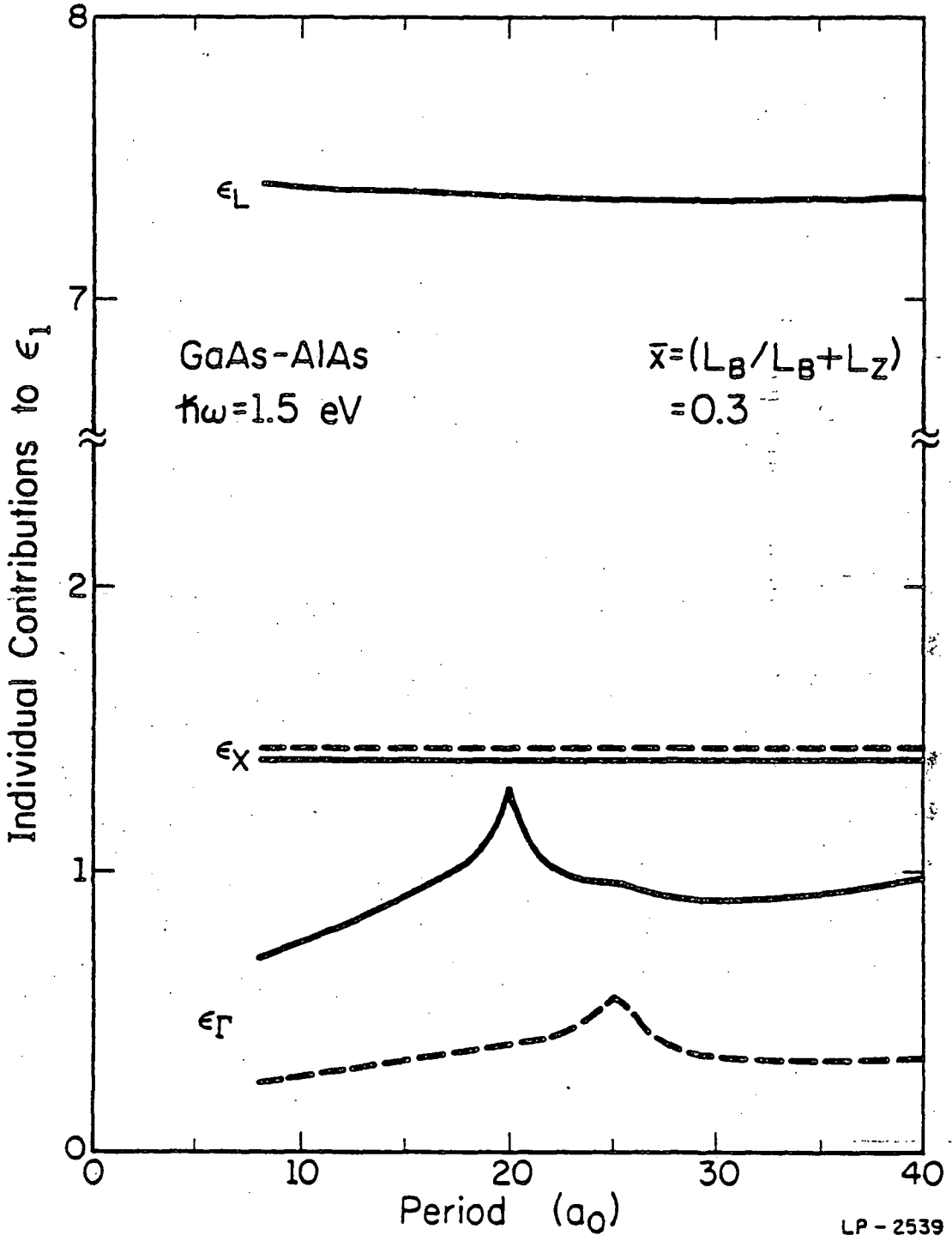

Figure 9. Structure dependence of the Γ, X, and L region contributions to the real part of the dielectric constant of a GaAs-AlAs superlattice at $\hbar\omega$ = 1.5 eV. The mole fraction of AlAs in the structure is $\bar{x}$ = 0.3 and a_0 is the lattice constant. The solid and dashed lines are for parallel and perpendicular polarizations, respectively. Note that the L region contribution is isotropic.

structure influences the dielectric constant by determining both the position and miniband width of the lowest quantized energy levels. Each are inverse functions of L_B and L_Z. It can be easily determined that the miniband widths have a negligible effect on the dielectric constant. Therefore, the important factor is the lowering of the quantized levels which results in an increase in ϵ_1 with the period. The peaks on the parallel Γ polarization curve correspond to the first electron-heavy hole and electron-light hole transitions, E_1(e-hh) and E_1(e-lh), respectively. For perpendicular polarization only E_1(e-lh) is present since the symmetry of the heavy hole state precludes momentum matrix elements in the quantization direction, i.e., for the heavy hole band, $p_x^2 \approx p_y^2$ and $p_z^2 = 0$ and use Eq. (32). Polarization effects at Γ occur because the heavy hole transitions which are responsible for the strong coupling between the Γ conduction and valence bands are absent for perpendicular polarization.

The X contribution is a weak function of the period because only the conduction band is quantized (we ignored the very small offset between the two valence bands as shown in Fig. 8); and, in comparison with the Γ point conduction band mass, both the transverse and longitudinal conduction band masses are large and, thus, rather insensitive to the confinement. Hence, in analogy with the L contribution, the X region dielectric constant assumes approximately its bulk alloy value. For the X region the band-edge, optical matrix elements are also appreciable only for light polarized along the x and y directions, i.e., similar to the situation for the e-hh transition. However, two of the valleys have the superlattice quantization axis parallel to the z-component of the optical matrix elements while the other four valleys have the quantization axis aligned along the y-component of the matrix elements. Hence, perpendicular polarization (the quantization axis is perpendicular to the layers) is favored by four of the six X valleys, which accounts for the reverse polarization trend for the X valley contribution.

In Figure 10 we compared our results for the normalized index of refraction of a GaAs-AlAs superlattice with the experimental data of Suzuki and Okamoto.[100] Our results

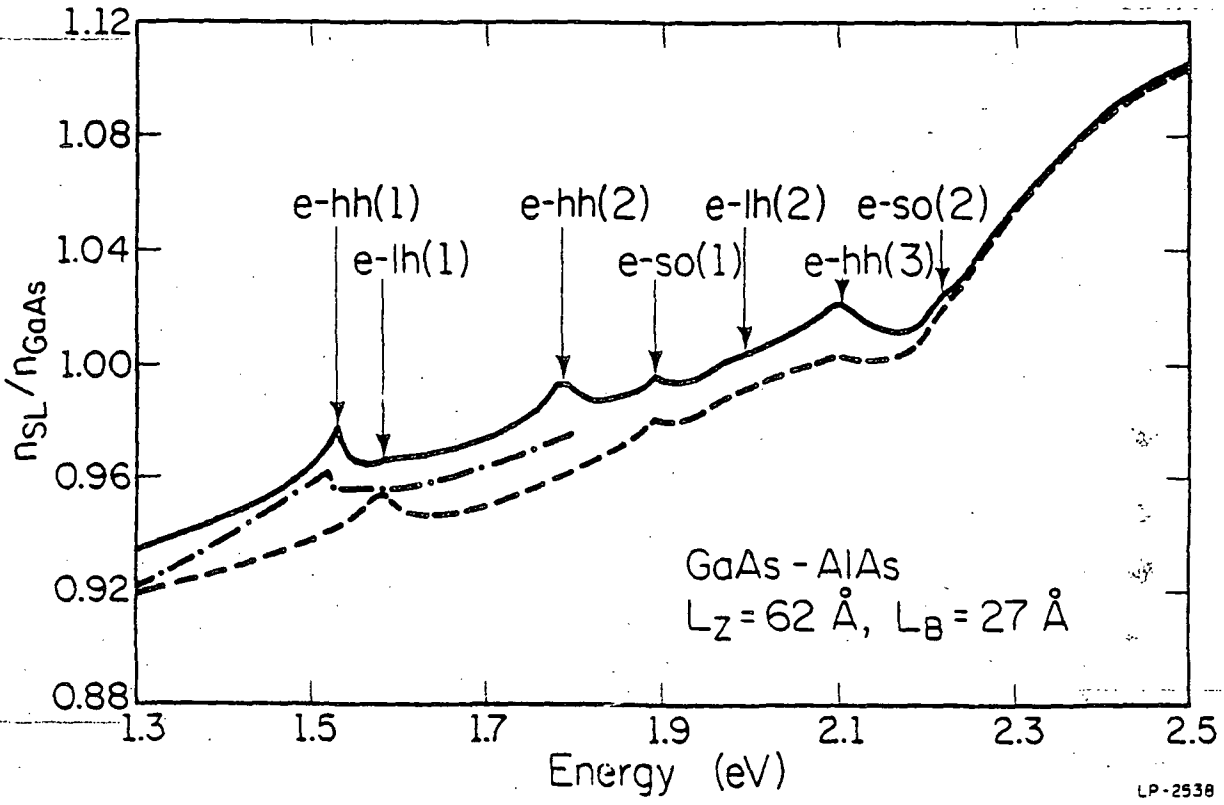

Figure 10. Normalized index of refraction of a GaAs-AlAs superlattice as a function of energy. The solid and dot-dashed lines are the theoretical and experimental parallel polarization values, respectively, and the dashed curve gives the theoretical perpendicular polarization values. The arrows mark the positions of the quantized Γ valley transitions. e-hh(j) corresponds to a transition between the j^{th} level of the heavy hole band and the j^{th} level of the lowest conduction band.

are for parallel and perpendicular polarizations, solid and dashed lines, respectively, while the experimental data are for parallel polarization, dotted-dashed line. The superlattice has a well and barrier thickness of 62 and 27 Å, respectively, and, consequently, $x = 0.3$. The experimental data are only available up to $\hbar\omega = 1.8$ eV. Because we have neglected band transitions larger than 6 eV in our model, the results for the bulk GaAs index of refraction are $\approx$ 7% smaller than the experimental values.[87] For most optical transitions the influence of the higher bands can be described by a constant factor. Therefore, we used a normalization procedure which enabled us to remove this constant contribution and focus only on the band-edge transitions. Consequently, in order to compare directly our results with the experimental data, the theoretical and experimental $\eta(\omega)$ values given in Figures 10 and 11 are normalized with respect to the theoretical and experimental bulk GaAs index of refraction values at $\hbar\omega = 1.5$ eV, respectively. In the figure the arrows indicate the quantized, Γ-point, valence band-conduction band transitions which produce the fine structure on the theoretical parallel polarization curve. The peaks on the theoretical perpendicular polarization curve are the result of the corresponding light hole and split-off hole transitions indicated on the parallel polarization curve. As discussed previously, there are no heavy hole transitions for perpendicular polarization and the dielectric constant is larger for parallel polarization. However, notice that the anisotropy vanishes around 2.3 eV due to the falling off of the Γ contribution and the isotropy of the L contribution.

As can be seen from the figure, our results compare favorably with the experimental data, there being less than a 2% discrepancy between the two parallel polarization curves. Our E_1(e-hh) peak is shifted to higher energies by $\approx$ 8 meV and is slightly larger. The slight shift is probably the result of our neglect of exciton effects in this model. Both the E_1(e-lh) and E_2(e-hh) peaks are absent from the experimental data. The light hole transitions are barely noticeable on our parallel polarization curve, being weak and overshadowed by the neighboring e-hh transitions; consequently, they might be difficult to observe experimentally. We do not know why the E_2(e-hh) peak is absent from

the experimental data. However, in general the data verify the validity of our superlattice model.

In Figure 11 we show the normalized index of refraction at 1.5 eV for a range of GaAs-AlAs superlattices. Again, the solid and dashed lines are for light being polarized parallel and perpendicular to the superlattice layers, respectively. Also shown in the figure are the normalized experimental alloy values[87] corresponding to four of the five superlattice compositions (there are no data for $x = 0.6$). As in Figure 10, the main peaks on the curves correspond to the quantized, Γ-region transitions. All of the parallel polarization curves exhibit the E_1(e-hh) peak while the $x = 0.1$ and 0.2 curves also show the E_2(e-hh) peak. Again, for perpendicular polarization, the peaks are due to the E_1(e-lh) transition. The E_1(e-lh) transition also contributes to the parallel curves; however, it is barely noticeable, being overshadowed by the neighboring E_1(e-hh) peak as in the previous figure. For both polarizations the peaks become larger and narrower up to $x = 0.3$, after which they become smaller. These effects can be explained by the following mechanisms. For small x values the peaks are broad because a large change in the period is required to modify the superlattice characteristics which resemble those of bulk GaAs. Additionally, the effects of quantization are weakly felt for these structures, which results in shallower peaks. For larger x values, the superlattice properties are a stronger function of the period, which produces sharper peaks; however, with increasing AlAs content, the peaks become shallower because the AlAs Γ region contribution is approximately a factor of seven times smaller than that of GaAs (see Table 2).

A characteristic feature of all of the curves is the shift in the peak positions for increasing AlAs content. For any mole fraction x, the energy of an optical transition increases as a function of the barrier width, but decreases more rapidly with the well width; consequently, the transition energies are the largest for small-period superlattices because of the strong confinement. Therefore, as the period d increases for constant x, the transition energy decreases (weakening confinement since L_z increases) and a peak occurs

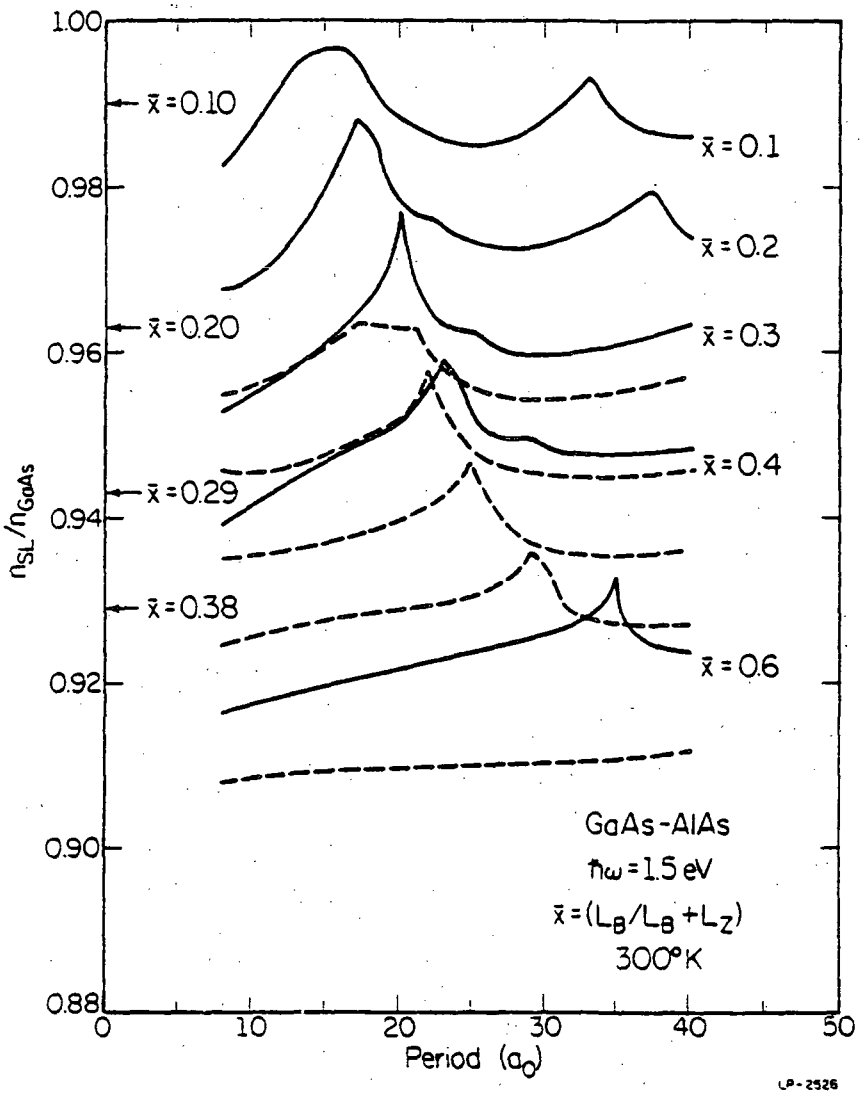

Figure 11. Structure dependence of the normalized index of refraction at 1.5 eV for a number of GaAs-AlAs superlattice structures. The solid and dashed lines are for light being polarized parallel and perpendicular to the layers, respectively, and a_0 is the lattice constant. The arrows on the left-hand side of the figure mark the positions of the normalized experimental alloy values for the indicated mole fractions $\bar{x}$ of Al. The mole fractions given on the right-hand side of the figure belong to the adjacent parallel polarization curve, whereas for perpendicular polarization, the indicated mole fractions correspond to the curves in descending order.

when the energy crosses the 1.5 eV level. Also, as x increases for a constant value of the period, the transition energy increases since L_B is increasing while L_Z is decreasing (AlAs has a larger band gap than GaAs). Therefore, larger L_Z values, i.e., the shift in the peaks for increasing x, are required to reduce the transition energy to the value of 1.5 eV. This explains why the curves with the smallest barrier values, x = 0.1 and 0.2, also contain the E_2(e-hh) transition and why the x = 0.6 curve for perpendicular polarization does not exhibit the E_1(e-*l*h) transition.

The curves also show that there is a strong birefringence which weakens with increasing AlAs content. The reduction in anistropy occurs because of the smaller AlAs Γ region contribution, as explained previously. The large birefringence arises because of the large difference between the Γ region parallel and perpendicular $\epsilon_1(\omega)$ contributions, as shown in Figure 9. In the next chapter, we will show that, in actuality, the birefringence in this model is overestimated due to our neglect of band mixing and our assumption that superstructure effects occur for all energies (see Section 4.3.a).

The most important point to notice in Figure 11 is the positions of the alloy index of refraction values relative to those of the superlattices. For parallel polarization it can be seen that the difference between the alloy and superlattice index of refractions increases with x and with L_B, i.e., with the period. The later trend is in agreement with the experimental findings of Suzuki and Okamoto[100] and confirms the conjecture of Holonyak et al.[9] about the difference between the index of refractions of a superlattice and its corresponding alloy. Figure 11 also shows that this difference is largest at the quantized transition energies. Because the model presented in this chapter neglects exciton effects and, as stated above, has some inherent problems, we cannot take seriously the exact differences between the superlattice and alloy index of refractions. However, the general trends discussed above are correct. Furthermore, since it requires only a small index difference to achieve optical waveguiding (require $\Delta n \sim 0.0063$ assuming a symmetric AlGaAs planar waveguide with a thickness of 2 μm and $\hbar\omega$ = 1.5 eV),[101] the figure shows that

waveguiding is optimized at the quantized transition energies.

In summary, the band structure partition method that we developed for studying the optical properties of III-V binary and ternary compounds has been shown to be successful also for superlattices. The quantization of the electronic states caused by the superstructure has been incorporated into our model within the envelope-function approximation. Unlike the superlattice $\vec{k} \cdot \vec{p}$ approach of Mailhiot et al.,[94] which is limited to calculating the absorption coefficient over a limited frequency range, our method is capable of calculating both the absorption coefficient and refractive index over an extended range of energies. Because our model is based on the partition method, we are able to get good insight into the influence of both the band structure and superlattice parameters on the values of the superlattice optical parameters. An additional virtue of our approach is its flexibility, which enables us to modify easily the model so as to incorporate excitons and band mixing, as will be shown in the next chapter.

5. EFFECT OF EXCITONS ON THE OPTICAL PROPERTIES OF SUPERLATTICES

5.1 Introduction

In the last few years there has been an increasing interest in the properties of excitons in superlattices and multiple quantum wells.[3-5,26] As discussed briefly in Chapter 1, the interest stems principally from the phenomenon that exciton resonances are clearly observable at room temperature, while in bulk semiconductors the resonances are barely noticeable at 300 K.[5] This effect has been attributed to the quasi-two-dimensional character of the excitons in quantum wells which enhances the exciton binding energy and localization while having a small effect on the longitudinal optical (LO) phonon broadening.[5] Because the 2-D exciton peaks can be modulated simply by the application of an electric field,[10] a number of room-temperature, optical devices have been demonstrated which utilize an electroabsorptive effect.[10,102-103] Concomitantly, there have been numerous theoretical papers devoted to understanding the low-energy exciton absorption spectra, with and without electric fields.[10,25] By taking the Kramers-Kronig transformation[63] of the imaginary part of the dielectric constant, $\epsilon_2(\omega)$, it follows that the strength of the 2-D excitons should also have an appreciable effect on the real part of the dielectric constant, $\epsilon_1(\omega)$ and, thus, on the low-frequency index of refraction. This proposition is borne out experimentally.[31,104] Consequently, this has led to the proposal and demonstration of a number of quantum well devices, such as superlattice lasers which are monolithically integrated into higher gap cavities via impurity diffusion,[9] optical-intensity controlled MQW switches,[33] and MQW phase modulators.[34] Therefore, the knowledge of the index of refraction including the excitonic contribution is technologically important.

In this chapter we extend the superlattice band structure model of the previous chapter by including the exciton contribution for the transitions originating around the Γ symmetry point. Both the bound and continuum excitons are modeled using the EMA.[88]

Since we will only be calculating the low-frequency optical properties of superlattices, i.e., $\hbar\omega < 2$ eV, exciton effects at the edges of the Brillouin zone can be neglected as a first approximation because they only affect the overall magnitude of the index of refraction.

In the following section we describe the manner in which the Γ-region, excitonic contribution is added to the superlattice model of the previous chapter. In addition to exciton effects, the superlattice model is also modified to incorporate band-mixing effects and a hybrid, superlattice-alloy, electronic band structure approach. These changes are also discussed in Section 5.2. Section 5.3 is devoted to describing the variational approach we used to compute the ground state exciton wavefunctions and energies. In the final section, results are given for the frequency-dependent absorption coefficient and index of refraction of GaAs-$Al_xGa_{1-x}As$ superlattices. Emphasis is given to comparing these results with those obtained using the superlattice model of the previous chapter.

5.2 Modified Superlattice Electronic Band Structure Model

In the previous chapter, $\epsilon_1(\omega)$ is calculated directly from the band structure results; however, when excitons are included in the model it is necessary to derive $\epsilon_1(\omega)$ by taking the Kramers-Kronig transformation of $\epsilon_2(\omega)$[63]

$$\epsilon_1(\omega) = 1 + \frac{2}{\pi} P \int_0^\infty \frac{E\,\epsilon_2(E)dE}{E^2 - (\hbar\omega)^2} \quad . \tag{41}$$

In the above, P denotes the principal value, and we have written the transformation in terms of energy instead of the usual form of using frequency as the variable.

Our Γ region model of $\epsilon_2(\omega)$ has a bound and a continuum contribution for which we transformed the two parts, separately. The bound part is given by[5.88,105]

$$\epsilon_{2,B}(\omega) = \frac{4\pi e^2}{m_0^2\omega^2} \sum_n \frac{f_n\gamma_n}{[(E-E_{x,n})^2+\gamma_n^2]} \tag{42a}$$

$$f_n = |\phi_n(\vec{r}=0)|^2 |\hat{e}\cdot P_{cv}(\vec{k}_n)|^2 \quad . \tag{42b}$$

The summation is over the bound exciton peaks where each peak is described by a Lorentian function with a half width at half maximum of γ_n and an oscillator-strength f_n. $E_{x,n}$ and $\phi_n(\vec{r})$ are the ground state exciton energy and envelope function for the n^{th} peak, respectively, where $\vec{r}$ is the coordinate of relative motion between the electron and hole. Both $\phi_n(\vec{r})$ and $E_{x,n}$ are calculated using a modified version of the variational approach of Greene et al.[26] (see next section) and γ_n is determined empirically.[5] Finally, $P_{cv}(\vec{k}_n)$ is the momentum matrix element between the valence and conduction bands evaluated at the point in $\vec{k}$ space from which the n^{th} exciton peak originates, assuming the Γ region to be spherically symmetric. Substituting the expression for $\epsilon_{2,B}(\omega)$ into Eq. (41) we obtain

$$\epsilon_{1,B}(\omega) = \frac{4\pi e^2}{m_o^2\omega^2} \sum_n f_n \left[\frac{-2}{E_{x,n}} + \frac{1}{E_{x,n}+\hbar\omega} + \left(\frac{\gamma_n/\pi}{(E_{x,n}-\hbar\omega)^2+\gamma_n^2} \right) \left(\ln \frac{(E_{x,n}^2+\gamma_n^2)^{1/2}}{\hbar\omega} + \frac{\pi}{\gamma_n}(E_{x,n}-\hbar\omega) + \frac{\hbar\omega}{E_{x,n}} - 1 \right) \right] . \quad (43)$$

Because the first two terms in the large brackets are generally small compared to the complicated third term, we evaluated them in the limit as $\gamma_n \to 0$.

For the continuum part, we scaled the imaginary dielectric function $\epsilon_{2,F}(\omega)$, calculated assuming free electron-holes, i.e., the one-electron contribution, by a two-dimensional Sommerfeld factor[106]

$$\epsilon_{2,C}(\omega) = \sum_n \epsilon_{2,F,n}(\omega) \frac{e^{\pi\alpha_n}}{\cosh(\pi\alpha_n)} \quad (44a)$$

$$\alpha_n = \left| \frac{R_n}{\hbar\omega - E_{C,n}} \right|^{1/2} \quad (44b)$$

where to the n^{th} exciton peak there corresponds the n^{th} continuum contribution described by an effective exciton Rydberg factor R_n, a continuum energy $E_{C,n}$, and a free electron-hole dielectric function $\epsilon_{2,F,n}(\omega)$. Because of the presence of the energy-dependent Sommerfeld factor in the expression for $\epsilon_{2,C}(\omega)$, we obtained $\epsilon_{1,C}(\omega)$ by numerically integrating Eq. (41).

Besides adding exciton effects to the model of Chapter 4, in this chapter we also

employed a hybrid, superlattice-isotropic-alloy, electronic band structure approach (see Section 4.3.a). More specifically, we used Eq. (32) and a superlattice band structure for small energies while using Eq. (31) and an isotropic-alloy band structure, within the VCA (see Section 3.2), for larger energies. As a first approximation we assumed the change in properties occurs at a single energy instead of gradually over a range of energies. For the transition energy we chose the top of the electrons' superlattice barrier potential.

In addition to the change to an alloy model for larger energies, we also assumed that exciton effects disappear above the electron barrier and empirically fit the well material hh and *l*h masses such that the n=1 hh and *l*h exciton peaks, respectively, agree with the experimental values while taking strain effects[107] into account. The first assumption follows from our hybrid approach approximation since exciton effects are negligible for bulk materials at 300 K.[5] The second assumption is given support by Mann et al.[108] who find experimentally that in order to fit their magneto-absorption data for single GaAs-$Al_xGa_{1-x}As$ quantum well structures, they had to use hh and *l*h masses of approximately 1.0 and 0.2, respectively, for well thicknesses of $\sim$ 100 Å and Al barrier contents of $\sim$ 0.3. They justified theoretically these large masses by invoking band-mixing effects which give rise to strong non-parabolicities. In the model of the previous chapter for all superlattice structures, we used well material hh and *l*h masses at $\bar{k} = 0$ of 0.51 and 0.082, respectively, i.e., the experimental GaAs 4 K masses.[57]

Consequently, in this empirical fashion we took band-mixing effects into consideration. Note that as discussed in Section 4.3.c, band mixing includes both band repulsion and symmetry exchanges. However, as will be shown in Section 5.4, we obtained good agreement with the experimental data by only including band repulsion effects.

5.3 Exciton Variational Model

A number of authors have calculated the binding energy of Wannier excitons in quantum wells. This has been attempted variationally,[26,109] perturbatively,[110] and using a combined variational-perturbative technique.[111] In this section we extend the variational approach of Greene and Bajaj[26] by making it valid for periodic superstructures and having all of the parameters material and energy dependent. Because our approach is very similar to theirs, in the following we will concentrate only on the important highlights and subtleties of the calculation.

In bulk III-V compounds the Γ-region, Wannier exciton can be described within the framework of the 6x6 $\vec{k} \cdot \vec{p}$ Hamiltonian matrix of Luttinger and Kohn.[112] Because the spin orbit splitting in $Al_xGa_{1-x}As$ systems is much larger than the binding energy of the exciton, the Hamiltonian reduces to a 4x4 matrix consisting of the spin up and spin down hh and *l*h excitons. In a superlattice the degeneracy of the hh and *l*h becomes lifted and the approximation is made that the hh and *l*h exciton systems are approximately independent.[113] Furthermore, because the coulomb interaction does not mix spin states, the 4x4 Hamiltonian can be further reduced to 4 separate effective mass equations.

In a superlattice, the growth direction, i.e., the z-direction, becomes distinct from the other directions and, thus, it is natural to express the exciton Hamiltonian using cylindrical coordinates. Consequently, within the EMA,[88] the Hamiltonian for the hh or *l*h exciton is given by

$$H_{e,h} = \frac{-\hbar^2}{2\mu}\left|\frac{1}{\rho}\frac{\partial}{\partial\rho}\rho\frac{\partial}{\partial\rho}+\frac{1}{\rho^2}\frac{\partial^2}{\partial\phi^2}\right| - \frac{\hbar^2}{2m_e}\frac{\partial^2}{\partial z_e^2}$$

$$-\frac{\hbar^2}{2m_h}\frac{\partial^2}{\partial z_h^2} - \frac{e^2}{\epsilon_0|\vec{r}_e-\vec{r}_h|} + V_{ew}(z_e) + V_{h\omega}(z_h) \qquad (45)$$

where m_e and m_h are the energy-dependent electron and hole masses in the z-direction, respectively, μ is the energy-dependent, electron-hole, reduced, effective mass in the x-y

plane, ϵ_0 is the static dielectric constant, $\bar{r}_e$, for example, is the electron coordinate, and ρ, ϕ, and $z=z_e-z_h$ are the relative, electron-hole coordinates in the cylindrical coordinate system. For simplicity we assumed the masses are isotropic and obtained their energy dependence from the results of the periodic square-well potential problem discussed in Section 4.3.b. Since Eq. (45) is applied in both well and barrier materials, both the masses and ϵ_0 are material dependent. The potential wells for the electrons, $V_{ew}(z_e)$ and holes, $V_{h\omega}(z_h)$ are represented by

$$V_{ew}(z_e) = \begin{cases} 0 & |z_e| < L_Z/2 \\ V_e & L/2 > |z_e| > L_Z/2 \end{cases} \tag{46a}$$

$$V_{h\omega}(z_h) = \begin{cases} 0 & |z_h| < L_Z/2 \\ V_h & L/2 > |z_h| > L_Z/2 \end{cases} \tag{46b}$$

where we have chosen the origin of the coordinate system to be at the center of the GaAs well. The values of V_e and V_h are determined for arbitrary Al barrier content in a manner analogous to that used for obtaining Figure 8. In formulating the exciton problem for long period superlattices, we found that it is only necessary to consider a single period, as in Eqs. (46), since there is negligible overlap between exciton wavefunctions from adjacent wells.

For the exciton wavefunction, assuming $H_{e,h}$ is dominated by the single-particle interactions, we used the trial form suggested by Greene and Bajaj[26]

$$\Psi_{ex} = g_e(z_e)g_h(z_h)h(\rho,z,\phi) \tag{47}$$

where g(z) is given by Eq. (40) for which k_z and K_z for the electron and hole are obtained in the manner described following those equations. The wavefunction $h(\rho,z,\phi)$ describes the internal motion of the exciton and is written as

$$h(\rho,z,\phi) = (1+\alpha z^2)e^{-\delta(\rho^2+z^2)^{1/2}} \tag{48}$$

where α and δ are variational parameters. Their values are obtained by minimizing the expectation value of $H_{e,h}$

$$E_{var} = \frac{\int_{-L/2}^{L/2} dz_e \int_{-L/2}^{L/2} dz_h \int_0^{\infty} \rho d\rho \Psi_{ex}^* H \Psi_{ex}}{\int_{-L/2}^{L/2} dz_e \int_{-L/2}^{L/2} dz_h \int_0^{\infty} \rho d\rho \Psi_{ex}^* \Psi_{ex}} \tag{49}$$

In order to speed up the process of minimizing E_{var}, we used the approach proposed by Kinoshita.[114] Once E_{var} is determined, the ground-state binding energy of the exciton E_x is obtained by subtracting from E_{var} the energy resulting from the periodic square-well potential problem discussed in Section 4.3.b. To calculate $\epsilon_{2,B}(\omega)$, Eq. (42), it is also necessary to determine $\phi(\vec{r}=0)$. By definition $\phi(\vec{r})$ is equivalent to $h(\rho,z,\phi)$.[88] Hence, by normalizing $h(\rho,z,\phi)$ in the manner shown for Ψ_{ex} in Eq. (49) and evaluating it at $\vec{r} = 0$, we obtained

$$\phi(\vec{r}=0) = \frac{\pi}{\delta^3} \tag{50}$$

where we have made the approximation in normalizing $h(\rho,z,\phi)$ that since it rapidly goes to zero within the barrier material, we can take $\frac{L}{2}$ as equal to infinity.

5.4 Results and Discussions

The absorption coefficient of a GaAs-$Al_{0.5}Ga_{0.5}As$ superlattice with a well and barrier thickness of 85 and 80 Å, respectively, is plotted in Figure 12. The results are given for light being polarized parallel to the superlattice layers. The solid and dotted-dashed lines are the theoretical and experimental[115] values, respectively. As in Figure 10, the arrows indicate the quantized, Γ-point, valence band-conduction band transitions which produce the fine structure on the theoretical curve. Since the experimental data have arbitrary units, the data are multiplied by a constant factor such that the two second electron-heavy hole peaks, E_2 (e-hh) coincide. The theoretical curve is calculated using $\vec{k}$ = 0 *l*h and hh masses of approximately 0.091 and 0.34, respectively. The values of γ which are used to fit the five main peaks are ≈ 1.1,3.3, and 9 meV, respectively, while the calculated binding energies E_0 are ≈ 10,10,11,11 and 14 meV, respectively. As can be seen

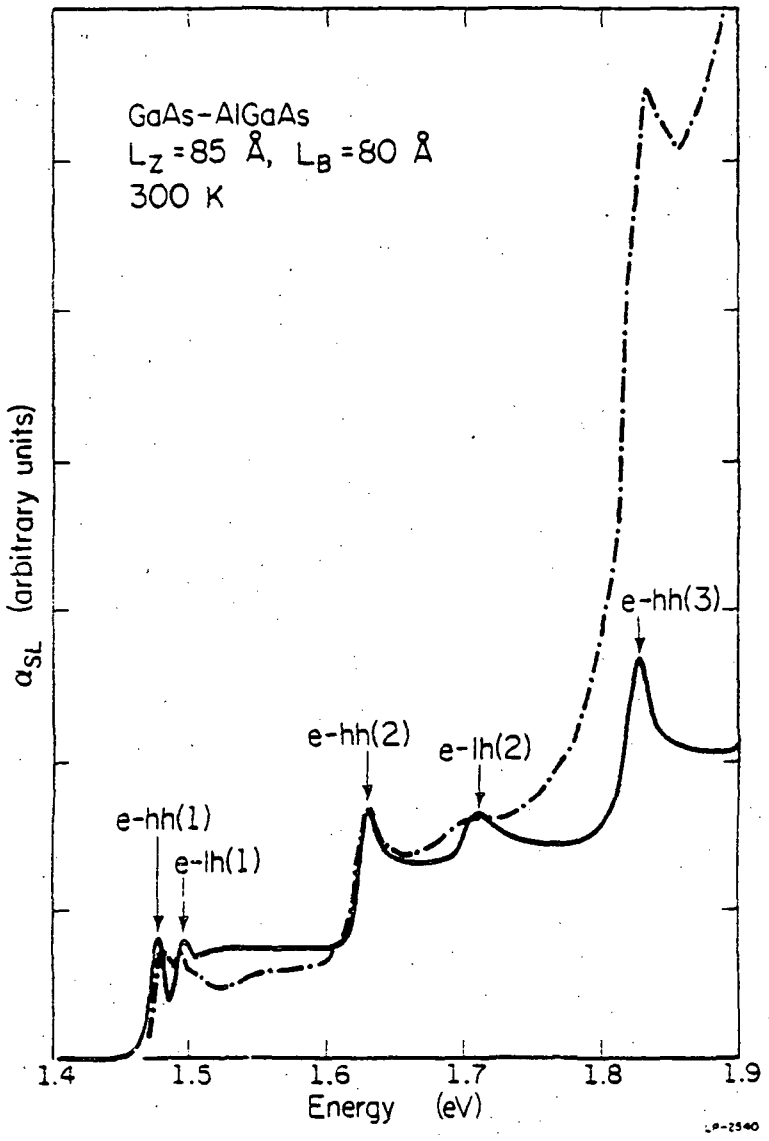

Figure 12. Relative absorption of a GaAs–$Al_{0.5}Ga_{0.5}As$ superlattice for parallel polarization at 300 K. The solid and dotted-dashed lines are the theoretical and experimental values, respectively. The arrows mark the positions, relative to the theoretical curve, of the Γ valley transitions. e-hh(j) corresponds to a transition between the j^{th} level of the heavy hole band and the j^{th} level of the lowest conduction band.

from the figure, our peak positions agree reasonably well with the experimental data, the only discrepancy coming from the E_2(e-*l*h) peak. The error could result from the use of isotropic masses. Since an anisotropic mass would change both the binding energy and the continuum position, it is difficult to ascertain qualitatively the overall effect. The sharp rise in the experimental curve for energies greater than $\approx$ 1.75 eV is due to an experimental artifact.[116] Overall, this figure demonstrates the flexibility of our dielectric constant model to incorporate exciton effects and shows the accuracy of our interface connection rule and exciton binding energy models.

In Figures 13a-c we present some theoretical and experimental values[104] for the index of refraction of a GaAs-$Al_{0.3}Ga_{0.7}As$ superlattice at 300 K for both parallel and perpendicular polarizations. The superlattice has a well thickness L_Z of 70 Å and a barrier thickness L_B of 75 Å. In Figure 13a we compare the index of refraction results of our previous model, i.e., the model of Chapter 4, for parallel and perpendicular polarizations, dashed and dotted-dashed lines, respectively, with those of our current model, i.e., the model of this chapter, without the inclusion of excitons, also for parallel and perpendicular polarizations, solid and dotted lines, respectively. To account for the neglect of excitons at the zone edges and also the neglect of non-band-edge transitions in our model (see Section 2.3), we added the same constant value to each of the theoretical curves so that for parallel polarization at $\hbar\omega$ = 1.416 eV, the results of our complete model given in Figure 13c agree with the experimental data. Note that this is in contrast with our normalization scheme discussed in the previous chapter in which we multiplied by a constant factor (see Section 4.4).

As discussed in Section 5.2, in our previous model we used $\vec{k}$ = 0 *l*h and hh masses of 0.082 and 0.51, respectively, while we fit the n=1 photoluminescence peaks[104] of the GaAs-$Al_{0.3}Ga_{0.7}As$ superlattice of Figure 13 using $\vec{k}$ = 0 *l*h and hh masses of 0.23 and 0.50, respectively. These masses yield exciton binding energies of approximately 12 meV and 17 meV, respectively. We noted in Section 5.2 that Mann et al.[108] found *l*h and hh masses of

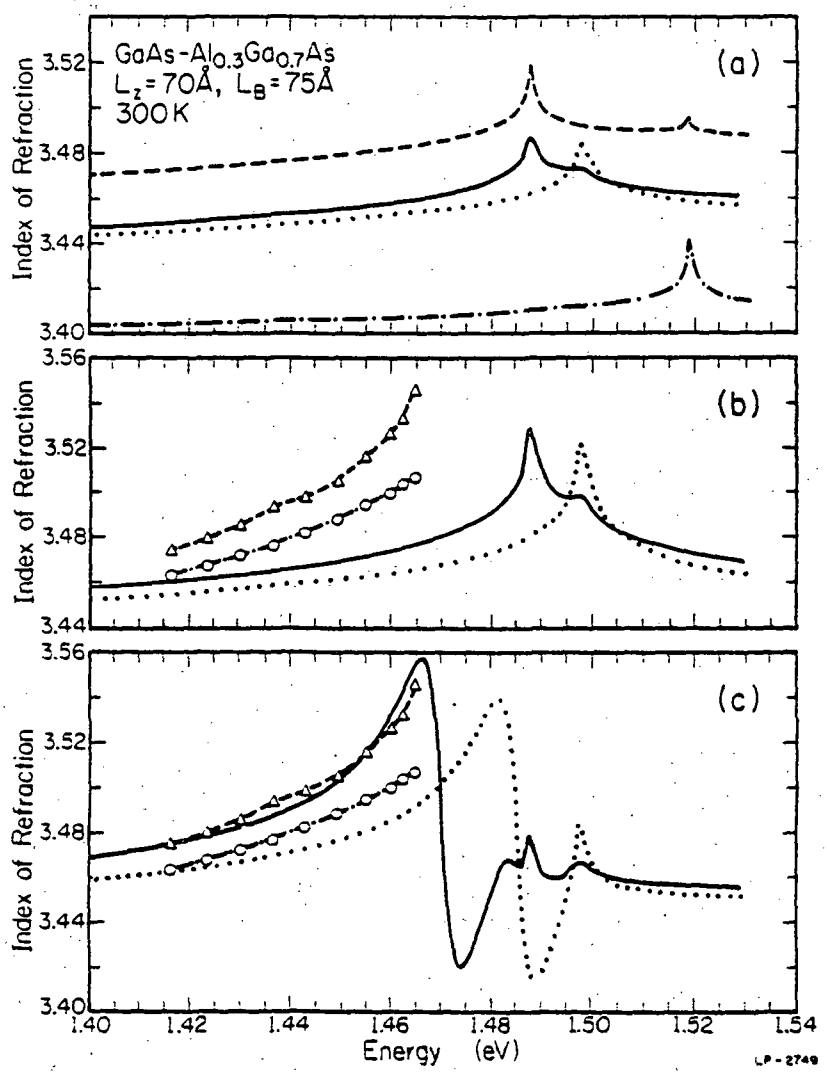

Figure 13. Index of refraction of a GaAs-$Al_{0.3}Ga_{0.7}As$ superlattice. In (a) the dashed and dotted-dashed lines are the results of our previous model (no excitons) for parallel and perpendicular polarizations, respectively, while the solid and dotted lines are the results of our current model (no excitons) for parallel and perpendicular polarizations, respectively. In (b) and (c) the dashed and dotted-dashed lines are the experimental results for parallel and perpendicular polarizations, respectively, while the solid and dotted lines are the results of our current model for parallel and perpendicular polarizations, respectively. In (b) these lines include the continuum exciton contribution and in (c) they include both the continuum and bound exciton contributions.

approximately 0.20 and 1.0, respectively, for similar superlattice structures. Hence, we have experimental support for our empirical *l*h mass; however, we cannot account for the discrepancy in the hh masses. Nevertheless, in spite of this difference, our *l*h and hh exciton binding energies agree very well with those of Mann et al.[108] Note that we used smaller masses to fit the experimental absorption peaks in the previous figure. Hence, band mixing effects vary from one structure to another as a result of the different energy separations between the quantized valence bands.

In Figure 13a the peaks on the parallel polarization curves correspond to the quantized e-hh(1) and e-*l*h(1) transitions, while as in Figure 9 for perpendicular polarization, only the e-*l*h(1) is present. Because the hh masses are the same for the two models in this figure, the energy positions of the hh peaks are equivalent, as opposed to the *l*h situation, where due to differing *l*h masses the peaks are separated, with the peak having the heavier *l*h mass occurring for smaller energies. The most important point to note from this figure is the large difference in the birefringence between the two models which mainly arises from the difference in *l*h masses, while the different handling of the polarizations, as discussed in Sections 4.3.a and 5.2, has a noticeable but smaller effect. Because the quantized hh transitions do not contribute to perpendicular polarization, a large difference in the density of states between the hh and *l*h bands, i.e., a small *l*h mass, is reflected by a large birefringence. However, by terminating the superlattice polarization above a certain energy, one allows the hh band to contribute to perpendicular polarization, thus reducing the birefringence. This polarization change also reduces the magnitude of the hh matrix elements, as can be seen from Eqs. (31) and (32) and noting that for the hh band, $p_x^2 \sim p_y^2$ and $p_z^2 = 0$. This phenomenon accounts for our previous model having a larger parallel contribution in comparison with our current model.

In Figure 13b we compare the results of our current model, including only the continuum exciton contribution, with the experimental data.[104] Again, for the current model, parallel and perpendicular polarizations correspond to the solid and dotted lines,

respectively, and for the data, parallel and perpendicular polarizations correspond to the dashed and dotted-dashed lines, respectively. The experimental data are only available for the energy range presented in this figure. Note that in comparison with the previous figure, the continuum exciton contribution increases the calculated birefringence and raises the overall strength of the index of refraction because of the Sommerfeld factor given in Eq. (44a). However, as can be seen from Figure 13c, the sharp rises in the experimental data correspond to bound exciton peaks. The curve notation in Figure 13c is analogous to that in Figure 13b, and in Figure 13c we have also included the bound exciton contribution in the model. By comparing Figures 13b and 13c, one sees that the bound peaks rise more quickly and have a larger magnitude than the continuum peaks because exciton effects are stronger for the bound case. The two figures also show that the bound exciton contribution increases the birefringence and for parallel polarization, for example, causes the appearance of four sets of peaks instead of two, i.e., bound and continuum peaks for e-hh(1) and e-*l*h(1).

Most importantly, Figure 13c gives support to the validity of the new index of refraction model presented in this chapter by the very good agreement between the theoretical and experimental curves. The only adjustable parameters in the model are the hh and *l*h masses, which we fit to obtain the correct energy for the n=1 exciton peaks, and the Lorentian broadening parameter γ, which was chosen to obtain good agreement between the two parallel polarization curves while being in line with the experimental estimates. To fit the data we used γ = 3.5 meV. As stated previously, the *l*h mass and the *l*h and hh binding energies are in excellent agreement with the experimental values of Mann et al.,[108] while the value for γ is very close to the suggested experimental value of Chemla et al.[5] of approximately 3 meV. Hence, our model also gives good results with *no* adjustable parameters.

There are a couple of other interesting features to gather from Figure 13c. The sharp decrease in the exciton peaks is the result of the Kramers-Kronig transformation of the quasi-2-D, exciton, absorption peaks which resemble broadened, energy-delta functions.

Experimentally, this effect might be difficult to detect due to strong absorption around the peaks causing the loss of signal in this energy range. The slight dip in the theoretical parallel polarization curve for $\hbar\omega \sim 1.485$ eV is due to the contribution of the bound *lh* exciton peak, which is decreasing in this energy range. Again, as a result of absorption effects, this dip is probably not experimentally resolvable. The final point is that comparing Figures 10 and 13 we see that the experimental data of Suzuki and Okamoto [100] do not exhibit bound exciton peaks. We cannot account for this disparity.

In conclusion, we have modified the superlattice model of the previous chapter. In addition to the inclusion of both the bound and continuum exciton contributions for Γ region transitions, we incorporated an empirical, band-mixing scheme and calculated the absorption coefficient and index of refraction using a hybrid approach which combines superlattice and isotropic-alloy, electronic band structure models. Overall, our calculations are in very good agreement with the experimental $\alpha(\omega)$ and $\eta(\omega)$ data and show the accuracy of our new model of the optical properties of superlattices and MQWs. Because our model includes band mixing empirically, we are not able to predict the fine structure in the absorption coefficient, as was done by Chang and Shulman [25]. However, overall our calculated $\alpha(\omega)$ curves agree well with their results and, unlike their approach, which is limited to small regions of the Brillouin zone, we were able to calculate accurately the index of refraction.

6. CONCLUSIONS

The goal of this thesis has been to obtain a working model for the optical parameters of long-period GaAs-$Al_xGa_{1-x}As$ superlattices and MQWs. Our motivation has been the recent development of numerous heterostructure devices whose optimization necessitates a knowledge of the refractive index, which cannot be calculated using existing superlattice models. Prior to calculating the properties of superlattices, it was necessary to develop optical models for both binary and ternary III-V compounds, which are used as inputs to the superlattice model. This required a bulk model which is simple but accurate, and flexible so that it can easily be extended to heterostructures. To accomplish this we have introduced a bulk band structure model based on a hybrid approach which combines the $\vec{k} \cdot \vec{p}$ and nonlocal pseudopotential techniques and partitions the bulk Brillouin zones into the Γ, X, and L regions. The optical properties were calculated as the sum of the contributions of each region.

Our results for the optical properties of bulk III-V compounds are consistent with other one-electron band structure techniques. Because the partition method is based on the $\vec{k} \cdot \vec{p}$ approach, our model has several advantages over the other techniques. They are computational speed, flexibility, and ease of interpretation, i.e., our model engenders a physical understanding of the parameters which influence the dielectric constant. For example, we have found that except for optical absorption in the vicinity of the Γ gap, most of the optical properties of bulk materials, especially the index of refraction, are essentially determined by the electronic structure around the L point, rather than at the center of the Brillouin zone.

For ternary alloys both disorder-assisted and phonon-assisted indirect transitions have been incorporated into the model. The disorder of the alloy has been accounted for by using a straightforward, perturbative, CPA approach which only includes the effects of compositional disorder. The results for the disorder-induced, Γ point, energy-gap bowings

are shown to be nearly comparable to those calculated using a more sophisticated CPA approach. In general the calculated absorption coefficients of $Al_xGa_{1-x}As$ are in good agreement with the experimental data and compare well with existing alloy absorption models.

With this foundation we have formed our superlattice model based on the envelope-function approximation. In addition, the model incorporates band mixing empirically and Γ-region, exciton effects. In general the results of our model for the absorption coefficient and index of refraction of GaAs-$Al_xGa_{1-x}As$ superlattices are in good agreement with the experimental data. Band-mixing effects, which produce changes in the hh and *l*h masses, are shown to have an important effect on the values of the optical parameters. Furthermore, superstructure effects are not present for all energies, but rapidly decrease for energies larger than the height of the potential barriers. The anisotropy and structure dependence of the refractive index are determined to result mainly from the Γ region because of its small conduction band mass, while the outer regions (X and L) of the Brillouin zone provide contributions which are similar to the corresponding alloy values. In comparison with the index of refraction of the corresponding $Al_xGa_{1-x}As$ alloy, characterized by the same average mole fraction $\bar{x}$ of Al, our results indicate that the superlattice index of refraction values attain maxima at the various, quantized, exciton-enhanced, transition energies. Consequently, the waveguiding and reflectance properties of optoelectronic devices which incorporate superlattices can be improved by tailoring the structure to the chosen optical frequency. In sum, we have accomplished our task of obtaining an accurate model of the refractive index of GaAs-$Al_xGa_{1-x}As$ superlattices which can be used to improve existing optoelectronic devices.

APPENDIX. GALLIUM ARSENIDE $\vec{k} \cdot \vec{p}$ PARAMETERS AT 4 K

Γ Region Parameters	Value
A'	-28.0 eV-Å^2
B'	-22.0 eV-Å^2
P'	111.5 eV-Å
Δ	0.341 eV
E_c	1.52 eV

X Region Parameters	Value
D	0.30 eV–Å^2
E1	-11.0 eV–Å^2
E2	6.2 eV–Å^2
F	-0.25 eV–Å^2
G	0.0 eV–Å^2
H'	-24.3 eV–Å^2
I	4.2 eV–Å^2
Δ'	0.125 eV
$E^c_{5,x}$	14.85 eV
$E^c_{3,x}$	5.27 eV
$E^c_{1,x}$	4.93 eV
$E_{5,x}$	-0.06 eV
$E_{3,x}$	-3.99 eV
k_m	0.104 Å^{-1}

L Region Parameters	Value
R'	-17.3 eV–Å^2
S'	13.8 eV–Å^2
T	-9.0 eV–Å^2
U	3.5 eV–Å^2
V'	0.0 eV–Å^2
W	13.5 eV–Å^2
Δ''	0.22 eV
$E^c_{2,L}$	8.67 eV
$E^c_{3,L}$	6.69 eV
$E^c_{1,L}$	3.02 eV
$E_{3,L}$	-0.11 eV
$E_{1,L}$	-5.55 eV

References

1 L. Esaki and R. Tsu. "Superlattice and negative differential conductivity in Semiconductors," IBM J. Res. Dev. *14*, 61 (1970); A.Y. Cho. "Film deposition by molecular-beam techniques." J. Vac. Sci. Technol. *8*, S31 (1971).

2 R.D. Dupuis, P.D. Dapkus, R.M. Kolbas, and N. Holonyak, Jr., "Quantum-well $Al_xGa_{1-x}As$-GaAs heterostructure lasers grown by metalorganic chemical vapor deposition," IEEE J. Quant. Elect. *QE-15*, 756 (1979).

3 R. Dingle, W. Wiegmann, and C.H. Henry, "Quantum states of confined carriers in very thin $Al_xGa_{1-x}As$-GaAs-$Al_xGa_{1-x}As$ heterostructures," Phys. Rev. Lett. *33*, 827 (1974); R. Dingle, "Confined carrier quantum states in ultra thin semiconductor heterostructures," in *Festkorperprobleme XV, Advances in Solid State Physics*, edited by H.J. Queisser (Pergamon, Braunschweig, 1975), p. 21.

4 B.A. Vojak, N. Holonyak, Jr., W.D. Laidig, K. Hess, J.J. Coleman, and P.D. Dapkus, "The exciton in recombination in $Al_xGa_{1-x}As$-GaAs quantum-well heterostructures," Solid State Commun. *35*, 477 (1980).

5 D.S. Chemla, D.A.B. Miller, P.W. Smith, A.C. Gossard, and W. Wiegmann, "Room temperature excitonic nonlinear absorption and refraction in GaAs/AlGaAs multiple quantum well structures," IEEE J. Quant. Elect. *QE-20*, 265 (1984).

6 B.A. Vojak, W.D. Laidig, N. Holonyak, Jr., M.D. Camras, J.J. Coleman, and P.D. Dapkus, "High-energy (visible red) stimulated emission in GaAs," J. Appl. Phys. *52*, 621 (1981).

7 N. Holonyak, Jr., R.M. Kolbas, R.D. Dupuis, and P.D. Dapkus, "Quantum-well heterostructure lasers," IEEE J. Quant. Elect. *QE-16*, 170 (1980).

8 G.C. Osbourne, "Electronic properties of strained-layer superlattices," J. Vac. Sci. Technol. *B1*, 379 (1983).

9 N. Holonyak, Jr., W.D. Laidig, M.D. Camras, J.J. Coleman, and P.D. Dapkus, "IR-red GaAs-AlAs superlattice laser monolithically integrated in a yellow-gap cavity," Appl. Phys. Lett. *39*, 102 (1981).

10 D.A.B. Miller, D.S. Chemla, T.C. Damen, A.C. Gossard, W. Wiegmann, T.H. Wood, and C.A. Burrus, "Electric field dependence of optical absorption near the band gap of quantum-well structures," Phys. Rev. *B32*, 1043 (1985); and references therein.

11 F. Capasso, "Band-gap engineering via graded gap, superlattice, and periodic doping structures: Applications to novel photodetectors and other devices," J. Vac. Sci. Technol. *B1*, 457 (1983).

12 T. Mimura, "The present status of modulation-doped and insulated-gate field-effect transistors in III-V semiconductors," Surf. Sci. *113*, 454 (1982).

13 N. Holonyak, Jr., R.M. Kolbas, W.D. Laidig, B.A. Vojak, K. Hess, R.D. Dupuis, and P.D. Dapkus, "Phonon-assisted recombination and stimulated emission in quantum-well $Al_xGa_{1-x}As$-GaAs heterostructures," J. Appl. Phys. *51*, 1328 (1980).

14 E.E. Mendez, L.L. Chang, G. Landgren, R. Ludeke, L. Esaki, and F.H. Pollack, "Observation of superlattice effects on the electronic bands of multilayer heterostructures," Phys. Rev. Lett. *46*, 1230 (1981).

15 A.C. Gossard, "Molecular beam epitaxy of superlattices in thin films," in *Treatise on Materials Sciences and Technology, Vol. 24*, edited by K.N. Tu and R. Rosenberg (Academic, New York, 1982), p. 13; and references therein.

16 B. Abeles and T. Tiedje, "Amorphous semiconductor superlattices," Phys. Rev. Lett. *51*, 2003 (1983).

17 E. Caruthers and P.J. Lin-Chung, "Electronic structures of GaAs-$Ga_{1-x}Al_xAs$ repeated monolayer heterostructures," Phys. Rev. Lett. *38*, 1543 (1977).

18 J.N. Schulman and T.C. McGill, "Band structure of AlAs-GaAs(100) superlattices," Phys. Rev. Lett. *39*, 1680 (1977).

19 G.A. Sai-Halasz, L. Esaki, and W.A. Harrison, "InAs-GaSb superlattice energy structure and its semiconductor-semimetal transition," Phys. Rev. *B18*, 2812 (1978).

20 J. Ihm, P.K. Lam, and M.L. Cohen, "Electronic structure of the [001] InAs-GaSb superlattice," Phys. Rev. *B20*, 4120 (1979).

21 G. Bastard, "Superlattice band structure in the envelope-function approximation," Phys. Rev. B24, 5693 (1981).

22 S.R. White and L.J. Sham, "Electronic properties of flat-band semiconductor heterostructures," Phys. Rev. Lett. *47*, 879 (1981).

23 J.P. Leburton and K. Hess, "A simple model for the index of refraction of GaAs-AlAs superlattices and heterostructure layers: Contributions of the states around Γ," J. Vac. Sci. Technol. *B1*, 415 (1983).

24 M. Altarelli, "Electronic structure and semiconductor-semimetal transition in InAs-GaSb superlattices," Phys. Rev. *B28*, 842 (1983).

25 Y.C. Chang and J.N. Shulman, "Interband optical transitions in GaAs-$Ga_{1-x}Al_xAs$ and InAs-GaSb superlattices," Phys. Rev. *B31*, 2069 (1985).

26 R.L. Greene and K.K. Bajaj, "Binding energies of Wannier excitons in GaAs-$Ga_{1-x}Al_xAs$ quantum well structures," Solid State Commun. *45*, 831 (1983).

27 M. Jaros, K.B. Wong, M.A. Gell, and D.J. Wolford, "Microscopic description of confinement in quantum well and sawtooth semiconductor superlattices," J. Vac. Sci. Technol. *B3*, 1051 (1985).

28 K.B. Kahen and J.P. Leburton, "Optical constants of GaAs-$Al_xGa_{1-x}As$ superlattices and multiple quantum wells," Phys. Rev. *B33*, 5465 (1986).

29 M. del Castillo-Mussot and L.J. Sham, "Excitonic effect in the optical spectrum of semiconductors," Phys. Rev. *B31*, 2092 (1985).

30 F. Koyama and K. Iga, "Frequency chirping of external modulation and its reduction," Electron. Lett. *21*, 1065 (1985).

31 M. Glick, F.K. Reinhart, G. Weimann, and W. Schlapp, "Quadratic electro-optic light modulation in a GaAs/AlGaAs multiquantum well heterostructure near the excitonic gap," Appl. Phys. Lett. *48*, 989 (1986).

32 H. Yamamoto, M. Asada, and Y. Suematsu, "Electric-field-induced refractive index variation in quantum-well structures," Electron. Lett. *21*, 579 (1985).

33 P.L.K. Wa, J.E. Sitch, N.J. Mason, J.S. Roberts, and P.N. Robson, "All optical multiple-quantum well waveguide switch," Electron. Lett. *21*, 27 (1985); and references therein.

34 A. Alping, X.S. Wu, T.R. Hausken, and L.A. Coldren, "Highly efficient waveguide phase modulator for integrated optoelectronics," Appl. Phys. Lett. *48*, 1243 (1986).

35 D.J. Chadi, "Localized-orbital description of wave functions and energy bands in semiconductors," Phys. Rev. *B16*, *3572 (1977)*.

36 J.N. Schulman, private communication.

37 K.B. Kahen and J.P. Leburton, "General theory of the transverse dielectric constant of III-V semiconducting compounds," Phys. Rev. *B32*, 5177 (1985).

38 E.O. Kane, "Band structure of Indium Antimonide," J. Phys. Chem. Solids *1*, 249 (1957); E.O. Kane, "The $\vec{k} \cdot \vec{p}$ method," in *Semiconductor and Semimetals, Vol. 1*, edited by R.K. Willardson and A.C. Beer (Academic, New York, 1966), p. 75.

39 M. Cardona, "Optical properties and band structure of Germanium and zincblende-type semiconductors," in *Proceedings of the International School of Physics "Enrico Fermi"*, edited by E. Burstein (Academic, New York, 1972), p. 514.

40 J.R. Chelikowsky and M.L. Cohen, "Nonlocal pseudopotential calculations for the electronic structure of eleven diamond and zinc-blende semiconductors," Phys. Rev. *B14*, 556 (1976).

41 J.P. Leburton and K. Kahen, "GaAs-AlGaAs superlattice band structure under hydrostatic pressure: An analysis based on the envelope function approximation," Superlattices Microstruct. *1*, 49 (1985).

42 G. Duggan, "Critical review of heterojunction band offsets," J. Vac. Sci. Technol. *B3*, 1224 (1985).

43 K.B. Kahen and J.P. Leburton, "Exciton effects in the index of refraction of multiple quantum wells and superlattices," submitted to Appl. Phys. Lett.

44 P. Soven, "Coherent potential model of substitutional disordered alloys," Phys. Rev. *156*, 809 (1967).

45 D. Stroud, "Band gaps of semiconductor alloys," Phys. Rev. *B5*, 3366 (1972).

46 A. Baldereschi and K. Maschke, "Band structure of semiconductor alloys beyond the virtual crystal approximation. Effect of compositional disorder on the energy gaps in GaP_xAs_{1-x}," Solid State Commun. *16*, 99 (1975).

47 D.J. Stukel and R.N. Euwema, "Electronic band structure and related properties of cubic AlP," Phys. Rev. *186*, 754 (1969); "Energy-band structure of Aluminum Arsenide," Phys. Rev. *188*, 1193 (1969).

48 T.C. Collins, D.J. Stukel, and R.N. Euwema, "Self-consistent orthogonalized-plane-wave band calculation on GaAs," Phys. Rev. *B1*, 729 (1970).

49 Y.F. Tsay, A.J. Corey, and S.S. Mitra, "Band structure and optical spectrum of AlP," Phys. Rev. *B12*, 1354 (1975).

50 C.S. Wang and B.M. Klein, "First-principles electronic structure of Si, Ge, GaP, GaAs, ZnS, and ZnSe. II Optical properties," Phys. Rev. *B24*, 3417 (1981).

51 D.E. Aspnes, "Interband masses of higher interband critical points in Ge," Phys. Rev. Lett. *31*, 230 (1973).

52 J.R. Chelikowsky and M.L. Cohen, "High-resolution band structure and the E_2 peak in Ge," Phys. Rev. Lett. *31*, 1582 (1973).

53 G. Dresselhaus, "Spin-orbit coupling effects in zinc-blende structures," Phys. Rev. *100*, 580 (1955).

54 P.O. Löwdin, "A note on quantum mechanical perturbation theory," J. Chem. Phys. *19*, 1396 (1951).

55 D.J. Chadi, "Angular momentum decomposition of $\vec{k} = 0$ Bloch functions in group IV and zincblende crystals," Solid State Commun. *20*, 361 (1976).

56 G. Dresselhaus, A.F. Kip, and C. Kittel, "Cyclotron resonance of electrons and holes in Silicon and Germanium crystals," Phys. Rev. *98*, 368 (1955).

57 J.S. Blakemore, "Semiconducting and other major properties of Gallium Arsenide." J. Appl. Phys. *53*, R123 (1982).

58 E.D. Palik and R.F. Wallis, "Infrared cyclotron resonance in n-type InAs and InP." Phys. Rev. *123*, 131 (1961).

59 C.W. Litton, R.B. Denis, and S.D. Smith, "Infra-red cyclotron resonance in n-type epitaxial InAs with evidence of polaron coupling," J. Phys. *C2*, 2146 (1969).

60 C.R. Pidgeon, D.L. Mitchell, and R.N. Brown, "Interband magnetoabsorption in InAs and InSb," Phys. Rev. *154*, 737 (1967).

61 J. Leotin, R. Barbaste, S. Askenazy, M.S. Skolnick, R.A. Stradling, and J. Tuchendler, "Hole mass measurement in p-type InP and GaP by submillimeter cyclotron resonance in pulsed magnetic fields," Solid State Commun. *15*, 693 (1974).

62 A. Onton, "Optical absorption due to excitation of electrons bound to Si and S in GaP," Phys. Rev. *186*, 786 (1969).

63 F. Bassani and G.P. Parravicini, *Electronic States and Optical Transitions in Solids* (Pergamon, Oxford, 1975).

64 D.E. Aspnes and A.A. Studna, "Dielectric functions and optical parameters of Si, Ge, GaP, GaAs, GaSb, InP, InAs, and InSb from 1.5 to 6.0 eV," Phys. Rev. *B27*, 985 (1983).

65 B. Velicky and J. Sak, "Excitonic effects in the interband absorption of semiconductors," Phys. Status Solidi *16*, 147 (1966).

66 W. Hanke and L.J. Sham, "Many-particle effects in the optical spectrum of a semiconductor," Phys. Rev. *B21*, 4656 (1980).

67 C. Hermann and C. Weisbuch, "$\vec{k} \cdot \vec{p}$ perturbation theory in III-V compounds and alloys: A reexamination," Phys. Rev. *B15*, 823 (1977).

68 N. Holonyak, Jr. and S.F. Bevacqua, "Coherent (visible) light emission from $Ga(As_{1-x}P_x)$ junctions," Appl. Phys. Lett. *1*, 82 (1962).

69 W.O. Groves, A.H. Herzog, and M.G. Crawford, "The effect of nitrogen doping on $GaAs_{1-x}P_x$ electroluminescent diodes," Appl. Phys. Lett. *19*, 184 (1971).

70 G.E. Stillman, C.M. Wolfe, A.G. Foyt, and W.T. Lindley, "Schottky barrier $In_xGa_{1-x}As$ alloy avalanche photodiodes for 1.06 μm," Appl. Phys. Lett. *24*, 8 (1974).

71 T.P. Pearsall and M. Papuchon, "The $Ga_{0.47}In_{0.53}As$ homojunction photodiode - A new avalanche photodetector in the near infrared between 1.0 and 1.06 μm," Appl. Phys. Lett. *33*, 640 (1978).

72 J.M. Woodall and H.J. Hovel, "High efficiency $Ga_{1-x}Al_xAs$-GaAs solar cells," Appl. Phys. Lett. *21*, 379 (1972).

73 J.A. Hutchby and R.L. Fudurich, "Theoretical analysis of $Al_xGa_{1-x}As$-GaAs graded band-gap solar cell," J. Appl. Phys. *47*, 3140 (1976).

74 J.M. Ziman, *Models of Disorder* (Cambridge University Press, Cambridge, 1977).

75 A. Baldereschi, E. Hess, K. Maschke, H. Neumann, K.R. Schulze, and K. Unger, "Energy band structure of $Al_xGa_{1-x}As$," J. Phys. *C10*, 4709 (1977).

76 F. Aymerich, "Pseudopotential band structure of $Al_{1-x-y}Ga_xIn_yAs$," Phys. Rev. *B26*, 1968 (1982).

77 J.C. Phillips and J.A. Van Vechten, "Dielectric classification of crystal structures, ionization potentials, and band structures," Phys. Rev. Lett. *22*, 705 (1969).

78 J.A. Van Vechten and T.K. Bergstresser, "Electronic structure of semiconductor alloys," Phys. Rev. *B1*, 3351 (1970).

79 W.E. Pickett, "Theoretical study of the hydrogen saturated ideal silicon vacancy," Phys. Rev. *B23*, 6603 (1981).

80 D. Stroud and H. Ehrenreich, "Band structure of SiGe: Coherent-potential approximation," Phys. Rev. *B2*, 3197 (1970).

81 A.B. Chen and A. Sher, "Valence-band structures of III-V compounds and alloys-Bond orbital and coherent-potential approximations," Phys. Rev. *B17*, 4726 (1978); "Electronic structure of pseudobinary semiconducting alloys $Al_xGa_{1-x}As$, GaP_xAs_{1-x}, and $Ga_xIn_{1-x}P$," Phys. Rev. *B23*, 5360 (1981).

82 D.Z.Y. Ting and Y.C. Chang, "Disorder effect on the photoabsorption of III-V semiconducting alloys," Phys. Rev. *B30*, 3309 (1984).

83 W.P. Dumpke, M.R. Lorenz, and G.P. Pettit, "Enhanced indirect optical absorption in AlAs and GaP," Phys. Rev. *B5*, 2978 (1972).

84 F. Aymerich, F. Meloni, and G. Mula, "General model pseudopotential," Phys. Rev. *B15*, 3980 (1977).

85 K.R. Schulze and K. Unger, "The linear dielectric response of a semiconductor: A new analytic form for the dielectric function," Phys. Stat. Sol. *b66*, 491 (1974).

86 J. Hubbard, "The description of collective motion in terms of many-body perturbation theory. II The correlation energy of a free-electron gas," Proc. Royal. Soc. *A243*, 336 (1957).

87 H.C. Casey, D.D. Sell, and M.B. Parish, "Refractive index of $Al_xGa_{1-x}As$ between 1.2 and 1.8 eV," Appl. Phys. Lett. *24*, 63 (1974).

88 R.J. Elliott, "Theory of exciton: I," in *Polarons and Excitons*, edited by C.G. Kuper and G.D. Whitfield (Plenum, New York, 1963), p. 269.

89 S. Adachi, "GaAs, AlAs, and $Al_xGa_{1-x}As$: Material parameters for use in research and device applications," J. Appl. Phys. *58*, R1 (1985).

90 B. Monemar, K.K. Shih, and G.D. Pettit, "Some optical properties of the $Al_xGa_{1-x}As$ alloy system," J. Appl. Phys. *47*, 2604 (1976).

91 H. Shichijo, "Theoretical studies of high field transport in III-V semiconductors," Ph.D. dissertation, University of Illinois, Urbana, IL, 1980.

92 W.D. Laidig, J.W. Lee, and P.J. Caldwell, "Embedded-mirror semiconductor laser," Appl. Phys. Lett. *45*, 485 (1984).

93 R. Tsu and L. Ioriatti, "Longitudinal dielectric constant for quantum wells," Superlattices Microstruct. *1*, 295 (1985).

94 C. Mailhiot, T.C. McGill, and D.L. Smith, "New approach to the $\vec{k} \cdot \vec{p}$ theory of semiconductor superlattices," J. Vac. Sci. Tech. *B2*, 371 (1984).

95 B.R. Nag, in *Electron Transport in Compound Semiconductors*, edited by H.J. Queisser (Springer, New York, 1980), vol. 11.

96 K.B. Kahen, unpublished results.

97 G.Y. Wu, C. Mailhiot, and T.C. McGill, "Optical properties of HgTe-CdTe superlattices," Appl. Phys. Lett. *46*, 72 (1985).

98 G.A. Sai-Halasz, R. Tsu, and L. Esaki, "A new semiconductor superlattice," Appl. Phys. Lett. *30*, 651 (1977).

99 W.D. Laidig, D.K. Blanks, and J.F. Schetzina, "Reflectance of AlAs-GaAs and $In_{0.28}Ga_{0.72}As$-GaAs superlattices," J. Appl. Phys. *56*, 1791 (1984).

100 Y. Suzuki and H. Okamoto, "Refractive index of GaAs-AlAs superlattices grown by MBE." J. Electron. Mater. *12*, 397 (1983).

101 R.G. Hunsperger, *Integrated Optics: Theory and Technology* (Springer, New York, 1982), p. 35.

102 T.H. Wood, C.A. Burrus, A.H. Grauck, J.M. Wiesenfeld, D.A.B. Miller, D.S. Chemla, and T.C. Damen, "Wavelength-selective voltage-tunable photodetector made from multiple quantum wells." Appl. Phys. Lett. *47*, 190 (1985).

103 T.H. Wood, C.A. Burrus, D.A.B. Miller, D.S. Chemla, T.C. Damen, A.C. Gossard, and W. Wiegmann, "High speed optical modulation with GaAs/GaAlAs quantum wells in p-i-n diode structure." Appl. Phys. Lett. *44*, 16 (1984).

104 G.J. Sonek, J.M. Ballantyne, Y.J. Chen, G.M. Carter, S.W. Brown, E.S. Koteles, and J.P. Salems, "Modal dispersion of GaAs/AlGaAs multiple quantum well waveguides." in *Proceedings of the Topical Meeting on Integrated Circuits and Guided Wave Optics*, Atlanta, GA, 1986, p. 18.

105 D.F. Blossey, "Wannier exciton in an electric field. I. Optical absorption by bound and continuum states." Phys. Rev. *B2*, 3976 (1970).

106 M. Shinada and S. Sugano, "Interband optical transitions in extremely anisotropic semiconductors. I. Bound and unbound exciton absorption." J. Phys. Soc. Jap. *21*, 1936 (1966).

107 R. Dingle and W. Wiegmann, "Optical investigation of stress in the central GaAs layer of molecular-beam-grown $Al_xGa_{1-x}As$-GaAs-$Al_xGa_{1-x}As$ structures." J. Appl. Phys. *46*, 4312 (1975).

108 J.C. Mann, G. Belle, A. Fasolino, M. Altarelli, and K. Ploog, "Magneto-optical determination of exciton binding energy in GaAs-$Al_xGa_{1-x}As$ quantum wells." Phys. Rev. *B30*, 2253 (1984).

109 R.C. Miller, D.A. Kleinman, W.T. Tsang, and A.C. Gossard, "Observation of the excited level of excitons in GaAs quantum wells." Phys. Rev. *B24*, 1134 (1981).

110 Y.C. Lee and D.I. Lin, "Wannier exciton in a thin crystal film." Phys. Rev. *B19*, 1982 (1979).

111 T.F. Jiang, "An alternative approach to exciton binding energy in a GaAs-$Al_xGa_{1-x}As$ quantum well." Solid State Commun. *50*, 589 (1984).

112 J.M. Luttinger and W. Kohn, "Motion of electrons and holes in perturbed periodic fields." Phys. Rev. *97*, 869 (1955).

113 A. Baldereschi and N.C. Lipari, "Energy levels of direct excitons in semiconductors with degenerate bands." Phys. Rev. *B3*, 439 (1971).

114 T. Kinoshita, "Ground state of the Helium atom." Phys. Rev. *105*, 1490 (1957).

115 S.W. Kirchoefer, N. Holonyak, Jr., K. Hess, D.A. Gulino, H.G. Drickamer, J.J. Coleman, and P.D. Dapkus, "Absorption measurements at high pressure on AlAs-$Al_xGa_{1-x}As$-GaAs superlattices." Appl. Phys. Lett. *40*, 821 (1982).

116 N. Holonyak, Jr. (private communication).

VITA

Keith Brian Kahen was born on [redacted] in [redacted]. He received a B.S. in Physics in 1981 and an M.S. in Electrical Engineering in 1983 from the University of Illinois at Urbana. While at the University of Illinois, he served as a teaching assistant in the Department of Electrical Engineering and as a research assistant in the Coordinated Science Laboratory. He is currently a candidate for the degree of Doctor of Philosophy.